NASA TECHNICAL NOTE

NASA TN D-3029

NASA TN D-3029

SEMIEMPIRICAL METHOD FOR PREDICTING EFFECTS OF INCIDENT-REFLECTING SHOCKS ON THE TURBULENT BOUNDARY LAYER

by S. Z. Pinckney

Langley Research Center
Langley Station, Hampton, Va.

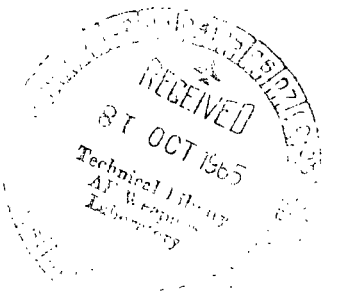

NATIONAL AERONAUTICS AND SPACE ADMINISTRATION • WASHINGTON, D. C. • OCTOBER 1965

SEMIEMPIRICAL METHOD FOR PREDICTING EFFECTS OF INCIDENT-REFLECTING SHOCKS ON THE TURBULENT BOUNDARY LAYER

By S. Z. Pinckney

Langley Research Center
Langley Station, Hampton, Va.

NATIONAL AERONAUTICS AND SPACE ADMINISTRATION

For sale by the Clearinghouse for Federal Scientific and Technical Information
Springfield, Virginia 22151 – Price $3.00

SEMIEMPIRICAL METHOD FOR PREDICTING EFFECTS OF INCIDENT-REFLECTING SHOCKS ON THE TURBULENT BOUNDARY LAYER

By S. Z. Pinckney
Langley Research Center

SUMMARY

A method is presented for the calculation of the boundary-layer velocity profile change and various thickness parameter changes across a two-dimensional incident-reflecting shock. The method employs a one-dimensional hypothetical flow, representative of the boundary layer, in conjunction with a postulated boundary-layer shock model. Curves, calculated by using the method, are presented for boundary-layer velocity profile, boundary-layer thickness, momentum-thickness and displacement-thickness changes across an incident-reflecting shock for a Mach number range from 2 to 6, a Reynolds number range based on an equivalent length from 3.3×10^5 to 3.3×10^7, and incident shock-turning angle range from 0° to 12°. Curves are also presented (empirically determined) for important incident-reflecting shock—boundary-layer interaction lengths. An outline of a procedure which can be followed in the practical application of the method is also included.

Comparison of the calculated velocity profile change (measured through the profile index change) and boundary-layer thickness change with experimental data gave good agreement. For example, the values of profile index change and boundary-layer thickness change are found to agree with data to within 10 percent or better for the Mach number range from 1.9 to 3.85, Reynolds number range based on an equivalent length of approximately 10^7 to 10^8, and incident shock-turning angles up to 13°.

INTRODUCTION

The optimum design and performance of inlets for hypersonic air-breathing propulsion systems present a number of problems of interest. The successful design of such inlets requires methods for closely estimating the growth of the turbulent boundary layer across shocks in the inlet compression flow field. The present paper presents such a method for two-dimensional, incident-reflecting shocks which is based on the usual conservation equations and employs certain empirical representations of parameters. In view of the empirical features, the method is regarded as a correlation procedure for determining the effects

of incident-reflecting shocks on the turbulent boundary layer as indicated by data available in the literature and by some unpublished data.

A number of analytical investigations have been conducted on the changes in a turbulent boundary layer across incident-reflecting shocks which generally use one of two basic lines of approach. The first approach employs momentum integral methods of which the analyses of references 1 and 2 are examples. The second approach (for example, ref. 3) employs a one-dimensional hypothetical boundary layer representative of the real boundary layer together with a postulated boundary-layer shock model. Sufficient experimental investigations are available (see refs. 4, 5, and 6) which provide measurements of changes in velocity profile and various thickness parameters through the shock-interaction region for evaluating the accuracy of the theories.

In general, the analytical methods of references 1 to 3 predict the velocity profile change accurately but do not predict satisfactorily the boundary-layer thickness change. The present correlation method is similar in approach to that of reference 3 and employs a one-dimensional hypothetical flow and a postulated boundary-layer shock model. The shock model of the present analysis permits the evaluation by empirical representations of the mass flow influx to the boundary layer due to turbulent mixing in the shock-interaction region, whereas the shock model of reference 3 does not include a means for the determination of this mass influx.

In the present correlation method the boundary layer upstream of the incident-reflecting shock is converted to an equivalent one-dimensional flow through use of the momentum, continuity, and energy relations by assuming exponential velocity profiles and the modified Crocco enthalpy distribution. A boundary-layer shock model is constructed employing conventional two-dimensional, weak shock theory along with empirical representations for important shock model dimensions which are based on schlieren and shadowgraph pictures and pressure survey data. Downstream of the shock model at the station where the theoretical pressure rise is realized in the real flow, the equivalent one-dimensional flow is converted back to the real boundary-layer flow and yields the velocity profile index and the velocity, momentum, and displacement thicknesses at this station. The empirical representations are required because turbulent boundary layers are not amenable to theoretical evaluation.

The correlation method covers the ranges of independent variables available in the experimental data as follows: adiabatic-wall upstream Mach numbers from 1.0 to 6.0, incident shock-turning angles from 0° to 12°, upstream values of velocity profile index from 4.6 to 11.5, and upstream Reynolds numbers (based on an equivalent length) from 3.4×10^5 to 2×10^8. In addition to the dependent variables previously mentioned, the correlation method provides the significant geometric lengths of the interaction region, and the paper also presents a means of evaluating the velocity profile development in the constant-pressure mixing region downstream of the interaction region.

A preliminary version of this paper was presented in reference 7; the present paper presents further refinements of data correlations made possible

by additional data and additional correlations of value to the solution of the overall incident-shock turbulent boundary-layer interaction problem.

SYMBOLS

C_F average friction coefficient for turbulent flow

C_p specific heat of air at constant pressure

C_V specific heat of air at constant volume

$f(M_e)$ effective Mach number function, $\dfrac{M_e\left(1 + \dfrac{\gamma - 1}{2} M_e^2\right)^{1/2}}{1 + \gamma M_e^2}$

h static enthalpy, C_pT

H boundary-layer shape factor, δ^*/θ

K mixing constant

l_1, l_2 lengths identified in figures 8 and 9

L_{eq} distance required for distorted velocity profile at station d to return to an equilibrium profile

L_u distance from inviscid intersection of incident shock with wall to most upstream point at which pressure rise is detectable

L_t distance from most upstream point the shock pressure rise is detectable on wall to point downstream of shock where pressure rise on wall is 0.99 of pressure ratio across shock

M Mach number

m boundary-layer mass flow per unit area, $\displaystyle\int_0^1 \rho_b V_b d\left(\frac{y}{\delta}\right)$

m_l free-stream mass flow per unit area, $\rho_l V_l$

N profile index value corresponding to an exponential velocity profile having same value of m/m_l as that of an actual profile

N_L exponent of an exponential velocity profile $\dfrac{V_b}{V_l} = \left(\dfrac{y}{\delta}\right)^{1/N_L}$ which fits as much of an actual boundary-layer velocity profile as possible

N_{φ/φ_l}	profile index value corresponding to an exponential velocity profile having the same value of φ/φ_l as that of an actual profile
p	pressure
Δp	theoretical overall static-pressure rise across incident and reflecting shocks
q	dynamic pressure, $\frac{\rho V^2}{2}$
r	adiabatic-wall recovery factor for turbulent flow (assumed to be 0.896)
R	gas constant
R_x	Reynolds number based on x
R_δ	Reynolds number based on δ
R_θ	Reynolds number based on θ
T	temperature
V	velocity
w	boundary-layer mass flow, $\int_0^\delta \rho_b V_b \, dy$
x	distance measured in direction of free-stream flow parallel to a plate
Δx	increment in the x-direction
y	perpendicular distance from wall
Y_1	distance from wall to intersection of wall shock and incident shock
α	single shock-turning angle, deg
α_b'	extra compression angle, deg
β	shock wave angle, deg
β'	shock wave angle for portion of incident and reflecting shocks between wall and intersection of incident and reflecting shocks
γ	ratio of specific heats (1.4), C_p/C_V

δ thickness of boundary layer at point where $\frac{V_b}{V_l} = 1.0$

δ'' thickness of boundary layer at point where $\frac{V_b}{V_l} = 0.99$

δ_d' boundary-layer thickness as indicated in figures 8 and 9

δ^* displacement thickness, $\int_0^{\delta} \left(1 - \frac{\rho_b V_b}{\rho_l V_l}\right) dy$

η boundary-layer energy parameter, $\int_0^1 \rho_b V_b^3 d\left(\frac{y}{\delta}\right)$

η_l free-stream energy parameter, $\rho_l V_l^3$

θ momentum thickness, $\int_0^{\delta} \frac{\rho_b V_b}{\rho_l V_l}\left(1 - \frac{V_b}{V_l}\right) dy$

ρ mass density

Φ_b total momentum flux per unit area in boundary layer, $p_l\left(1 + \gamma M_l^2 \frac{\varphi}{\varphi_l}\right)$

φ boundary-layer momentum parameter, $\int_0^1 \rho_b V_b^2 d\left(\frac{y}{\delta}\right)$

φ_l free-stream momentum parameter, $\rho_l V_l^2$

Subscripts:

A,B successive shocks

b boundary layer

d maximum pressure rise point on wall downstream of an incident-reflecting shock

e equivalent

eq equilibrium

E station where the boundary layer reaches an equilibrium velocity profile downstream of station d

i	incompressible
ℓ	local free stream
t	stagnation conditions
1	station upstream of a shock—boundary-layer interaction where the pressure rise is first detectable on wall
1/7	corresponding to an exponential velocity profile having as an exponent 1/7
3	longitudinal station as identified in figure 1(c)
x	axial location

Primed values are at station δ_d' unless otherwise defined.

ANALYSIS

Analytical Boundary-Layer Shock Model

If the supersonic flow over a plate were inviscid, the pressure rise on the plate generated by an intersecting incident-reflecting shock would be instantaneous (at station 2 of fig. 1(a)) and thus cover an infinitesimal distance. In the real flow, however, a boundary layer exists next to the plate and contains low kinetic energy and low Mach number flow in its lower regions. The low kinetic energy flow does not contain sufficient momentum to traverse the pressure rise of the shock without gaining additional kinetic energy from the outer layers of the boundary layer. Thus, a spreading out of the shock pressure rise occurs to provide the distance needed to add the necessary kinetic energy by turbulent mixing. This phenomenon is illustrated by the pressure distribution of figure 1(a) where the pressure rise produced by the shock starts at station 1 and a maximum value is reached at station d and it corresponds to the theoretical inviscid flow's shock pressure rise. As shown in figure 1(a), there may be an inflection near the middle of the wall pressure distribution curve if the shock strength is sufficient to produce separation.

The complicated shock pattern within the boundary layer produced by the spreading out of the shock pressure rise is illustrated in the bottom sketch of figure 1(a) which is based on shadowgraph and schlieren observations; typical shadowgraph and schlieren pictures obtained under contract NAS1-3489 by General Dynamics Corporation are shown in figure 1(b). The incident shock approaches the boundary-layer edge from the left and curves after entering the boundary layer to produce higher shock angles with higher turning angles at the lower Mach numbers of the boundary layer. The increasing angle of the incident shock after entering the boundary layer is a result of the boundary-layer shock attempting to match the free-stream pressure rise. The thickening of the low kinetic energy regions of the boundary layer caused by the adverse pressure gradient results in a shock being initiated upstream in the vicinity of the

wall (wall shock) which turns the flow away from the wall. This shock crosses the incident shock, proceeds toward the free stream, and forms the reflecting shock. Near the edge of the boundary layer, the wall shock is joined by additional expansion and compression waves which originate within the boundary layer. In actual boundary-layer shock configurations, the extension of the free-stream incident shock to the wall (inviscid intersection with wall), station 2, is a convenient reference point for longitudinal dimensions. The length of the interaction region upstream from the reference point is L_u and the total length L_t.

Figure 1(c) shows the selected analytical boundary-layer shock model to be similar to the one indicated by shadowgraph and schlieren pictures. In order to avoid an analysis involving curved shocks, the boundary-layer flow at station 1 of the analytical model is converted to one-dimensional equivalent flow through the use of integrated values of mass, momentum, and energy corresponding to the profile index N. The one-dimensional flow is then treated with the two-dimensional shock system of the analytical model by using existing two-dimensional shock tables. At an appropriate downstream station, the uniform equivalent flow is converted back to boundary-layer flow by the reverse process. Integrations involved in converting back and forth from boundary-layer flow to equivalent flow were made by assuming exponential velocity profiles and a modified Crocco enthalpy distribution as presented in reference 8.

The orientation of the incident and wall shocks in the analytical model (fig. 1(c)) is fixed by locating the intersection of the two shocks at a distance from the wall Y_1 corresponding to an empirical correlation of data obtained from schlieren and shadowgraph pictures. This analytical shock model produces a void region (cross-hatched) adjacent to the wall which in the real flow corresponds to a low kinetic energy flow (in some cases separated).

Up to station d' no mass flow has been added to the boundary layer; however, data indicate that by the time the flow reaches station d, a considerable amount of mass-flow addition has occurred. In the attempt to determine a means for estimating the mass addition between stations d' and d, it was noted that if the mass-flow addition were assumed to be that required to fill the void region at station d' at conditions corresponding to the equivalent flow at station d', a total mass flow at station d' was obtained which experimental data showed to be 8 to 12 percent less than the measured mass flow at station d. To eliminate this discrepancy between calculated and actual mass addition, the strength of the wall shock was increased by stipulating a turning angle greater than the angle α_b by the small angle α_b'. By increasing the turning of the wall shock by the amount α_b', the void region height was made to be a direct measure of the necessary mass addition. It was found that good agreement was obtained between experimental data and the computed thickness change when it is assumed that α_b' is equal to 2° for $\alpha_1 \geq 3^\circ$ and equal to $\frac{2}{3}\alpha_1$ for $\alpha_1 \leq 3^\circ$. The assumption of a linear variation of α_b' for $\alpha_1 \leq 3^\circ$ was made in order to keep the extra turning angle α_b' less than the free-stream incident shock turning angle α_1.

As a result of the preceding considerations, the wall shock of the analytical model (fig. 1(c)) has a turning angle of $\alpha_b + \alpha_b'$ and the boundary-layer portion of the incident shock has a turning angle of α_b. The height of the void region at station d' is a direct measure of the mass-flow addition between station d' and station d. The equivalent flow at station d' is turned out from the wall by the amount α_b'. The expansion wave with turning α_b' originates at the shoulder of the void region and produces flow parallel to the wall at all locations downstream of station 3. Calculation of the turning angle α_b by the methods outlined in a later section also yields a value of the velocity profile index N_3 (corresponding to equivalent flow at station 3), which experimental data indicated to be equal to N_d.

For simplicity in the present analysis all the mass-flow addition is assumed to occur in the mixing region downstream of station 3, as indicated in the sketch of figure 1(c), although in the real case the mass addition starts in the vicinity of station d'. Under this assumption the results of the analysis show that the values computed for α_b by using the extra turning angle α_b' and the conditions at station 3 are correct and that N_3 is equal to N_d. Therefore, in the region between stations 3 and d, the velocity profile remains constant while the mass-flow addition occurs. The boundary-layer thickness at station d δ_d is determined by incorporating the mass-flow addition in a simple continuity relation between stations 1 and d. Other boundary-layer parameters of interest at station d are readily determined from N_d and δ_d. In the calculation of δ_d and N_d, the effects of the wall friction were assumed to be negligible inasmuch as this condition seemed to be an unnecessary complication in view of the empirical features of the method.

The assumption that the height of the void region at station d' is a direct measure of the mass-flow addition is considered to be reasonable in view of the general character of the phenomena. The size of the void region is a direct function of the location of the intersection of the incident and wall shocks with respect to the wall; the location of the intersection in turn is determined by the effect on the boundary layer of the adverse pressure gradient induced by the incident shock. Furthermore, the height of the void region at station d' relative to the boundary-layer thickness is a measure of the distortion of the boundary layer of the real flow and thus a measure of the rate of turbulent mixing.

The model static-pressure distribution for the equivalent boundary-layer flow is shown in figure 1(a). As a two-dimensional shock model was assumed in the present analysis for a boundary-layer shock model, all pressure changes in the equivalent boundary-layer flow will be instantaneous and thus of infinitesimal length. At station 1 the free-stream static pressure is converted to the static pressure of the equivalent boundary-layer flow which is slightly lower than the free-stream static pressure. The analytical shock model is then traversed by the equivalent boundary-layer flow until station d is reached and then the static pressure of the equivalent flow is converted back to the actual static pressure. The only criterion relative to static pressure that is incorporated in the correlation method is that the overall static-pressure rise

between stations 1 and d is the same as that for the real flow. The differences, at stations 1 and d, between the magnitude of the static pressure of the actual boundary layer and the static pressure of the equivalent boundary layer are inherent in the method chosen for the conversion to one-dimensional flow.

Definition of Characteristics of Undisturbed Boundary Layer Upstream of Shock-Pressure Rise

The first step required by the present method is the determination of integrated values of mass, momentum, and energy corresponding to the profile index N of the undisturbed upstream boundary layer for the purpose of converting this boundary layer to equivalent one-dimensional flow. The preferred procedure for the determination of these integrated parameters would involve the use of a single simply determined parameter. The Reynolds number correlation of the profile index N_L presents a method for evaluating such a parameter; an example of this type of correlation is presented in figure 18 of reference 9. The velocity profile parameter N_L is the exponent of an exponential velocity profile $\frac{V_b}{V_l} = \left(\frac{y}{\delta}\right)^{1/N_L}$ which is the best fit of the actual boundary-layer velocity profile. The correlation of the profile index N_L in terms of Reynolds number R_{xe} is presented in figure 2. The equivalent Reynolds number R_{xe} of each data point of figure 2 is based on the length of flat plate x_e at local free-stream conditions required to obtain the momentum thickness of the station with turbulent boundary layer from the plate leading edge. The experimental data of figure 2 include data from references 9 to 14 as well as some data obtained under contract NAS1-3489 with General Dynamics Corporation; these experimental data cover a Mach number range from 0 to 6. The curve shown in figure 2 was obtained from an empirical representation for incompressible equilibrium velocity profiles of reference 6 and seems to describe the compressible experimental data very well. In choosing experimental data for figure 2, data were chosen which were believed to be essentially for flat-plate undisturbed flow and thus also have equilibrium velocity profiles. Comparison of all data reveals no Mach number effect on the profile index N_L in the Mach number range considered.

As shown in figure 2, experimental data exist from which the profile index N_L can be obtained for a very broad range of Reynolds numbers. In the correlation method of the present analysis, however, the parameter N and not N_L is used to determine the integrated values of boundary-layer mass flow, momentum, and energy in a manner similar to the method used in formulating the tables of reference 8. The profile index N corresponds to an exponential profile having a value of $\frac{m}{m_l} = \int_0^1 \frac{\rho_b V_b}{\rho_l V_l} d\left(\frac{y}{\delta}\right)$ identical with that of the actual boundary layer. A curve representing the relationship between N_L and N was obtained from an empirical correlation of the existing experimental data and is presented in figure 3 along with some example data points (obtained under Contract NAS1-3489).

Conversion to Equivalent One-Dimensional Boundary-Layer Flow

An equivalent one-dimensional boundary-layer flow, for the purposes of the present analysis, is defined as a one-dimensional flow which has a value of total mass flow equal to the corresponding integrated values of the actual boundary layer; this equivalent one-dimensional flow has the same values of momentum and energy which correspond to a boundary layer with an exponential profile (exponent N) and the same mass flow as the actual boundary layer. In ensuing comparisons of the results from the present correlation method and experimental data, it was not found necessary to match the momentum and energy in the one-dimensional flow with that of integrated values from the actual boundary layer to obtain significant results. The expression for the equivalent one-dimensional Mach number derived in appendix A in a form similar to the mass momentum method of reference 15 is as follows:

$$f(M_e) = \frac{M_l \left(\frac{m}{m_l}\right)^{1/2} \left(\frac{N}{N+1} + \frac{\gamma - 1}{2} M_l^2 \frac{\eta}{\eta_l}\right)^{1/2}}{1 + \gamma M_l^2 \frac{\varphi}{\varphi_l}} \tag{1}$$

where

$$f(M_e) = \frac{M_e \left(1 + \frac{\gamma - 1}{2} M_e^2\right)^{1/2}}{1 + \gamma M_e^2} \tag{2}$$

Equation (1) shows that the equivalent Mach number is a function of the velocity profile index N and the corresponding integrated values of mass, momentum, and energy as defined in appendix A. In using equation (1) to convert the boundary layer upstream of the shock system (station 1 of fig. 1) to a one-dimensional equivalent flow, the value of N for equilibrium velocity profiles is obtained as described in the previous section. For nonequilibrium velocity profiles, the value of N must be determined by some other method. Values of the integrated boundary-layer parameters may be obtained from figures 4 to 6 as a function of Mach number at the edge of the boundary layer M_l and the profile index N. The calculation of the curves of figures 4 to 6 was performed on a digital computer; the modified Crocco enthalpy distribution of reference 8 was assumed in the computation of figures 4 to 6. Solutions for equations (1) and (2) were also obtained in the computations and are presented in figure 7 in terms of $M_l - M_e$ as a function of N and M_l.

Values of other equivalent flow parameters can be obtained by using M_e, N, M_l, and other appropriate equations. For example, the equivalent static pressure p_e can be obtained from the momentum equation (appendix A) as follows:

$$\frac{p_e}{p_l} = \frac{1 + \gamma M_l^2 \frac{\varphi}{\varphi_l}}{1 + \gamma M_e^2} \tag{3}$$

Boundary-Layer Shock-Turning Angle and Profile Index Change

After the upstream boundary layer is converted to equivalent one-dimensional flow, the next step in the correlation method is to establish a procedure for computing the turning angle α_b of the individual boundary-layer shocks. The criteria, from which the computation of α_b is developed, have as their basis the matching of the overall static-pressure rise through the boundary layer $\left(\frac{p_{l,3}}{p_{l,1}}\right)_b$ with the theoretical overall static-pressure rise through the shocks and expansion outside of the boundary layer $\left(\frac{p_{l,3}}{p_{l,1}}\right)_l$. At station 3 of figure 1(c), the pressure changes have been completed in both the boundary layer and free stream and no mass-flow addition to the boundary layer has occurred in the shock model. The calculations for α_b will be performed between stations 1 and 3 (fig. 1(c)) instead of between stations 1 and d. Station d is not a suitable downstream station as the mass flow added to the boundary layer in the mixing region between stations 3 and d cannot be determined until α_b is known.

The value of the overall static-pressure rise $\left(\frac{p_{l,3}}{p_{l,1}}\right)_l$ through the shocks and expansion in the free stream can be determined from two-dimensional shock tables (ref. 16), but the means of obtaining the overall pressure rise $\left(\frac{p_{l,3}}{p_{l,1}}\right)_b$ through the equivalent boundary layer is more complicated. The pressure changes in the boundary layer include pressure ratios associated with converting the real boundary layer to one-dimensional flow and back again. The overall pressure rise through the boundary layer is as follows:

$$\left(\frac{p_{l,3}}{p_{l,1}}\right)_b = \left(\frac{p_e}{p_l}\right)_1 \frac{p_{e,3}}{p_{e,1}} \frac{1}{\left(\frac{p_e}{p_l}\right)_3} \tag{4}$$

As outlined in the previous section, the value of the ratio $\left(\frac{p_e}{p_l}\right)_1$ can be determined from the values of $M_{l,1}$ and N_1 which are known. The net pressure rise through the boundary-layer shocks $\frac{p_{e,3}}{p_{e,1}}$ (which includes the wall shock with a turning of $\alpha_b + \alpha_b'$, the incident shock with a turning of α_b and an expansion with turning of α_b') is a function of the unknown turning angle α_b. The pressure ratio $\left(\frac{p_e}{p_l}\right)_3$ cannot be evaluated until the station 3

equivalent Mach number $M_{e,3}$ is known and $M_{e,3}$ also is a function of α_b. A trial-and-error method of solution must be used where an arbitrary series of values of α_b are assumed. For each value of α_b, the ratio $\frac{p_{e,3}}{p_{e,1}}$ is determined from figures 7 and 5 and from equation (3). The value of α_b is selected from the series of values assumed either by graphical or analytical procedures which satisfy the criteria

$$\left(\frac{p_{l,3}}{p_{l,1}}\right)_l = \left(\frac{p_{l,3}}{p_{l,1}}\right)_b$$

The selected values of α_b will correspond to specific values of $M_{e,3}$ and N_3 where $M_{e,3}$ is a result of the two-dimensional boundary-layer shock calculations and N_3 is determined from figure 7. Experimental data show that the value of N_3 so determined is equal to N_d.

Geometry of Analytical Shock Model

The mass-flow addition to the boundary layer due to turbulent mixing through the shock system is essential in the accurate calculation of the boundary-layer thickness change across the shocks. The method chosen for the calculation of this mass-flow addition has certain empirical features; therefore, a boundary-layer shock model as similar as possible to that of the actual flow is used. Schematics of this shock model are presented for a weak incident shock in figure 8 and for a strong incident shock in figure 9. One of the critical dimensions in the diagrams of figures 8 and 9 is the distance from the wall to the intersection of the incident and wall shocks; the intersection point is within the boundary layer in figure 8 and external to the boundary layer in figure 9. This dimension Y_1, as well as other important dimensions of the shock model required to determine the boundary-layer shock geometry, is not amenable to determination by analysis. Therefore, an empirical representation for Y_1, as well as for two other important dimensions of interest L_u and L_t, is developed by using data from references 4, 5, 10, 12, 17 to 22, data obtained at Ames and Langley Research Centers, and data obtained by General Dynamics under contract NAS1-3489. The dimensions L_u and L_t are, as defined in figure 1, the upstream and total lengths of the pressure gradient imposed on the wall by the shocks.

The determination of Y_1, or $\frac{Y_1}{\delta_1}$, is accomplished through the use of an empirically determined curve for $\frac{Y_1}{L_u}$ and a family of empirically determined curves for $\frac{L_u}{\delta_1}$. The correlation curve for $\frac{Y_1}{L_u}$ is presented in figure 10

where $\frac{Y_1}{L_u}$ is given as a function of $\frac{\Delta p}{q_{l,1}}$; the parameter Δp is the theoretical overall static-pressure rise across the incident and reflecting shocks external to the boundary layer. No systematic trends with changes in Mach or Reynolds numbers are detectable for $\frac{Y_1}{L_u}$. The family of curves for the nondimensional upstream length of the interaction region $\frac{L_u}{\delta_1}$ is taken from cross-plots of the aforementioned references and are presented in figure 11(a). In the curves of figure 11(a), $\frac{\Delta p}{q_{l,1}}$ is again the independent parameter and the curves are for given values of M_l and R_θ at station 1. To avoid confusion, no data points are shown in figure 11(a); the correspondence with experimental data is presented in figure 11(b).

In figures 12(a) to 12(c) cross-plots of the nondimensional length parameter $\frac{L_t}{\delta_1}$ were obtained by using the data of references 4, 5, 10, 12, 17, 18, 19, and 22, and unpublished data obtained at Ames Research Center. The range of Reynolds number, Mach number, and turning angle of the experimental data used to determine the correlations of the shock-interaction length parameter $\frac{L_t}{\delta_1}$ is presented in table I. The points identified in figures 12(a) to 12(c) by symbols are not experimental points but points from cross-plotted experimental data. The limit curve shown for attached shocks in figure 12(a) was determined from figure 4 of reference 23 corresponding to wedges. Figure 12(c) shows that extrapolation of experimental results obtained for $\frac{L_t}{\delta_1}$ to Reynolds numbers not covered by experimental data is not advisable.

TABLE I.- RANGE OF VARIABLES USED IN EMPIRICAL DETERMINATION OF $\frac{L_t}{\delta_1}$ CURVES

Reference	Mach number range	Turning angle range	Reynolds number range, R_δ
Unpublished Ames data	2.38 to 4.02	8° to 12.5°	1.95×10^4 to 7.5×10^4
28	2.95 to 4.80	6° to 9.5°	1.18×10^4 to 1.60×10^5
5	2.97	7° to 12°	2.65×10^5
4	2.99	4° to 10°	1.60×10^5
13	1.44	1.5° to 6.5°	1.49×10^4
9	3.85	4° to 10°	5.15×10^5
11	2.99	8.4° to 11.6°	5.81×10^4
22	3.0	6.6° to 8.1°	3.14×10^5
18	3.0	6.6° to 8.0°	3.98×10^5

In summary, the determination of the important length parameters Y_1, L_u, and L_t of the shock model is accomplished through the use of the empirical curves of figures 10, 11, and 12. The determination of these length parameters, in conjunction with the equivalent one-dimensional flow properties at station 1 and the turning angles α_b and α_b', provide sufficient information to determine shock diagrams similar to those of figures 8 and 9, either analytically or graphically, upon using conventional shock tables (ref. 16) to determine the shock angles.

Boundary-Layer Thickness Change

The initial step required to determine the boundary-layer thickness change between stations 1 and d is the determination of the mass-flow addition to the boundary layer between stations 3 and d. (See fig. 1.) It was found that the height of the void region at station d' is a direct measure of this mass-flow addition to the boundary layer. Station d' is defined as the station at the point where the wall shock intersects the edge of the boundary layer or at the point where the incident shock intersects the edge of the void region, whichever is further downstream. The mass-flow addition is computed by using the equivalent flow conditions at station d' in conjunction with the height of the void region at station d'. Therefore, the ratio of mass flow at station d to that at station 1 is given by

$$\frac{w_d}{w_1} = \frac{p_{e,d'}}{p_{e,1}} \frac{M_{e,d'}}{M_{e,1}} \left(\frac{1 + \frac{\gamma - 1}{2} M_{e,d'}^2}{1 + \frac{\gamma - 1}{2} M_{e,1}^2} \right)^{1/2} \frac{\delta_{d'}}{\delta_1} \tag{5}$$

where all the values of the equivalent flow parameters are obtained by the method outlined in a previous section. The quantity $\frac{\delta_{d'}}{\delta_1}$ can be evaluated graphically or analytically by the methods outlined in appendix B.

The boundary-layer thickness ratio $\frac{\delta_d}{\delta_1}$ can be evaluated by the following equation:

$$\frac{\delta_d}{\delta_1} = \frac{w_d}{w_1} \frac{p_{l,1}}{p_{l,d}} \frac{M_{l,1}}{M_{l,d}} \left(\frac{1 + \frac{\gamma - 1}{2} M_{l,1}^2}{1 + \frac{\gamma - 1}{2} M_{l,d}^2} \right)^{1/2} \frac{\left(\frac{m}{m_l} \right)_1}{\left(\frac{m}{m_l} \right)_d} \tag{6}$$

where the values of all parameters were determined previously. Specifically, the values of $\left(\frac{m}{m_l} \right)_1$ and $\left(\frac{m}{m_l} \right)_d$ are determined from figure 4 corresponding, respectively, to N_1 and N_d.

Boundary-Layer Growth Downstream of Station d

In the determination of the growth of the turbulent boundary layer through an incident-reflecting shock system, the development of the turbulent boundary layer should be considered from station 1 to some downstream station where the velocity profile has returned to approximately an equilibrium profile. The choice of this downstream station is necessary because at the point on the wall where the theoretical static-pressure rise through the shocks has been realized, station d, the boundary-layer velocity profile may be very distorted and thus N_d will be considerably lower than the corresponding equilibrium value. Thus, the next step in estimating the boundary-layer growth must include a means to determine the distance from station d to the station where the velocity profile has reached a near-equilibrium value. This step should also include a means of determining the velocity-profile development as well as the changes in important boundary-layer parameters through this mixing region.

An empirical equation for the change in the boundary-layer shape parameter in the mixing region downstream of station d is presented in reference 24 for incompressible flow:

$$\frac{H}{H_{1/7}} - 1 = \left(\frac{H_d}{H_{1/7}} - 1\right) e^{-K\frac{\Delta x}{\delta_d}} \tag{7}$$

It was assumed in reference 24 that the equilibrium profile would correspond to an N of 7 and that K has a value of 0.23 for incompressible pipe flow. Equation (7) presents a means for determining both the required length of the mixing region and the velocity-profile development through the mixing region. However, as shown in figures 2 and 3, the equilibrium value of N is a function of Reynolds number and does not necessarily have a value of 7; therefore, equation (7) is modified as follows:

$$\frac{H}{\left(H_{eq}\right)_d} - 1 = \left[\left(\frac{H}{H_{eq}}\right)_d - 1\right] e^{-K\frac{\Delta x}{\delta_d}} \tag{8}$$

The equilibrium shape parameter $\left(H_{eq}\right)_d$ corresponds to the equivalent Reynolds number $\left(R_{xe}\right)_d$ which can be evaluated from $R_{\theta,d}$ by using the procedure given in appendix C. The constant K has been evaluated from the data of references 5, 25, 26, 27, 20, 24, and 28 and from data obtained under contract NAS1-3489; the results are presented in figure 13. The values of the shape parameter H $\left(\text{which is equal to } \frac{\delta^*}{\theta}\right)$ used in equation (8) to solve for the experimental values of K presented in figure 13 were obtained from figure 14 by using the experimental values of N through the constant-pressure mixing region. The equilibrium profile index N_{eq} used in equation (8) for the determination of experimental points of figure 13 corresponds to the Reynolds

number R_θ of the most upstream experimentally investigated point of the constant-pressure mixing region.

Equation (8) indicates that Δx may approach infinity before an equilibrium profile is reached. In order to obtain a practical solution as to the necessary length of the constant-pressure mixing zone, it is arbitrarily assumed that the shape factor H is allowed to develop until it has a value equal to $H_{eq} + 0.10(H_d - H_{eq,d})$. By using this assumption equation (8) can be rearranged to give

$$\frac{L_{eq}}{\delta_d} = \frac{2.302}{K} \tag{9}$$

where L_{eq} is a specific value of Δx. Equation (9) provides a means for estimating the length L_{eq} downstream of station d required to reach a near-equilibrium shape factor. The value of K corresponding to the value of N_{eq} chosen for station d is determined from figure 13. The value of N_{eq} chosen for station d is the value of the profile index which would be obtained on a flat plate with the same value of R_θ as station d; the details of obtaining N_{eq} and thus H_{eq} are presented in appendix C.

The longitudinal station at distance L_{eq} downstream of station d is assumed to correspond to an equilibrium shape factor and is designated station E. The increase in the boundary-layer thickness between stations d and E is produced by the mixing (in addition to the mixing between stations 3 and d) of a significant amount of free-stream flow with the boundary layer to produce a near-equilibrium velocity profile at station E. This thickness change can be evaluated by assuming a constant-pressure process and by omitting the effects of wall friction. Since with these assumptions there are no external forces on the boundary layer between stations d and E, there is no change in the integrated momentum of the boundary layer and thus no change in the momentum thickness θ. Therefore, the boundary-layer thickness calculation is as follows:

$$\frac{\delta_E}{\delta_d} = \frac{\frac{\theta_E}{\delta_d}}{\left(\frac{\theta}{\delta}\right)_E} = \frac{\left(\frac{\theta}{\delta}\right)_d}{\left(\frac{\theta}{\delta}\right)_E} \tag{10}$$

The value $\left(\frac{\theta}{\delta}\right)_E$ corresponds to the equilibrium value of N at station d and its corresponding N_{φ/φ_l}. The value of equilibrium N at station d was previously described in connection with equation (8) but the corresponding value of N_{φ/φ_l} is obtained from the empirically determined curve of figure 15. (Example experimental data are also shown in fig. 15.) The value of the profile index N_{φ/φ_l} of figure 15 associated with each value of N and thus each actual velocity profile is chosen to be the value of N which corresponds to

an exponential profile having a value of $\frac{\varphi}{\varphi_l} = \int_0^1 \frac{\rho_b V_b^2}{\rho_l V_l^2} d\left(\frac{y}{\delta}\right)$ identical with that of the actual boundary layer. Since the curve of figure 15 also holds for nonequilibrium zero-pressure-gradient velocity profiles, the values of $\left(\frac{\theta}{\delta}\right)_d$ and $\left(\frac{\theta}{\delta}\right)_E$ are then evaluated by using figures 4 and 5 and the correct values of N and N_{φ/φ_l} along with the expression

$$\frac{\theta}{\delta} = \frac{m}{m_l} - \frac{\varphi}{\varphi_l} \tag{11}$$

As noted, the preceding calculation omits the growth in the momentum thickness θ due to wall friction along the mixing length. If desired, this effect can be estimated by using standard methods for evaluating the friction coefficient and the results are modified accordingly.

The length estimated by equation (9) when added to the length L_t of figures 12(a) to 12(c) provides an estimate of the overall length of run of boundary layer disturbed by an incident-reflecting shock. The thickness ratio $\frac{\delta_E}{\delta_d}$ evaluated by equation (10), when multiplied by the value of $\frac{\delta_d}{\delta_1}$ of equation (6), provides a means of determining the overall thickness change chargeable to an incident-reflecting shock. Also shown by this section is that two successive incident shocks, designated A and B, which might occur in an inlet compression field, for instance, should be separated by a distance D where

$$D = \left(L_t - L_u\right)_A + L_{eq} + L_{u,B} \tag{12}$$

if an equilibrium velocity profile is to enter shock B.

RESULTS AND DISCUSSION

Profile Index Change

The present method for calculating the change in velocity profile across an incident-reflecting shock is based on the assumption of exponential turbulent velocity profiles; the exponent N was selected as the profile index. The values of N used in the method correspond to a mathematically exact exponential profile having the same $\frac{m}{m_l}$ as the actual profile. Since turbulent boundary-layer velocity profiles are not exactly exponential, the accuracy of the results obtained by using this assumption is of interest. Figure 16 presents a comparison of experimental values of profile index at station d of

references 4, 5, and 25 as well as the data obtained under contract NAS1-3489 with curves computed by the present method. A portion of the experimental data presented in figure 16 has nonequilibrium upstream velocity profiles; these data are identified on the figure. The greatest discrepancy between data and curves is approximately 10 percent which is considered to be ample substantiation of the method.

The changes in profile index parameters across incident-reflecting shocks have been computed by procedures outlined in previous sections for a systematic variation in values of the prime variables. These variables include incident shock-turning angle or pressure ratio, upstream Mach number, and upstream profile index N_1. The purpose of the computations is to illustrate in detail the effects of the independent parameters and to furnish values of parameters to be used in the application of the method. The computed values of the profile index N_d are presented in figures 17(a) to 17(c) for N_1 values of 5, 7, and 9, respectively. The profile index N_d curves of figures 17(a) to 17(c) are presented as a function of overall pressure ratio $\frac{p_{l,d}}{p_{l,1}}$ for curves of constant Mach number $M_{l,1}$; superimposed on figures 17(a) to 17(c) are curves of constant turning angle α_l. Results show that the profile index when expressed as a function of pressure ratio is a strong function of Mach number. However, a study of the slopes of the shock-turning-angle curves shows that most of the Mach number dependence would be removed by expressing N_d as a function of α_l; in fact, N_d was deliberately plotted against $\frac{p_{l,d}}{p_{l,1}}$ to spread the curves for constant Mach number for easy viewing. Results also show that the profile index N_d is a strong function of upstream profile index N_1; N_d increases substantially as N_1 increases from 5 to 9 for the same $M_{l,1}$ and $\frac{p_{l,d}}{p_{l,1}}$.

The computations for N_d do not extend below a value of 1.23 because according to reference 29, separation will always occur for lower values of N, at least for incompressible flow. An empirical curve for compressible turbulent boundary-layer separation under incident-reflecting shocks derived from reference 10 is given in figure 17(b) for N_1 of 7. The method used for converting the data of reference 10 to the variables of figure 17(b) is given in appendix D. This separation curve indicates that separated flow occurs somewhere in the shock system for values of N_d ranging from 2 to 3 whereas incompressible criteria of reference 29 indicate that the flow at station d would have reattached for these cases.

Changes in Boundary-Layer Thickness Parameters

From Station 1 to Station d

The experimental boundary-layer thickness change data of references 4, 5, 17, and 21 as well as data obtained under contract NAS1-3489 are compared in

figure 18 with curves computed by using the present method; figure 18 presents calculated and experimental thickness changes as a function of free-stream turning angle α_l. Some of these data do not correspond to equilibrium boundary-layer velocity profiles at station 1 (fig. 1); these nonequilibrium data are identified on the figure. In these cases the curve representing the present method was computed by using the actual values of N_1 and R_θ and satisfactory agreement was obtained. All other data of figure 18 correspond to equilibrium velocity profiles at station 1. Agreement with data is within 10 percent which is considered to be adequate substantiation of the method.

The results of systematic computations of the boundary-layer thickness change across incident-reflecting shocks are given in figures 19(a) to 19(c), respectively, for N_1 values of 5, 7, and 9 and R_{xe} values of 3.3×10^5, 3.3×10^6, and 3.3×10^7; these curves are for equilibrium boundary-layer velocity profiles at station 1. The calculations were limited to Mach numbers $M_{l,1}$ up to 5.0 because of the limitations of the empirical correlation of $\frac{L_u}{\delta_1}$ of figure 11(a). In general, the curves of $\frac{\delta_d}{\delta_1}$ decrease initially, go through a minimum, and then increase as α_l is further increased. The increasing values of $\frac{\delta_d}{\delta_1}$ are caused by high rates of mass influx into the boundary layer produced by the severe distortion of boundary-layer velocity profiles at high turning angles. The results show the turning angle α_l corresponding to minimum values of $\frac{\delta_d}{\delta_1}$ generally increases with Mach number $M_{l,1}$. The results also show the effect of Reynolds number or N_1 on the boundary-layer thickness ratio $\frac{\delta_d}{\delta_1}$ is small for equilibrium velocity profiles at station 1.

A separation curve corresponding to that of figure 17(b) is shown on figure 19(b); in general, separation occurs under the shock at higher values of turning angle than those corresponding to minimum values of $\frac{\delta_d}{\delta_1}$. In inlet design, however, shock-turning angles smaller than those corresponding to minimum $\frac{\delta_d}{\delta_1}$ values are generally of interest because of a need of higher total-pressure recoveries in the inviscid flow than could be obtained with the shock-turning angles corresponding to minimum $\frac{\delta_d}{\delta_1}$ values.

The results of computations of the momentum thickness change $\frac{\theta_d}{\theta_1}$ and displacement thickness change $\frac{\delta^*_d}{\delta^*_1}$ corresponding to the boundary-layer thickness change curves of figures 19(a) to 19(c) are presented, respectively, in

figures 20(a) to 20(c) and 21(a) to 21(c); these curves are also for equilibrium profiles at station 1. The curves of figures 20 and 21 were calculated by using the following equations:

$$\left.\begin{aligned} \frac{\theta_d}{\theta_1} &= \frac{\left(\frac{\theta}{\delta}\right)_d}{\left(\frac{\theta}{\delta}\right)_1} \frac{\delta_d}{\delta_1} \\ \frac{\delta^*_d}{\delta^*_1} &= \frac{\left(\frac{\delta^*}{\delta}\right)_d}{\left(\frac{\delta^*}{\delta}\right)_1} \frac{\delta_d}{\delta_1} \end{aligned}\right\} \tag{13}$$

The values of $\frac{\delta_d}{\delta_1}$ are obtained from figures 19(a) to 19(c) whereas the values of $\frac{\theta}{\delta}$ are determined from equation (11) and the values of $\frac{\delta^*}{\delta}$ are determined from the following equation:

$$\frac{\delta^*}{\delta} = 1 - \frac{m}{m_l} \tag{14}$$

The values of $\frac{m}{m_l}$ used in equations (11) and (14) are obtained from figure 4 by using, to determine station 1 values, the value of the profile index at station 1, N_1, and by using, to determine station d values, the value of the profile index at station d, N_d, obtained from figure 17. The values of $\frac{\varphi}{\varphi_l}$ used in equation (11) for stations 1 and d are obtained from figure 5 using the values of N_{φ/φ_l} determined from figure 15 corresponding to these N_1 and N_d values.

In general, the curves of $\frac{\theta_d}{\theta_1}$ and $\frac{\delta^*_d}{\delta^*_1}$ behave in a similar manner to those of the thickness change $\frac{\delta_d}{\delta_1}$ curves; however, the minimum values of both $\frac{\theta_d}{\theta_1}$ and $\frac{\delta^*_d}{\delta^*_1}$ occur at lower turning angles. This observation is important as shocks with turning angles smaller than those corresponding to the values obtained for the minimum values of $\frac{\delta_d}{\delta_1}$ are of major importance in inlet design.

Overall Development of a Boundary Layer

Through an Incident-Reflecting Shock

The intersection of an incident-reflecting shock with a turbulent boundary layer distorts the boundary-layer velocity profile and, as a result, the velocity profile at station d is not an equilibrium profile; the value of N_d is lower than the value of N_{eq}. The equilibrium profile index chosen for station d, as already pointed out, corresponds to the value of profile index which would be obtained on a flat plate with the same value of R_θ as station d. Appendix C, which presents the means of determining the chosen value of N_{eq} for station d, shows that the resulting equilibrium profile index is a function of the free-stream stagnation temperature $T_{l,t}$. The chosen value of N_{eq} at station d is used in the calculation of the overall changes in all the boundary-layer thickness parameters (δ, θ, and δ^*) from station 1 to the equilibrium station E downstream of station d. The chosen value of N_{eq} at station d is also used in the calculation of the nondimensional distance $\frac{L_{eq}}{\delta_1}$, the distance required for the distorted velocity profile at station d to return to an equilibrium profile. Therefore, as some insight into the overall effect of the intersection of a shock with a boundary layer is of interest, computations were made for the overall thickness changes $\frac{\delta_{eq}}{\delta_1}$, $\frac{\theta_{eq}}{\theta_1}$, and $\frac{\delta_{eq}^*}{\delta_1^*}$ as well as for the nondimensional distance $\frac{L_{eq}}{\delta_1}$ for a free-stream stagnation temperature of 310° K.

Computations for $\frac{L_{eq}}{\delta_1}$ were made by using equation (9) along with the values of $\frac{\delta_d}{\delta_1}$ obtained from figure 19; the results of these computations are presented in figures 22(a) to 22(c). The values of K (fig. 13) used in equation (9) correspond to a stagnation temperature of 310° K. The results of the computations of $\frac{L_{eq}}{\delta_1}$ show it behaves in the same manner as the thickness-change curves of figure 19; for example, the minimum values of each constant Mach number curve of $\frac{L_{eq}}{\delta_1}$ occur at almost the exact turning angle of the corresponding curve for $\frac{\delta_d}{\delta_1}$. A marked decrease in the value of $\frac{L_{eq}}{\delta_1}$ occurs with increases in Mach number $M_{l,1}$ or profile index N_1 $\left(\text{or } R_{xe}\right)$.

Computations of the thickness ratio $\frac{\delta_{eq}}{\delta_1}$ were conducted by using equation (10) and the curves for $\frac{\delta_d}{\delta_1}$ of figure 19. These computations were

conducted also for a free-stream stagnation temperature of 310° K and the results are presented in figures 23(a) to 23(c). As equation (10) ignores any change in momentum thickness between stations d and E (equilibrium profile station), the values of the ratio $\frac{\theta_{eq}}{\theta_1}$ would be identical with those for $\frac{\theta_d}{\theta_1}$ of figure 20. However, the improvement in the profile from station d to station E does result in a change in the values of the displacement thickness; therefore, as a knowledge of the overall effect of the shocks on the displacement thickness is also of general interest, computations for $\frac{\delta^*_{eq}}{\delta^*_1}$ were also made and are presented in figures 24(a) to 24(c). The computations for $\frac{\delta^*_{eq}}{\delta^*_1}$ were made by using the following equation:

$$\frac{\delta^*_{eq}}{\delta^*_1} = \frac{\left(\frac{\delta^*}{\delta}\right)_{eq}\left(\frac{\delta_{eq}}{\delta_1}\right)}{\left(\frac{\delta^*}{\delta}\right)_1} \tag{15}$$

where the values of $\frac{\delta^*}{\delta}$ are determined from equation (14) and the values of $\frac{\delta_{eq}}{\delta_1}$ are obtained from figure 23. The values of $\frac{m}{m_l}$ used in equation (14) are obtained from figure 4 by using, to determine the station 1 values, the value of the profile index at station 1 and by using, to determine the station E values, the value of the profile index N_{eq} incorporated in equation (10).

Upon comparing the results of the calculations for $\frac{\delta_{eq}}{\delta_1}$ (fig. 23) with the results of the calculations for $\frac{\delta_d}{\delta_1}$ (fig. 19), it can be seen that a considerable increase in boundary-layer thickness occurs between stations d and E. This is not the case, however, when the results of the calculations of $\frac{\delta^*_{eq}}{\delta^*_1}$ (fig. 24) are compared with the results of the calculations of $\frac{\delta^*_d}{\delta^*_1}$ of figure 21; the improvement in profile between stations d and E causes a decrease in the displacement thickness.

Practical Application Procedure for Changes in Profile Index and Thickness Parameters

In order to utilize in a practical problem the various thickness parameter change curves which are furnished, two assumptions have to be made as to the boundary-layer flow problem being considered. First, the boundary-layer flow has to be assumed to be turbulent; and second, the boundary-layer flow

upstream of the incident-reflecting shock interaction with the boundary layer has to have an equilibrium flat-plate (zero pressure gradient) flow velocity profile. The calculation across the incident-reflecting shock when the furnished curves are used then follows these steps:

(1) The momentum thickness at station 1 (fig. 1) is calculated by the most accurate means available and the value of $R_{\theta 1}$ is determined.

(2) By using the procedure outlined in appendix C, the Reynolds number $R_{\theta 1}$ is converted to R_{xe} and the equilibrium profile index $N_{eq,1}$ for station 1 is determined from figures 2 and 3. The value of $(N_{eq,1})_{\varphi,\varphi_1}$ is then obtained from figure 15 corresponding to $N_{eq,1}$.

(3) The values of the boundary-layer thickness δ_1 and displacement thickness δ_1^* at station 1 can then be computed through the use of θ_1 along with equations (11) and (14).

(4) The change in the thickness parameters δ, δ^*, and θ across an incident-reflecting shock with an incident shock-turning angle α_l is then determined from the appropriate set of curves (figs. 19(a) to 19(c) or 23(a) to 23(c); 20(a) to 20(c); 21(a) to 21(c) or 24(a) to 24(c)) by the use of $N_{eq,1}$, α_l, and $M_{l,1}$. The change in the profile index across an incident-reflecting shock of incident shock turning angle α_l is determined from the set of profile index change curves (figs. 17(a) to 17(c)) by using $N_{eq,1}$, $\frac{p_{l,d}}{p_{l,1}}$, and $M_{l,1}$.

(5) The value of the thickness parameter of interest downstream of the shock, whether at station d or station E, is obtained through multiplication of its station 1 value times the change read from the appropriate set of curves.

An example calculation using this step-by-step outline is presented in complete detail in appendix E.

CONCLUDING REMARKS

There are two important features of the present method of calculation of the changes in a boundary layer across an incident-reflecting shock which enhance its value over that of previous methods. The first of these features is that the profile index change, and thus the profile change calculation, requires no information or knowledge of the boundary-layer thickness change. The second of these features is that a boundary-layer shock model is assumed to be of a type consistent with the boundary-layer development and shock configuration revealed by shadowgraph and schlieren observations of the actual phenomena.

Utilization of the two features stated in the previous paragraph in the calculation of the profile index change and boundary-layer thickness change give good agreement with data. For example, values of the profile index change calculated at Mach numbers 1.9 to 3.0 and turning angles up to 11° are found to agree with the data to within 10 percent or better; boundary-layer thickness-change data in the Mach number range 1.9 to 3.85, Reynolds number range (based on an equivalent length) of 10^7 to 10^8, and for turning angles through the free-stream incident shock up to 13° also correlate to within 10 percent.

The results of systematic computations of important boundary-layer parameter changes from upstream of the shocks to two selected stations downstream of the shocks are presented in the form of curves which can be used for direct application. The two selected stations consist of the point where the theoretical maximum pressure rise occurs on the wall and the point where the boundary-layer flow returns to an equilibrium profile. For these stations, systematic computations were made for the boundary-layer thickness, momentum thickness, and displacement thickness. In addition to the previously mentioned computations, systematic computations for the profile index at the theoretical maximum pressure point were made. Because of the limits imposed by experimental data for important empirical parameters, the present method of calculation is generally limited to a maximum Mach number of 5.0.

Systematic computations were also made for the nondimensional length parameter $\frac{L_{eq}}{\delta_1}$. This parameter is defined as the length of plate required for the distorted boundary layer at the maximum pressure point downstream of the shocks to return to an equilibrium velocity profile. As was done in the thickness-change calculations, the calculations of $\frac{L_{eq}}{\delta_1}$ are also limited to a maximum Mach number of 5.0.

Langley Research Center,
National Aeronautics and Space Administration,
Langley Station, Hampton, Va., July 20, 1965.

APPENDIX A

DETERMINATION OF EQUIVALENT MACH NUMBER

A one-dimensional equivalent boundary-layer flow is derived as a function of the profile index N and free-stream Mach number M_l from equations for the total mass flow, momentum, and energy. The expression for the equivalent Mach number function of this equivalent one-dimensional boundary-layer flow as derived in the "mass momentum" method of reference 15 is

$$\frac{m\left(\frac{RT_{e,t}}{\gamma}\right)^{1/2}}{\Phi_b} = \frac{M_e\left(1 + \frac{\gamma - 1}{2} M_e^2\right)^{1/2}}{1 + \gamma M_e^2} \equiv f(M_e) \tag{A1}$$

where

$$m = m_l \frac{m}{m_l} = \frac{M_l}{\left(1 + \frac{\gamma - 1}{2} M_l^2\right)^{\frac{\gamma+1}{2(\gamma-1)}}} \left(\frac{\gamma}{RT_{l,t}}\right)^{1/2} \left(p_{l,t}\right) \frac{m}{m_l} \tag{A2}$$

and

$$\Phi_b = p_l\left(1 + \gamma M_l^2 \frac{\varphi}{\varphi_l}\right) = p_e\left(1 + \gamma M_e^2\right) \tag{A3}$$

In equations (A2) and (A3) the static pressure across the boundary layer is assumed to be constant and equal to the local free-stream static pressure.

In reference 15 the total temperature was assumed to be constant across the boundary layer but in the present method the total temperature is allowed to vary across the boundary layer and, thus, the energy equation must be included in the analysis. The energy equation with the equivalent total temperature incorporated is

$$\delta m T_{e,t} C_p = (mh)_b \delta + \frac{1}{2} \eta \delta \tag{A4}$$

where

$$(mh)_b = m_l h_l \int_0^1 \frac{\rho_b V_b}{\rho_l V_l} \frac{h_b}{h_l} d\left(\frac{y}{\delta}\right) \tag{A5}$$

and

$$\eta = \eta_l \frac{\eta}{\eta_l} \tag{A6}$$

After rearranging equation (A4) and assuming that the static enthalpy h is given by C_pT and that $\frac{V_b}{V_l} = \left(\frac{y}{\delta}\right)^{1/N}$, an expression for the equivalent total temperature is obtained:

$$T_{e,t} = T_l \frac{\frac{N}{N+1} + \frac{\gamma - 1}{2} M_l^2 \frac{\eta}{\eta_l}}{m/m_l} \tag{A7}$$

Substitute equations (A2), (A3), and (A7) into equation (A1) and rearrange to obtain an expression for the equivalent Mach number function $f(M_e)$ in terms of the profile index N and free-stream Mach number:

$$f(M_e) = \frac{M_l \left(\frac{m}{m_l}\right)^{1/2} \left(\frac{N}{N+1} + \frac{\gamma - 1}{2} M_l^2 \frac{\eta}{\eta_l}\right)^{1/2}}{1 + \gamma M_l^2 \frac{\varphi}{\varphi_l}} \tag{A8}$$

The parameters $\frac{m}{m_l}$, $\frac{\varphi}{\varphi_l}$, and $\frac{\eta}{\eta_l}$ are defined, respectively, as

$$\frac{m}{m_l} = \int_0^1 \frac{\rho_b V_b}{\rho_l V_l} d\left(\frac{y}{\delta}\right) = 1 - \frac{\delta^*}{\delta} \tag{A9}$$

$$\frac{\varphi}{\varphi_l} = \int_0^1 \frac{\rho_b V_b^2}{\rho_l V_l^2} d\left(\frac{y}{\delta}\right) = 1 - \frac{\delta^*}{\delta} - \frac{\theta}{\delta} \tag{A10}$$

$$\frac{\eta}{\eta_l} = \int_0^1 \frac{\rho_b V_b^3}{\rho_l V_l^3} d\left(\frac{y}{\delta}\right) \tag{A11}$$

The results of computations that were done for the parameters of equations (A9), (A10), and (A11) are presented in figures 4 to 6, respectively. The calculations of these parameters were performed on a digital computer by using the

following expressions for $\frac{V_b}{V_l}$ and $\frac{\rho_b}{\rho_l}$ given in reference 8 for adiabatic-wall conditions:

$$\left.\begin{aligned} \frac{V_b}{V_l} &= \left(\frac{y}{\delta}\right)^{1/N} \\ \frac{\rho_l}{\rho_b} &= \frac{T_b}{T_l} = 1 + \frac{\gamma - 1}{2} r M_l^2 \left[1 - \left(\frac{V_b}{V_l}\right)^2\right] \end{aligned}\right\} \tag{A12}$$

The value of γ is assumed to be 1.4 and the value of the adiabatic-wall recovery factor r is assumed to be 0.896.

APPENDIX B

EVALUATION OF BOUNDARY-LAYER THICKNESS $\frac{\delta_d'}{\delta_1}$

The evaluation of the boundary-layer thickness $\frac{\delta_d'}{\delta_1}$ by using the boundary-layer shock models of figures 8 and 9 requires the values of the shock-wave angles and the corresponding turning angles of the boundary-layer shock models as well as the value of $\frac{Y_1}{\delta_1}$ from figures 10 and 11. The shock-wave angles and the corresponding turning angles of the boundary-layer shock models are presented in the following table:

Shock-wave angle	Turning angle
$\beta_{b,1}$	α_b
$\beta'_{b,1}$	$\alpha_b + \alpha'_b$
$\beta_{b,2}$	$\alpha_b + \alpha'_b$
$\beta'_{b,2}$	α_b
$\beta'_{l,2}$	$\alpha_l + \alpha'_b$
$\beta_{l,1}$	α_l

The calculation of $\frac{\delta_d'}{\delta_1}$ using the values of the shock-wave angles and the corresponding turning angles of the boundary-layer shock models depends on which of the three cases is applicable. The three cases and the corresponding equation of $\frac{\delta_d'}{\delta_1}$ for each are:

Case 1: For $Y_1 < \delta_1$ where l_1 and l_2 are indicated in figure 8(b), if $l_2 \geqq l_1$, then $\frac{l_2}{\delta_1}$ is given by

$$\frac{l_2}{\delta_1} = \frac{Y_1/\delta_1}{\tan \beta'_{b,1}} + \frac{\sin\left(\beta_{b,1} - \alpha_b\right)\cos\left(\beta_{b,2} - \alpha_b\right)}{\sin \beta_{b,1} \sin \beta_{b,2}}\left(1 - \frac{Y_1}{\delta_1}\right) \tag{B1}$$

and $\frac{l_1}{\delta_1}$ is given by

$$\frac{l_1}{\delta_1} = \frac{Y_1}{\delta_1}\left\{\frac{1}{\tan \beta'_{b,1}} + \frac{1}{\tan\left[\beta'_{b,2} - \left(\alpha_b + \alpha'_b\right)\right]}\right\} \frac{\sin\left[\beta'_{b,2} - \left(\alpha_b + \alpha'_b\right)\right] \cos\left(\alpha_b + \alpha'_b\right)}{\sin \beta'_{b,2}} \tag{B2}$$

When l_2, l_1, and Y_1 satisfy the conditions of case 1, the following expression for $\frac{\delta'_d}{\delta_1}$ is used:

$$\frac{\delta'_d}{\delta_1} = \frac{\sin\left(\beta_{b,1} - \alpha_b\right)\sin\left(\beta_{b,2} - \alpha_b\right)}{\sin \beta_{b,1} \sin \beta_{b,2}}\left(1 - \frac{Y_1}{\delta_1}\right) + \frac{Y_1}{\delta_1} \tag{B3}$$

Case 2: For $l_2 < l_1$ and $Y_1 \leqq \delta_1$ (fig. 8; eqs. (B1) and (B2) are used for $\frac{l_2}{\delta_1}$ and $\frac{l_1}{\delta_1}$), the following equation for $\frac{\delta'_d}{\delta_1}$ is used:

$$\frac{\delta'_d}{\delta_1} = \frac{\sin\left(\beta_{b,1} - \alpha_b\right)\sin\left(\beta_{b,2} - \alpha_b\right)}{\sin \beta_{b,1} \sin \beta_{b,2}}\left(1 - \frac{Y_1}{\delta_1}\right) + \frac{Y_1}{\delta_1} + \frac{l_1 - l_2}{\delta_1} \tan \alpha'_b \tag{B4}$$

Case 3: For $l_2 < l_1$ and $Y_1 > \delta_1$ (l_2 and l_1 are indicated in fig. 9(b)), the following equation for $\frac{\delta'_d}{\delta_1}$ is used:

$$\frac{\delta'_d}{\delta_1} = \frac{\sin\left[\beta_{l,1} - \left(\alpha_b + \alpha'_b\right)\right]\sin\left[\beta_{l,2} - \left(\alpha_l + \alpha'_b\right)\right]}{\sin \beta'_{l,1} \sin\left[\beta_{l,2} - \left(\alpha_l - \alpha_b\right)\right]}\left(1 - \frac{Y_1}{\delta_1}\right) + \frac{Y_1}{\delta_1} + \frac{l_1 - l_2}{\delta_1} \tan \alpha'_b \tag{B5}$$

with $\frac{l_2}{\delta_1}$ given by

$$\frac{l_2}{\delta_1} = \frac{\frac{\sin\left[\beta'_{l,1} - \left(\alpha_b + \alpha'_b\right)\right]\sin\left[\beta_{l,2} - \left(\alpha_l + \alpha'_b\right)\right]}{\sin \beta'_{l,1} \sin\left[\beta_{l,2} - \left(\alpha_l - \alpha_b\right)\right]}\left(1 - \frac{Y_1}{\delta_1}\right) + \frac{Y_1}{\delta_1} - 1}{\tan\left(\alpha_b + \alpha'_b\right)} + \frac{1}{\tan \beta'_{b,1}} \tag{B6}$$

and $\frac{l_1}{\delta_1}$ given by

$$\frac{l_1}{\delta_1} = \frac{\sin\left[\beta'_{b,2} - \left(\alpha_b + \alpha'_b\right)\right]\cos\left(\alpha_b + \alpha'_b\right)}{\sin \beta'_{b,2}}$$

$$\times \left\{ \frac{l_2}{\delta_1} + \frac{\dfrac{\sin\left[\beta'_{l,1} - \left(\alpha_b + \alpha'_b\right)\right]\sin\left[\beta_{l,2} - \left(\alpha_l + \alpha'_b\right)\right]}{\sin \beta'_{l,1} \sin\left[\beta_{l,2} - \left(\alpha_l - \alpha_b\right)\right]}\left(1 - \frac{Y_1}{\delta_1}\right) + \frac{Y_1}{\delta_1}}{\tan\left[\beta'_{b,2} - \left(\alpha_b + \alpha'_b\right)\right]} \right\} \qquad \text{(B7)}$$

APPENDIX C

DETERMINATION OF EQUIVALENT FLAT-PLATE REYNOLDS NUMBER

By definition, the flat-plate equivalent Reynolds number R_{xe} for a given boundary-layer station is the Reynolds number based on the length of flat plate (zero pressure gradient) x_e required for turbulent flow to produce the same R_θ, as the flow in question, at the local free-stream Mach number and total temperature. Based on this definition of R_{xe}, and the following assumptions for the average incompressible friction coefficient and the ratio of compressible to incompressible turbulent friction coefficient,

$$C_{F,i} = \frac{2\theta_i}{x_e} = \frac{0.472}{\left(\log_{10} R_{\theta i} - \log_{10} \frac{C_{F,i}}{2}\right)^{2.58}} \tag{C1}$$

$$\frac{C_F}{C_{F,i}} = \frac{\theta}{\theta_i} \tag{C2}$$

the expression for R_{xe} is given by

$$R_{xe} = \frac{R_\theta}{\frac{C_F}{C_{F,i}} \frac{C_{F,i}}{2}} \tag{C3}$$

The incompressible average turbulent friction coefficient $C_{F,i}$ is obtained from figure 25(a), which is based on equation (C1), by using the value of $R_{\theta i}$ given by

$$R_{\theta i} = \frac{R_\theta}{C_F/C_{F,i}} \tag{C4}$$

The ratio of compressible to incompressible friction coefficient $\frac{C_F}{C_{F,i}}$ as obtained from reference 30 is given in figures 26(a) to 26(c) as a function of R_θ, M_l, and $T_{l,t}$. The flat-plate equilibrium flow profile index N_{eq} and equilibrium flow shape parameter $(H_{eq})_a$ can then be determined by the use of figures 2, 3, and 14.

APPENDIX D

DETERMINATION OF REYNOLDS NUMBER $R_{\delta''}$

Reference 10 gives empirical curves, for boundary-layer separation, of the incident shock-turning angle as a function of Mach number and Reynolds number $R_{\delta''}$; the thickness δ'' corresponds to the point in the boundary layer where $\frac{V_b}{V_l} = 0.99$. Thus, in order to utilize the empirical curves of reference 10 to determine the separation curve of figure 17(b), a value of $R_{\delta''}$ had to be determined corresponding to each Mach number and an N_1 value of 7. The value of $R_{\delta''}$ is calculated by using figures 2, 3, 4, 5, 15, 25(b), 27, and 28(a) to 28(c) along with the profile index given in the text. Figure 27 shows the empirically determined relationship (along with some example experimental data) between the equilibrium profile index N_{eq} and the ratio $\frac{\delta''}{\delta}$; figures 28(a) to 28(c) give the ratio of compressible to incompressible friction coefficient $\frac{C_F}{C_{F,i}}$ in terms of $R_{\theta i}$, M_l, and $T_{l,t}$ as obtained from reference 30.

The value of R_θ is determined from figures 2, 3, 25(b), and 28(a) to 28(c) along with the following relationships:

$$R_{\theta i} = \left(R_{xe}\right)_{N=7}\left(\frac{C_{F,i}}{2}\right) \tag{D1}$$

$$C_{F,i} = \frac{0.472}{\left(\log_{10} R_{xe}\right)^{2.58}}$$

$$R_\theta = R_{\theta i}\left(\frac{\theta}{\theta_i}\right) = R_{\theta i}\left(\frac{C_F}{C_{F,i}}\right) \tag{D2}$$

The value of $\frac{\theta}{\delta}$ is given by the relationship

$$\frac{\theta}{\delta} = \frac{m}{m_l} - \frac{\varphi}{\varphi_l} \tag{D3}$$

where the value of $\frac{m}{m_l}$ is determined from figure 4 by using the value of M_l and $N = 7$ and the value of $\frac{\varphi}{\varphi_l}$ is determined from figure 7 by using the value of M_l along with the value of N_{φ/φ_l} given by the empirically determined curve of figure 15. The value of $R_{\delta''}$ is then given by

$$R_{\delta''} = \frac{R_\theta}{\frac{\theta}{\delta}} \frac{\delta''}{\delta} \tag{D4}$$

where $\frac{\theta}{\delta}$ is determined from equation (D3) and the value of $\frac{\delta''}{\delta}$ is obtained from figure 27 and corresponds to the value of $N = 7$.

APPENDIX E

EXAMPLE CALCULATION USING FURNISHED BOUNDARY-LAYER THICKNESS-PARAMETER-CHANGE CURVES

The following example calculation which follows the step-by-step procedure as stated in the text and which utilizes the various thickness-parameter-change curves furnished is presented:

(1) The boundary-layer conditions at station 1 are:

$M_{l,1} = 3.0$

$T_{l,t} = 310^{\circ}$ K

$\theta_1 = 8.265 \times 10^{-6}$ meter

$p_{l,t} = 6.895 \times 10^{5} \frac{\text{newtons}}{\text{meter}^2}$

$R_{\theta 1} = 4.07 \times 10^{3}$ (as determined from ref. 23)

Incident shock-turning angle $\alpha_l = 8^{\circ}$

(2) Determination of R_{xe}: Equation (C3) gives

$$R_{xe} = \frac{R_\theta}{\frac{C_F}{C_{F,i}} \frac{C_{F,i}}{2}} = 3.3 \times 10^{6}$$

For this example calculation, the value of $\frac{C_F}{C_{F,i}}$ is 0.66 and is determined from figure 26(a) by using $M_{l,1} = 3.0$ and $R_{\theta 1} = 4.07 \times 10^{3}$. The value of $C_{F,i}$ is determined from figure 25(a) by using equation (C4)

$$\left(R_{\theta i}\right)_1 = \frac{R_{\theta 1}}{\frac{C_F}{C_{F,i}}} = 6.17 \times 10^{3}$$

Determination of $N_{eq,1}$: The determination of $N_{eq,1}$ is accomplished through two steps: (1) enter figure 2 with $R_{xe} = 3.3 \times 10^6$ to obtain $N_{L,1} = 6.1$; (2) enter figure 3 with $N_{L,1} = 6.1$ to obtain $N_{eq,1} = 7.0$.

Determination of $\left(N_{eq,1}\right)_{\varphi/\varphi_l}$: Enter figure 15 with $N_{eq,1} = 7.0$ to obtain $\left(N_{eq,1}\right)_{\varphi/\varphi_l} = 7.14$.

(3) Determination of δ_1: Equation (11) gives

$$\frac{\theta}{\delta} = \frac{m}{m_l} - \frac{\varphi}{\varphi_l}$$

In order to determine $\left(\frac{\theta}{\delta}\right)_1$ from equation (11), enter figure 4 with $N_{eq,1} = 7.0$ and $M_{l,1} = 3.0$ to obtain $\left(\frac{m}{m_l}\right)_1$; then enter figure 5 with $\left(N_{eq,1}\right)_{\varphi/\varphi_l} = 7.14$ and $M_{l,1} = 3.0$ to obtain $\left(\frac{\varphi}{\varphi_l}\right)_1$. Then $\left(\frac{\theta}{\delta}\right)_1$ is given by

$$\left(\frac{\theta}{\delta}\right)_1 = \left(\frac{m}{m_l}\right)_1 - \left(\frac{\varphi}{\varphi_l}\right)_1 = 0.6852 - 0.6202 = 0.0650$$

The boundary-layer thickness δ_1 is then equal to

$$\delta_1 = \frac{\theta_1}{\left(\frac{\theta}{\delta}\right)_1} = 1.272 \times 10^{-4} \text{ meter}$$

Determination of δ_1^*: Equation (14) gives

$$\frac{\delta^*}{\delta} = 1 - \frac{m}{m_l}$$

Utilizing the information presented in step 3 yields

$$\left(\frac{\delta^*}{\delta}\right)_1 = 1 - \left(\frac{m}{m_l}\right)_1 = 1 - 0.6852 = 0.3148$$

and the value of δ^*_1 is given by

$$\delta^*_1 = \delta_1\left(\frac{\delta^*}{\delta}\right)_1 = 4.002 \times 10^{-5} \text{ meter}$$

(4) Change in thickness parameters δ, δ^*, and θ:

(a) Change in δ: Enter figures 19(b) or 23(b) (curves for $N_{eq,1} = 7.0$) with $M_{l,1} = 3.0$ and $\alpha_l = 8^\circ$ to obtain $\frac{\delta_d}{\delta_1} = 0.716$ or $\frac{\delta_{eq}}{\delta_1} = 0.968$.

(b) Change in θ: Enter figure 20(b) (curves for $N_{eq,1} = 7.0$) with $M_{l,1} = 3.0$ and $\alpha_l = 8^\circ$ to obtain $\frac{\theta_d}{\theta_1} = 1.076$. The momentum thickness change from station 1 to station E is assumed to be identical to the momentum thickness change from station 1 to station d.

(c) Change in δ^*: Enter figures 21(b) or 24(b) (curves for $N_{eq,1} = 7.0$) with $M_{l,1} = 3.0$ and $\alpha_l = 8^\circ$ to obtain $\frac{\delta^*_d}{\delta^*_1} = 0.866$ or $\frac{\delta^*_{eq}}{\delta^*_{eq}} = 0.712$.

(d) Change in N: Enter figure 17(b) (curves for $N_{eq,1} = 7.0$) with $M_{l,1} = 3.0$ and $\frac{p_{l,d}}{p_{l,1}} = 3.008$ (static-pressure rise through incident-reflecting shock with an incident shock-turning angle α_l of 8°) to obtain $N_d = 3.34$.

(5) The values of the thickness parameters δ_d, θ_d, and δ^*_d at station d are:

$$\delta_d = \delta_1 \frac{\delta_d}{\delta_1} = 9.11 \times 10^{-4} \text{ meter}$$

$$\theta_d = \theta_1 \frac{\theta_d}{\theta_1} = 8.90 \times 10^{-6} \text{ meter}$$

$$\delta^*_d = \delta^*_1 \frac{\delta^*_d}{\delta^*_1} = 3.468 \times 10^{-5} \text{ meter}$$

APPENDIX E

The values of the thickness parameters δ_{eq}, θ_{eq}, and δ^*_{eq} at station E are:

$$\delta_{eq} = \delta_1 \frac{\delta_{eq}}{\delta_1} = 1.233 \times 10^{-4} \text{ meter}$$

$$\theta_{eq} = 8.90 \times 10^{-6} \text{ meter}$$

$$\delta^*_{eq} = \delta^*_1 \frac{\delta^*_{eq}}{\delta^*_1} = 2.85 \times 10^{-5} \text{ meter}$$

REFERENCES

1. Ritter, Alfred; and Kuo, Yung-Huai: Reflection of a Weak Shock Wave From a Boundary Layer Along a Flat Plate. I - Interaction of Weak Shock Waves With Laminar and Turbulent Boundary Layers Analyzed by Momentum-Integral Method. NACA TN 2868, 1953.

2. Reshotko, Eli; and Tucker, Maurice: Effect of a Discontinuity on Turbulent Boundary-Layer-Thickness Parameters With Application to Shock-Induced Separation. NACA TN 3454, 1955.

3. Hammitt, Andrew G.: The Interaction of Shock Waves and Turbulent Boundary Layers. J. Aeron. Sci., vol. 25, no. 6, June 1958, pp. 345-356.

4. Kepler, C. E.; and O'Brien, R. L.: Supersonic Turbulent Boundary Layer Growth Over Cooled Walls in Adverse Pressure Gradients. ASD-TDR-62-87, U.S. Air Force, Oct. 1962.

5. Bogdonoff, S. M.; Kepler, C. E.; Sanlorenzo, E.: A Study of Shock Wave Turbulent Boundary Layer Interaction at M = 3. Rep. No. 222 (Contract No. N6-onr-270, Task Order No. 6, Project No. NR-061-049), Dept. Aero. Eng. Princeton Univ., July 1953.

6. Cornish, Joseph Jenkins, III: A Universal Description of Turbulent Boundary Layer Profiles With or Without Transpiration. Res. Rept. No. 29 (Contract No. NONR 978(01)), Aerophys. Dept., Mississippi State Univ., June 1, 1960.

7. Pinckney, S. Z.: Boundary-Layer Changes Across an Incident Reflecting Shock. [Preprint] 63116, Am. Inst. Aeron. Astronaut., Apr. 1963.

8. Persh, Jerome; and Lee, Roland: Tabulation of Compressible Turbulent Boundary Layer Parameters. NAVORD Rept. 4282 (Aeroballistic Res. Rept. 337), U.S. Naval Ord. Lab. (White Oak, Md.), May 1, 1956.

9. Wilson, R. E.: Characteristics of Turbulent Boundary Layer Flow Over a Smooth, Thermally Insulated Flat Plate at Supersonic Speeds. DRL-301, CM-712 (Contract NOrd-9195), Univ. of Texas, June 1, 1952.

10. Kuehn, Donald M.: Experimental Investigation of the Pressure Rise Required for the Incipient Separation of Turbulent Boundary Layers in Two-Dimensional Supersonic Flow. NASA MEMO 1-21-59A, 1959.

11. Sterrett, James R.; and Emery, James C.: Extension of Boundary-Layer-Separation Criteria to a Mach Number of 6.5 by Utilizing Flat Plates With Forward-Facing Steps. NASA TN D-618, 1960.

12. Liepmann, H. W.; Roshko, A.; and Dhawan, S.: On Reflection of Shock Waves From Boundary Layers. NACA Rept. 1100, 1952. (Supersedes NACA TN 2334.)

13. Aeromechanics Sec: Aerodynamic Characteristics of Nozzles and Diffusers for Supersonic Wind Tunnels. Contract AF 33(038-10112), Defense Res. Lab., Univ. of Texas, Apr. 27, 1951.

14. Schultz-Grunow, F.: New Frictional Resistance Law for Smooth Plates. NACA TM 986, 1941.

15. Wyatt, DeMarquis D.: Analysis of Errors Introduced by Several Methods of Weighting Nonuniform Duct Flows. NACA TN 3400, 1955.

16. Dennard, John S.; and Spencer, Patricia B.: Ideal-Gas Tables for Oblique-Shock Flow Parameters in Air at Mach Numbers From 1.05 to 12.0. NASA TN D-2221, 1964.

17. Vas. I. E.; and Bogdonoff, S. M.: Interaction of a Shock Wave With a Turbulent Boundary Layer at M = 3.85. Rept. No. 294 (AFOSR TN 55-199), Dept. Aeron. Eng., Princeton Univ., April 1955.

18. Kutschenreuter, Paul H.; Zurschmeide, Robert L.; and Surber, Lewis E.: An Investigation of Shock Wave-Boundary Layer Interaction With Suction (Interim Report). ASRMDF TM 61-30, U.S. Air Force, Jan. 1962.

19. Levin, Victor; and Fabish, Thomas J.: Thermal Effects of Shockwave Turbulent Boundary Layer Interaction at Mach Numbers 3 and 5. NA 62 H-795 (Contract NOw 61-0679-c), North Am. Aviation, Inc., Nov. 12, 1962.

20. Chuan, Raymond L.: On the Supersonic Flow of a Viscous Fluid Over a Compression Corner. 1956 Heat Transfer Fluid Mech. Inst. (Stanford Univ.), Stanford Univ. Press, June 1956, pp. 185-203.

21. Bardsley, O.; and Mair, W. A.: The Interaction Between an Oblique Shock-Wave and a Turbulent Boundary-Layer. Phil. Mag., ser. 7, vol. 42, no. 324, Jan. 1951, pp. 29-36.

22. Strike, W. T.; and Rippey, J.: Influence of Suction on the Interaction of an Oblique Shock With a Turbulent Boundary Layer at Mach Number 3. AEDC-TN-61-129, U.S. Air Force, Oct. 1961.

23. Ames Research Staff: Equations, Tables, and Charts for Compressible Flow. NACA Rept. 1135, 1953. (Supersedes NACA TN 1428.)

24. Kepler, C. E.; Cnossen, J. W.; and Demarest, P. E.: Hypersonic Inlet Investigations Including Tests to Mach 8.7 and Theoretical Analyses to Mach 15. ASD Tech. Rept. 61-137, U.S. Air Force, June 1961.

25. Hammitt, A. G.; Vas, I. E.; and Hight, S.: An Analysis of the Effect of Shock Waves on Turbulent Boundary Layers. Rept. No. 396 (Contract AF 18(600)-498), Dept. Aeron. Eng., Princeton Univ., July 1957.

26. Naysmith, A.: Heat Transfer and Boundary Layer Measurements in a Region of Supersonic Flow Separation and Reattachment. Tech. Note No. Aero. 2558, British R.A.E., May 1958.

27. Seban, R. A.: Heat Transfer to the Turbulent Separated Flow of Air Downstream of a Step in the Surface of a Plate. Trans. ASME, Ser. C., J. Heat Transfer, vol. 86, no. 2, May 1964, pp. 259-264.

28. Wood, Charles C.; and Knip, Gerald, Jr.: An Investigation of Screens for Removing Distortions in Ducted Flows at High Subsonic Speeds. NACA RM L57G08, 1957.

29. Von Doenhoff, Albert E.; and Tetervin, Neal: Determination of General Relations for the Behavior of Turbulent Boundary Layers. NACA Rept. 772, 1943. (Supersedes NACA WR L-382.)

30. Nestler, D. E.; and Goetz, R.: Survey of Theoretical and Experimental Determinations of Skin Friction in Compressible Boundary Layers: Part II. The Turbulent Boundary on a Flat Plate. Tech. Inform. Ser. No. R58SD270 (Contract AF 04(645)-24), Missile and Ord. Systems Dept., Gen. Elec. Co., Jan. 29, 1959.

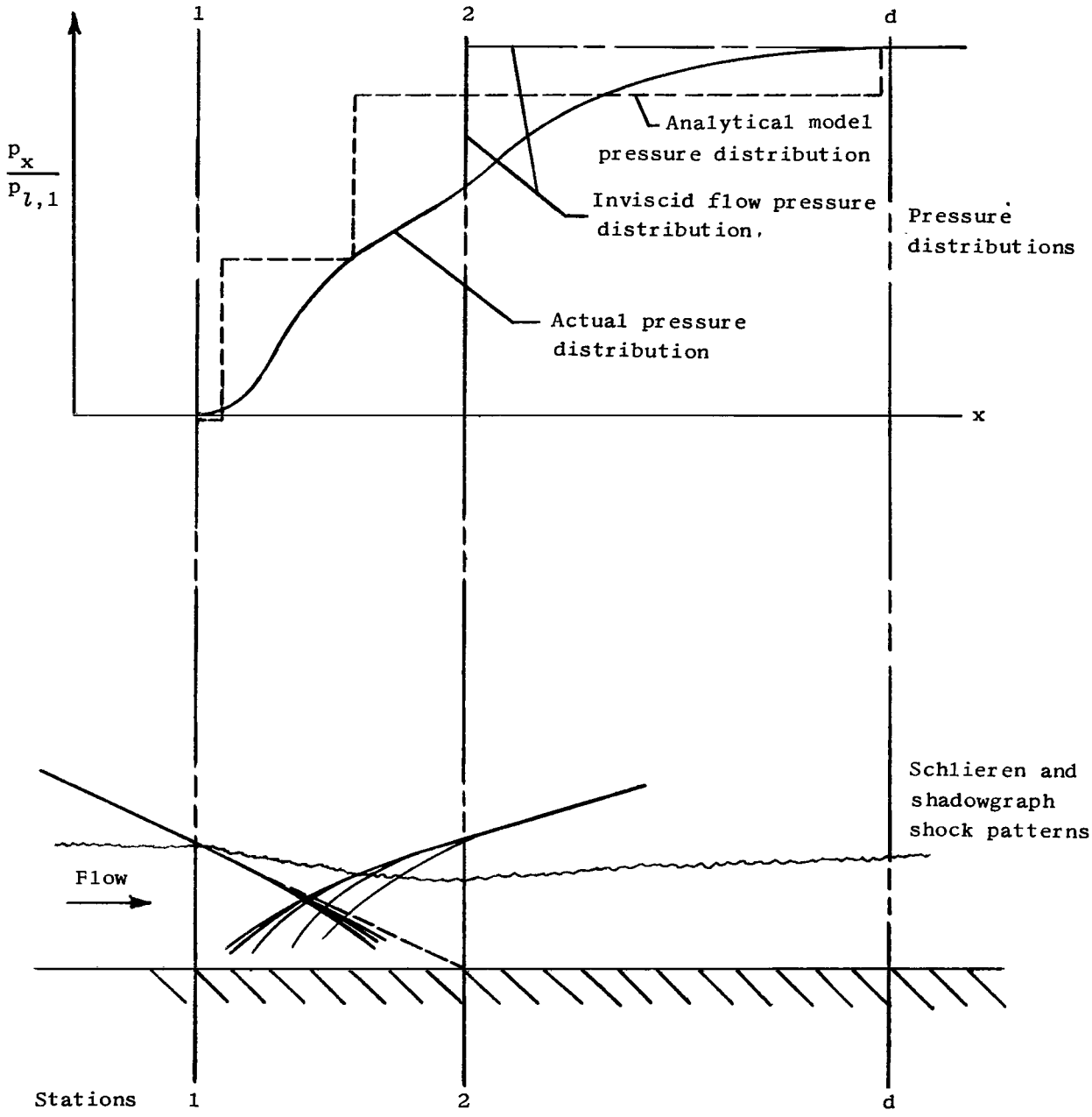

(a) Boundary-layer shock patterns and pressure distributions.

Figure 1.- Boundary-layer shock configuration.

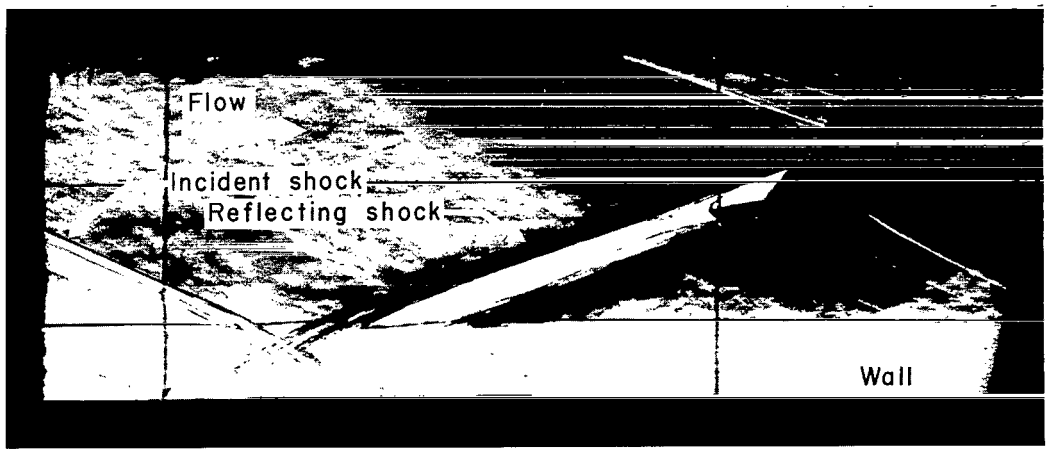

Schlieren

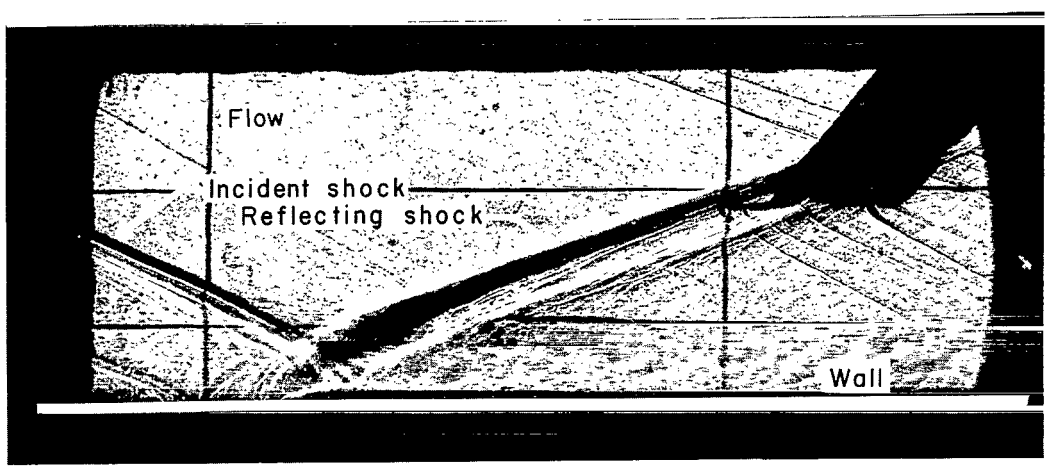

Shadowgraph

L-65-165

(b) Example shadowgraph and schlieren pictures of an incident-reflecting shock—boundary-layer interaction for $M = 3.20$ and incident shock turning angle of 8^{o}.

Figure 1.- Continued.

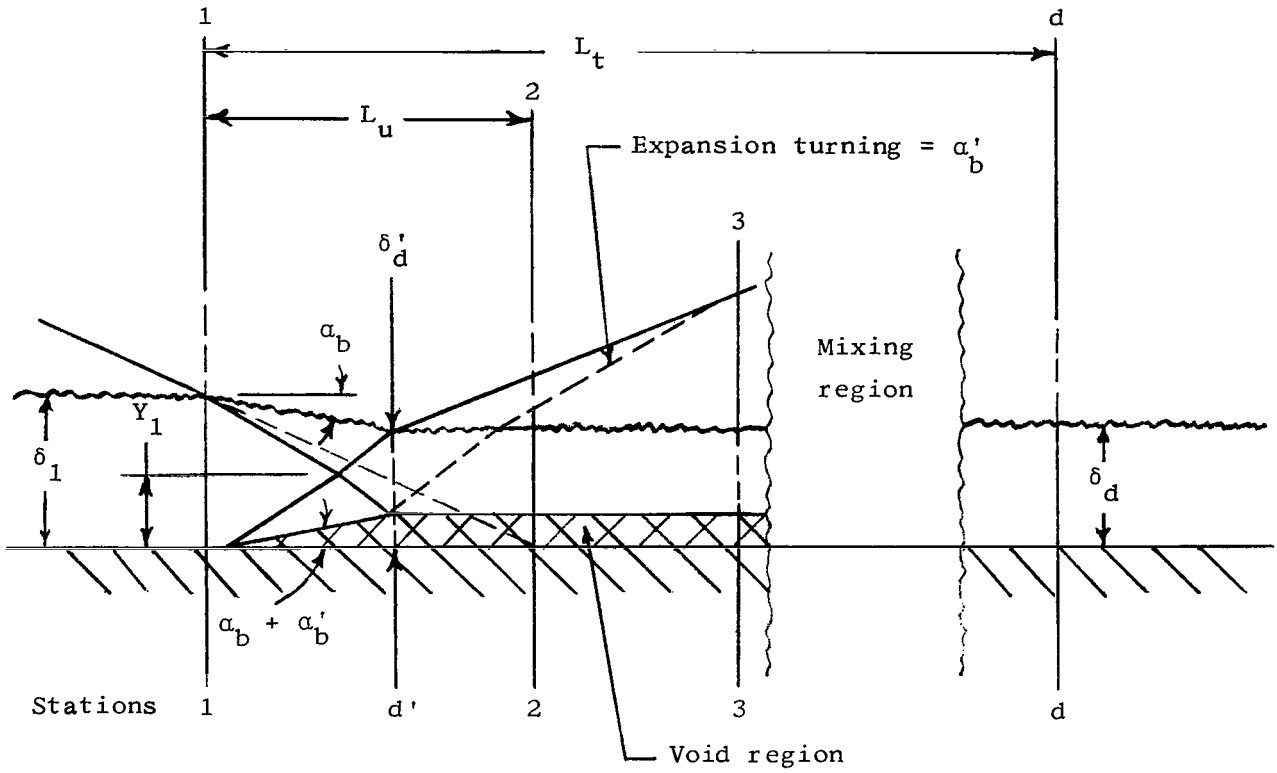

(c) Analytical boundary-layer shock model.

Figure 1.- Concluded.

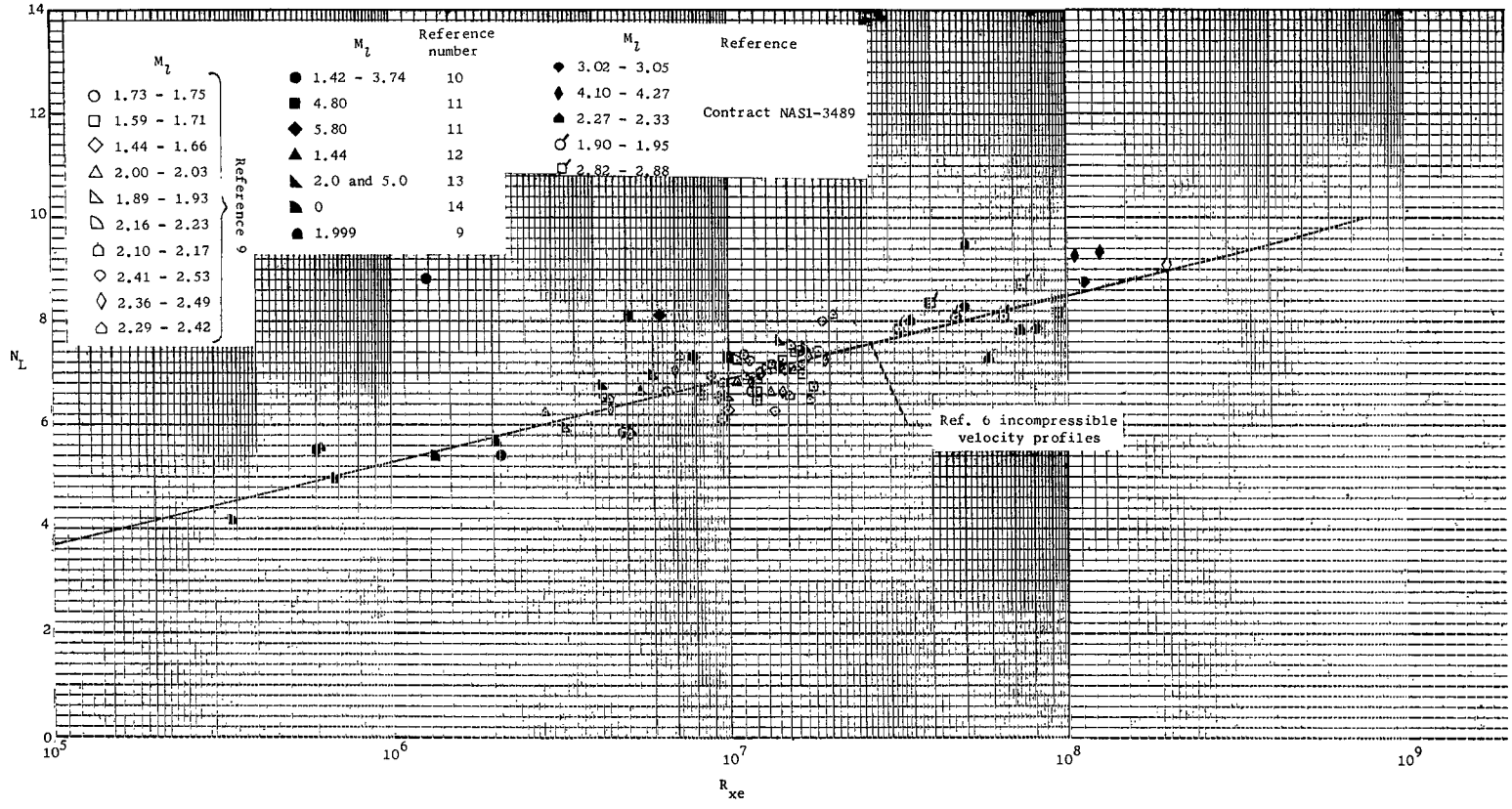

Figure 2.- Exponential boundary-layer velocity profile parameter N_L as a function of Reynolds number based on equivalent x_e.

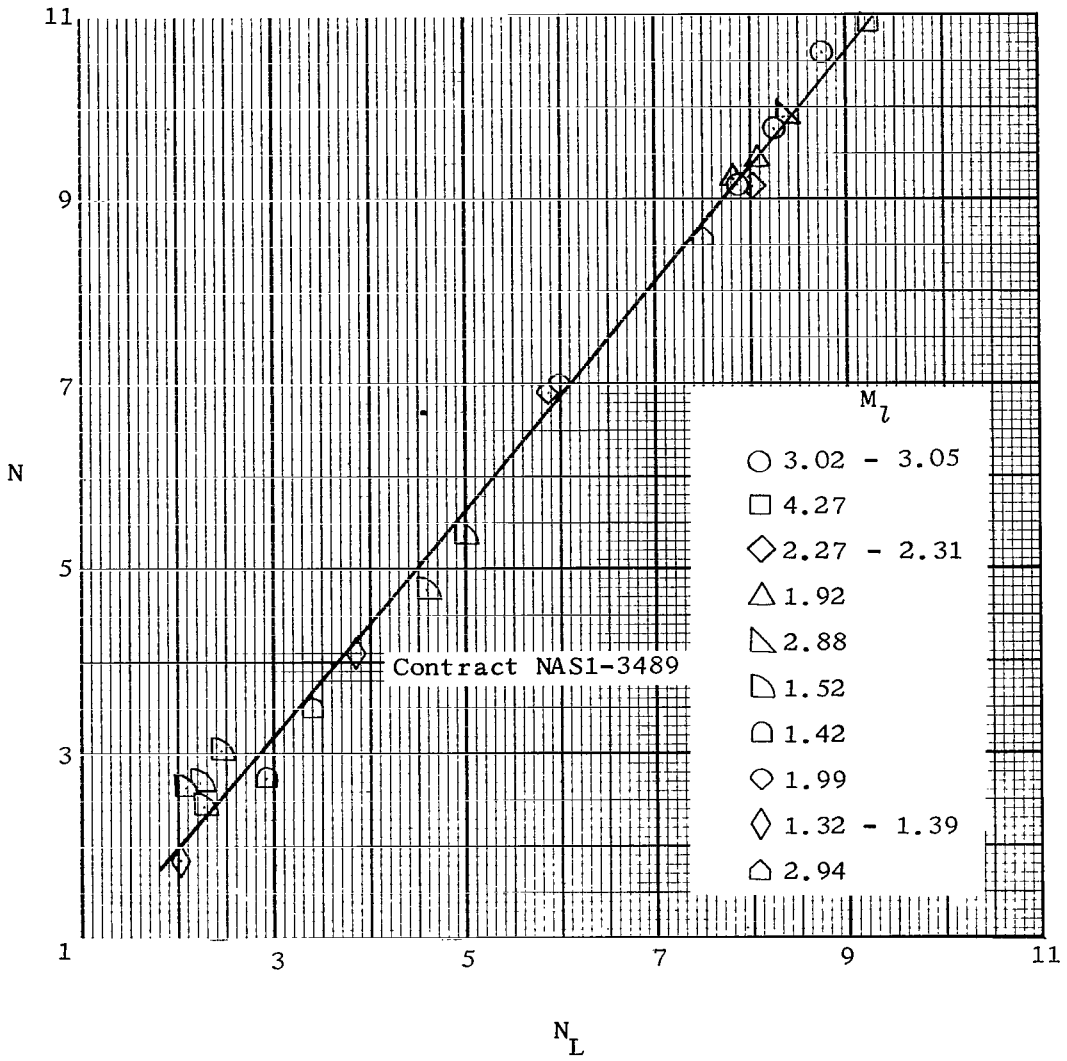

Figure 3.- Exponential velocity profile parameter N_L as a function of the profile index N.

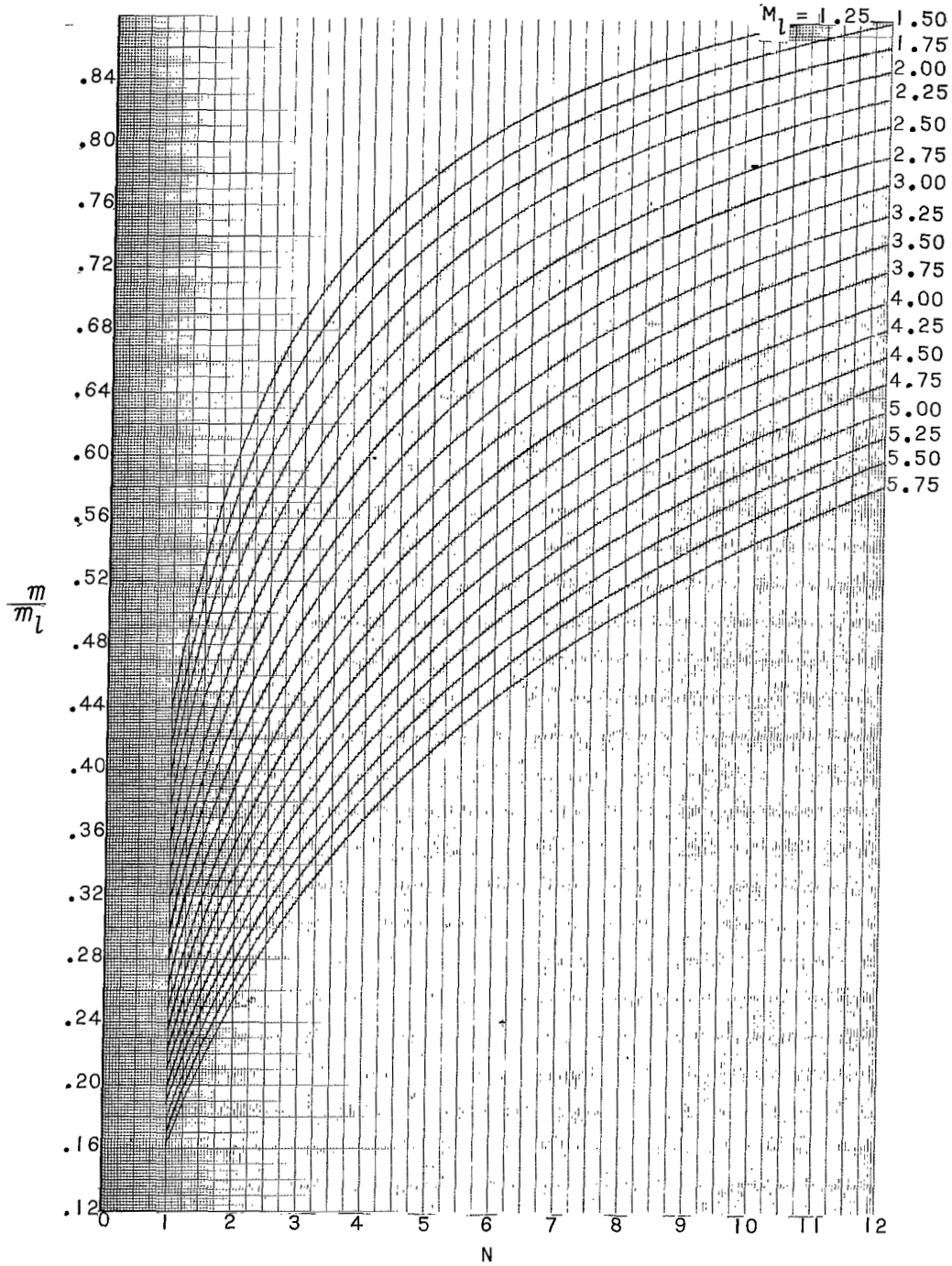

(a) M_l between 1.25 and 5.75.

Figure 4.- Plot of $\frac{m}{m_l} = \int_0^1 \frac{\rho_b V_b}{\rho_l V_l} d\left(\frac{y}{\delta}\right)$ as a function of local free-stream Mach number M_l and profile index N.

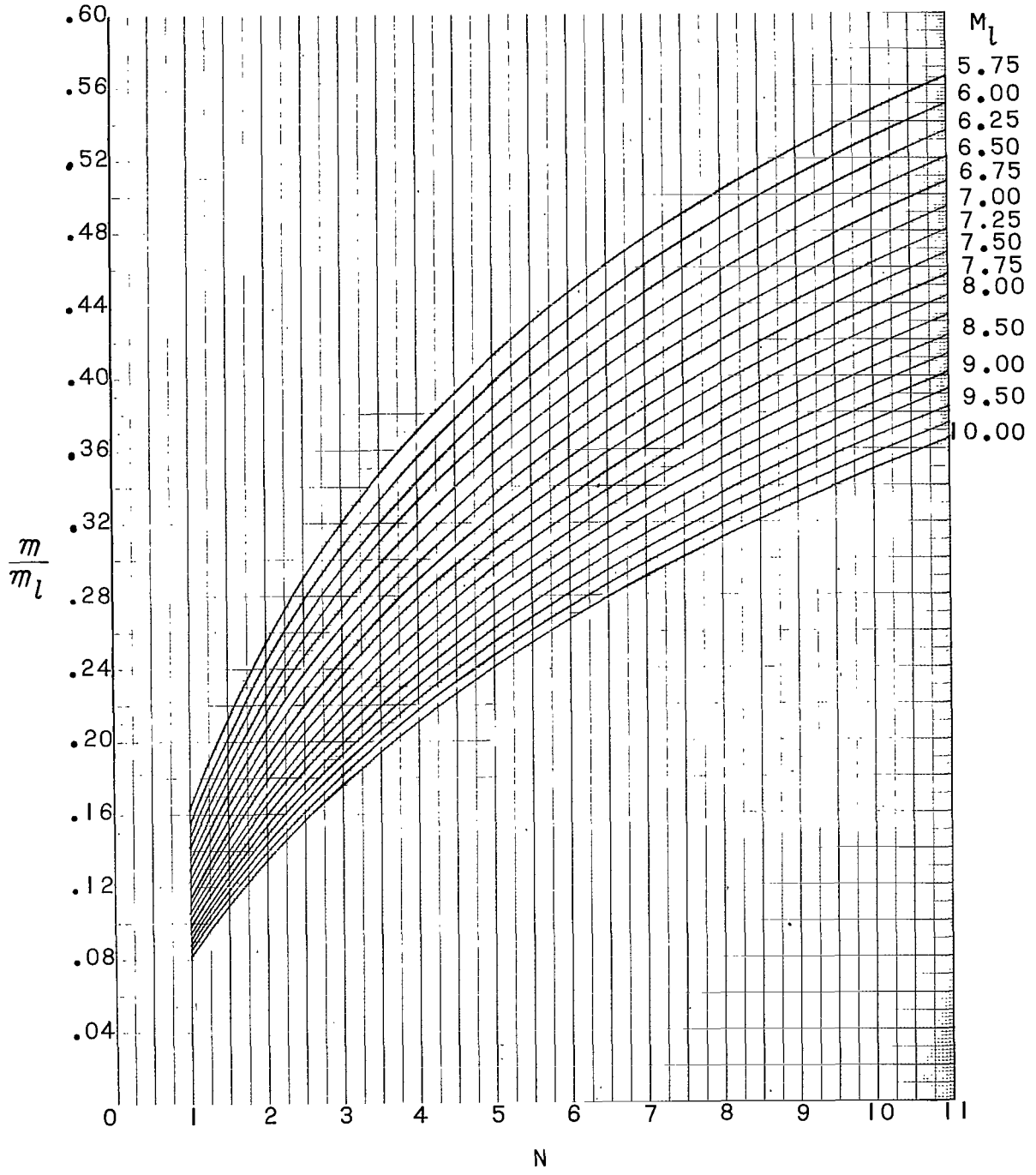

(b) M_l between 5.75 and 10.0.

Figure 4.- Concluded.

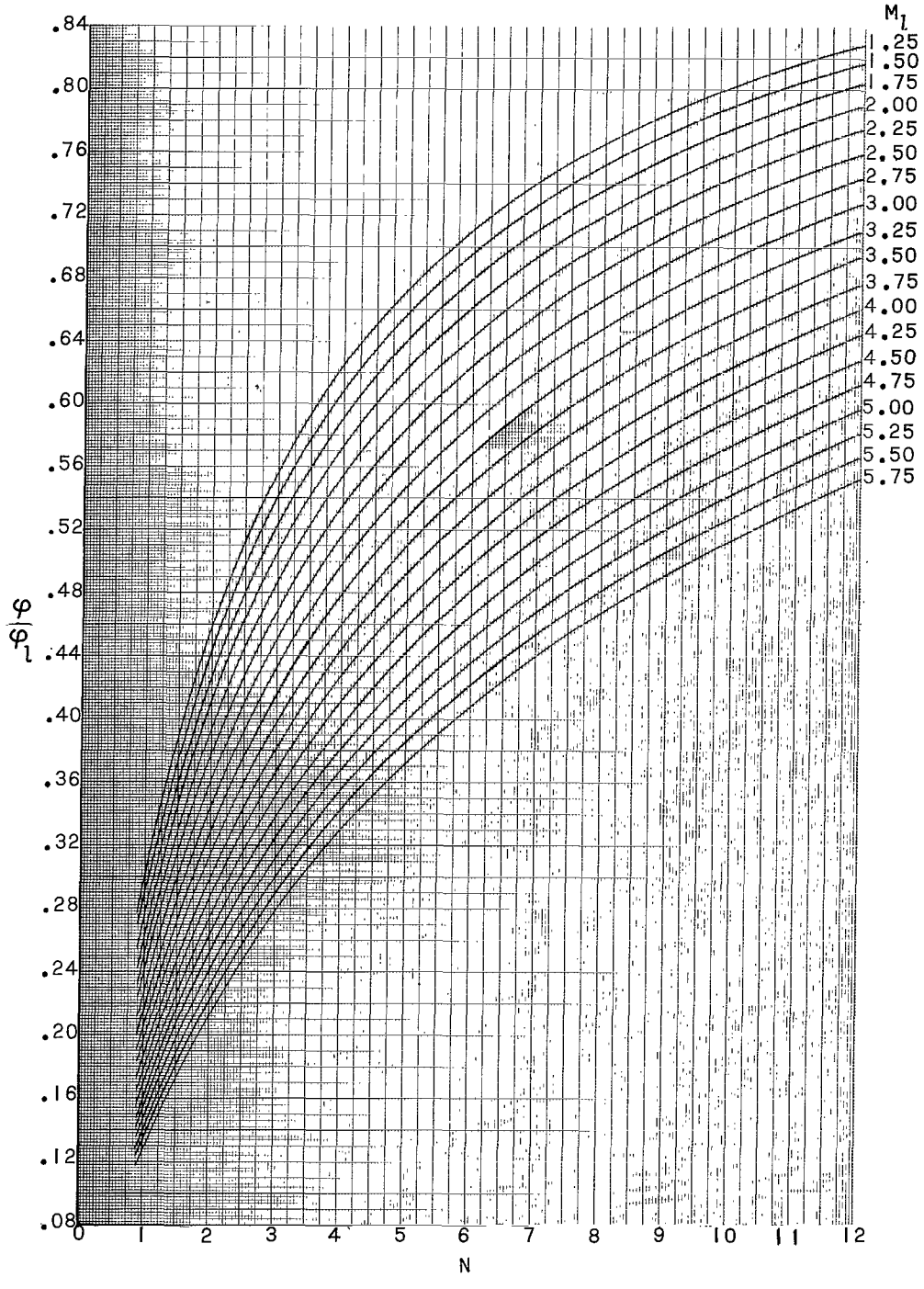

(a) M_l between 1.25 and 5.75.

Figure 5.- Plot of $\frac{\varphi}{\varphi_l} = \int_0^1 \frac{\rho_b V_b^2}{\rho_l V_l^2} d\left(\frac{y}{\delta}\right)$ as a function of local free-stream Mach number M_l and profile index N.

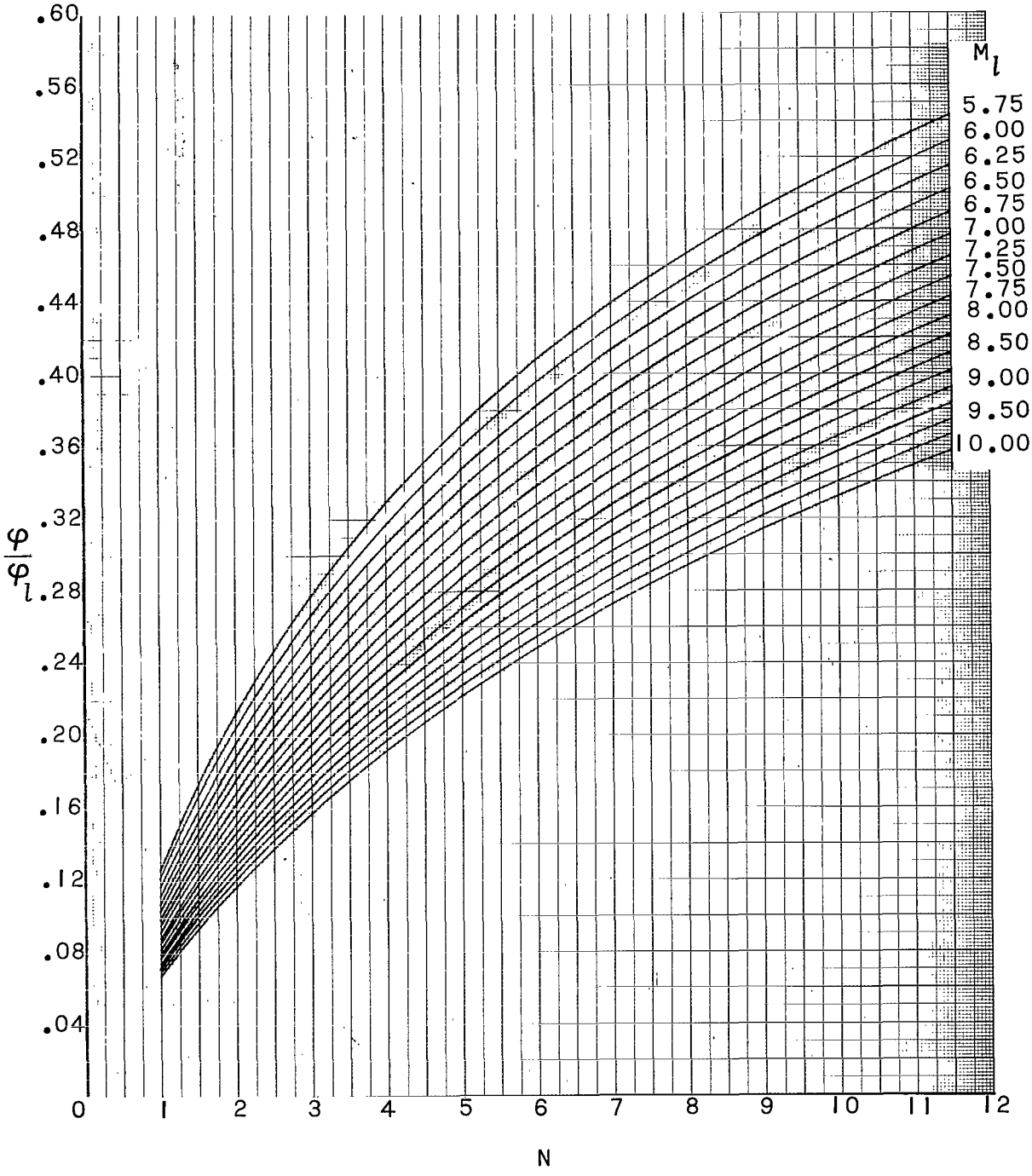

(b) M_l between 5.75 and 10.0.

Figure 5.- Concluded.

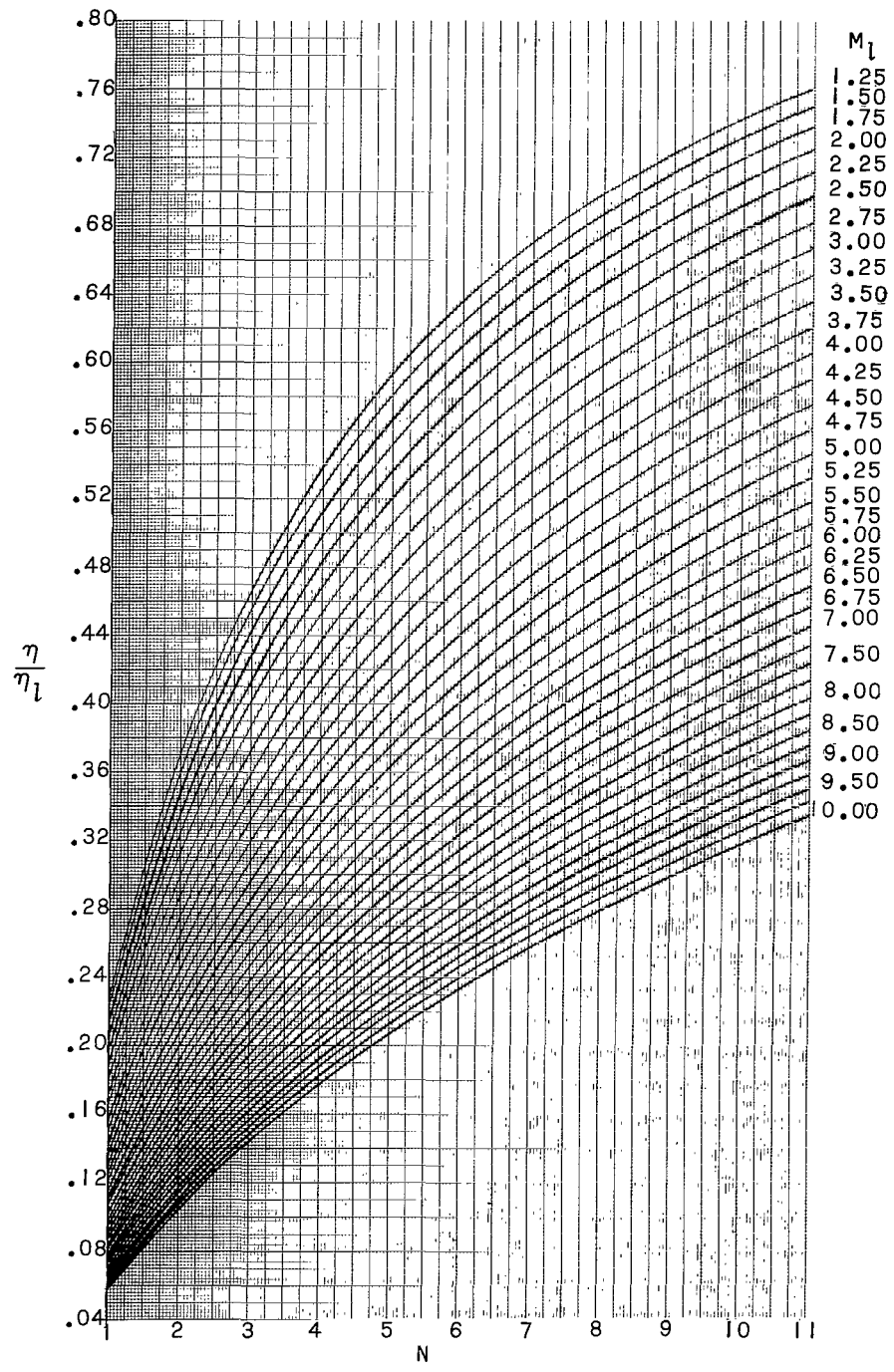

Figure 6.- Plot of $\frac{\eta}{\eta_l} = \int_0^1 \frac{\rho_b V_b^3}{\rho_l V_l^3} d\left(\frac{y}{\delta}\right)$ as a function of local free-stream Mach number M_l and profile index N.

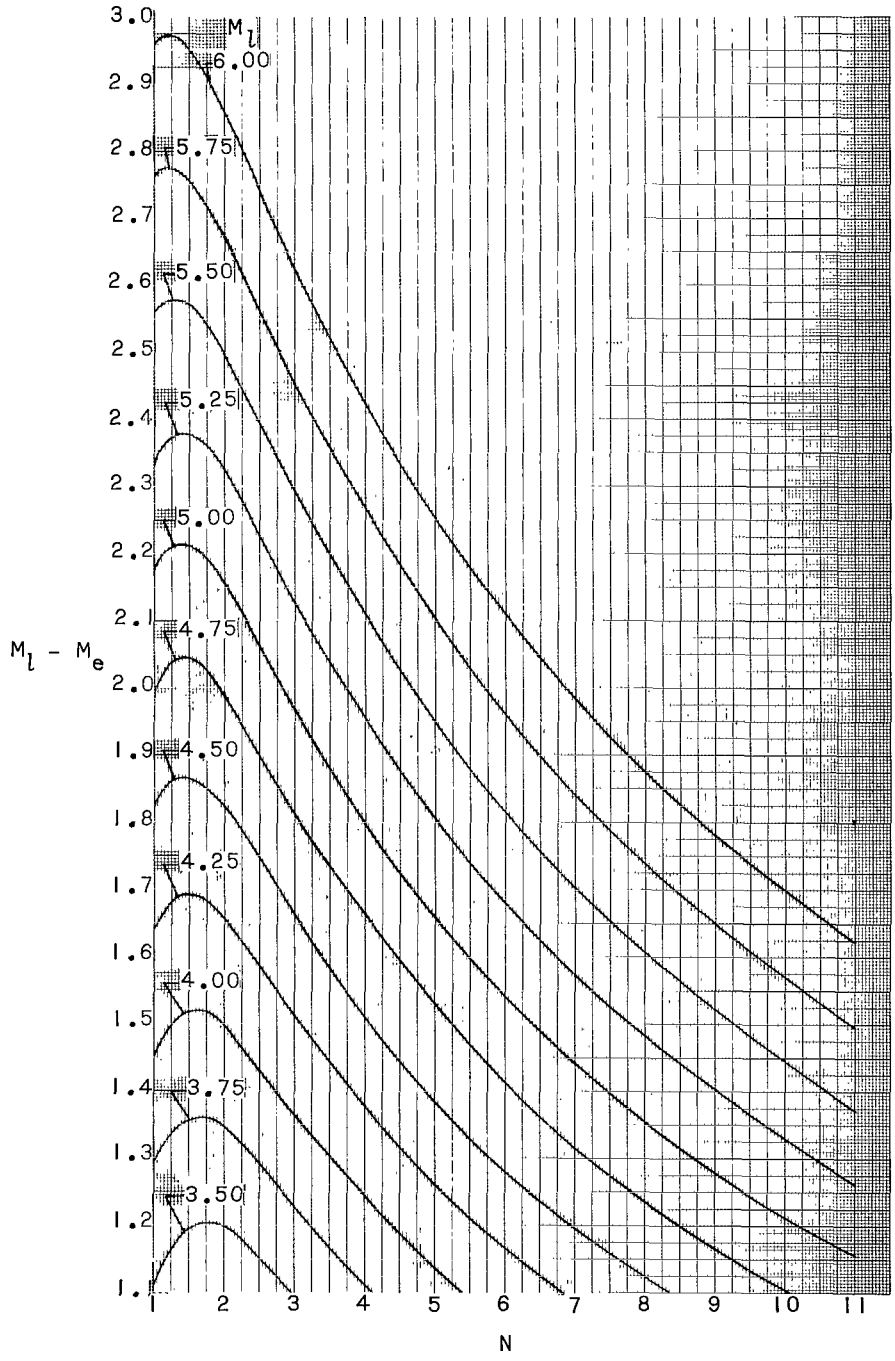

Figure 7.- The difference between free-stream and boundary-layer effective Mach numbers as functions of free-stream Mach number M_l and profile index N.

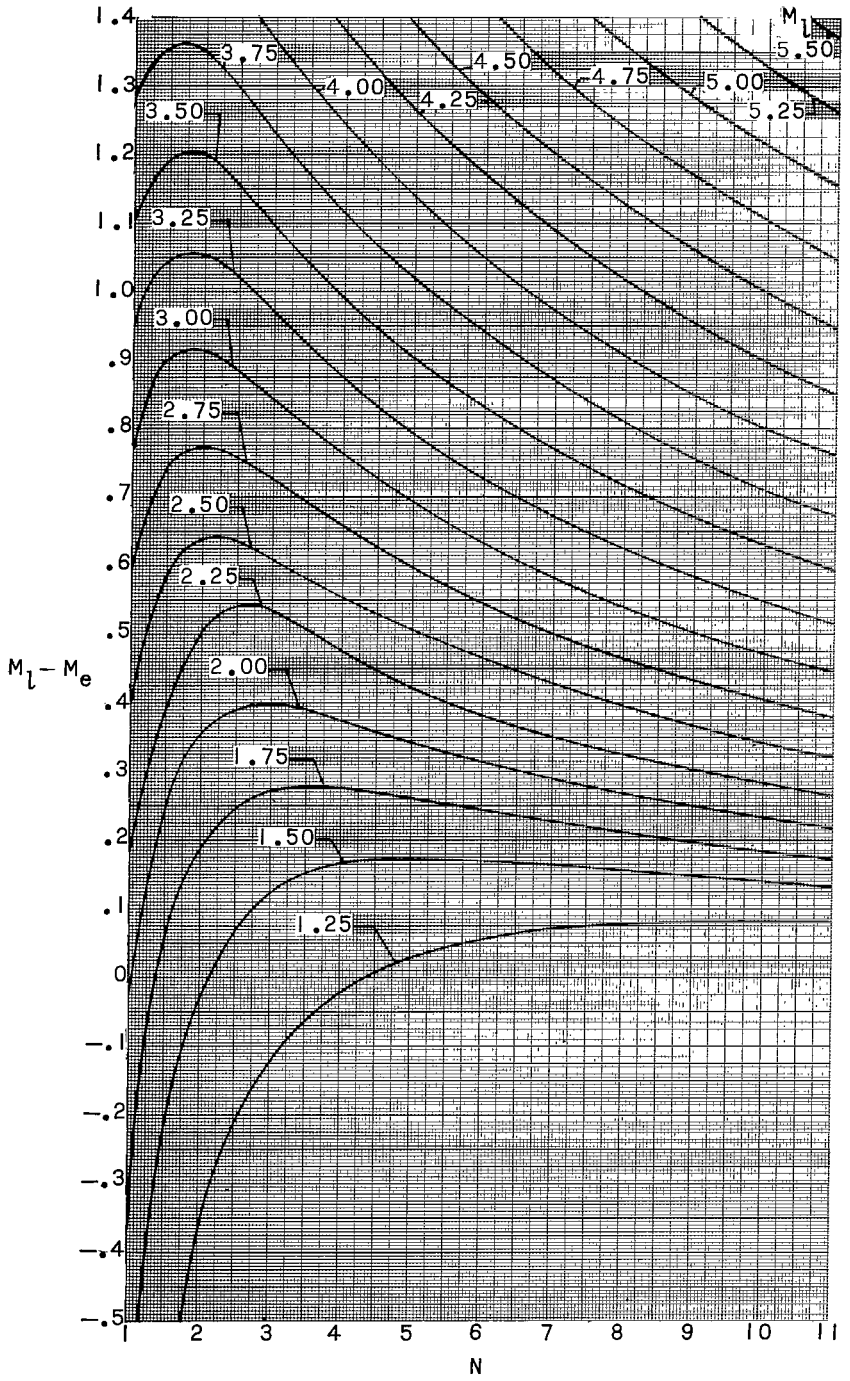

Figure 7.- Concluded.

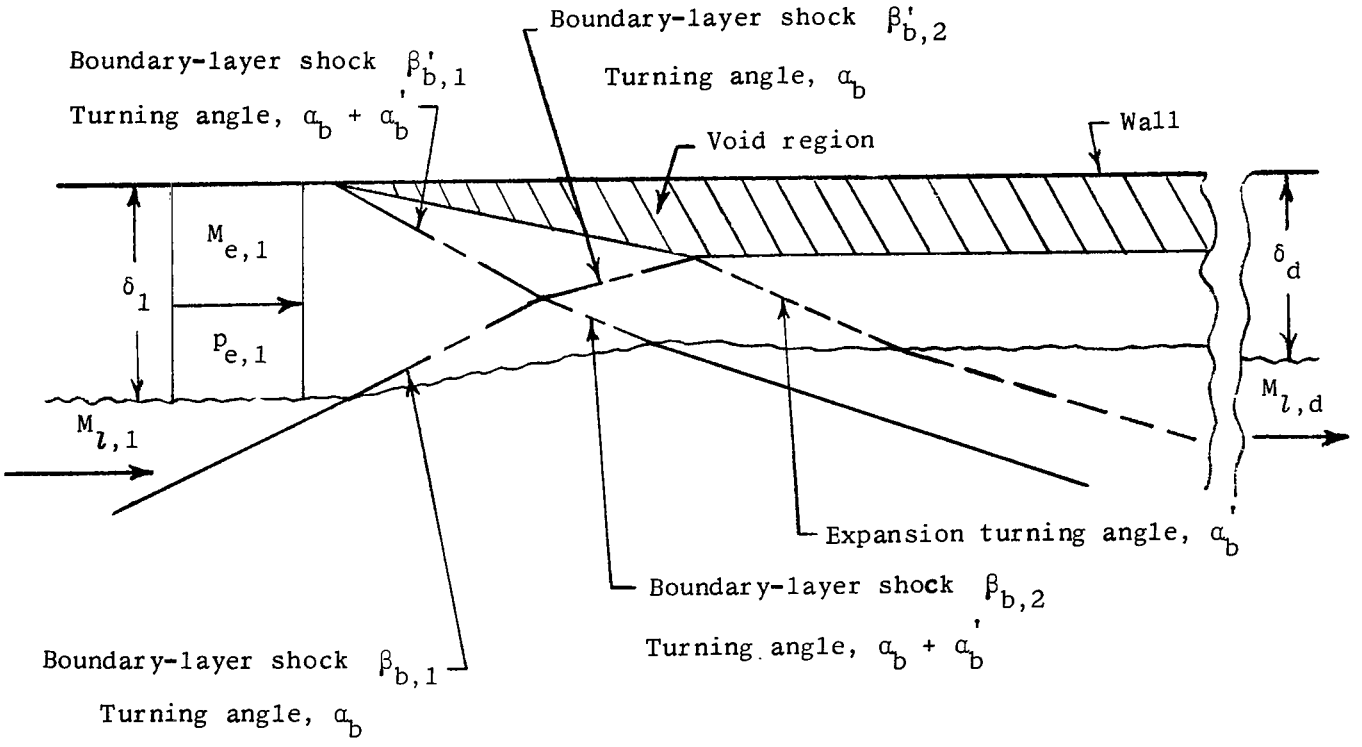

(a) Shock waves.

Figure 8.- Boundary-layer shock model for $Y_1 \leq \delta_1$.

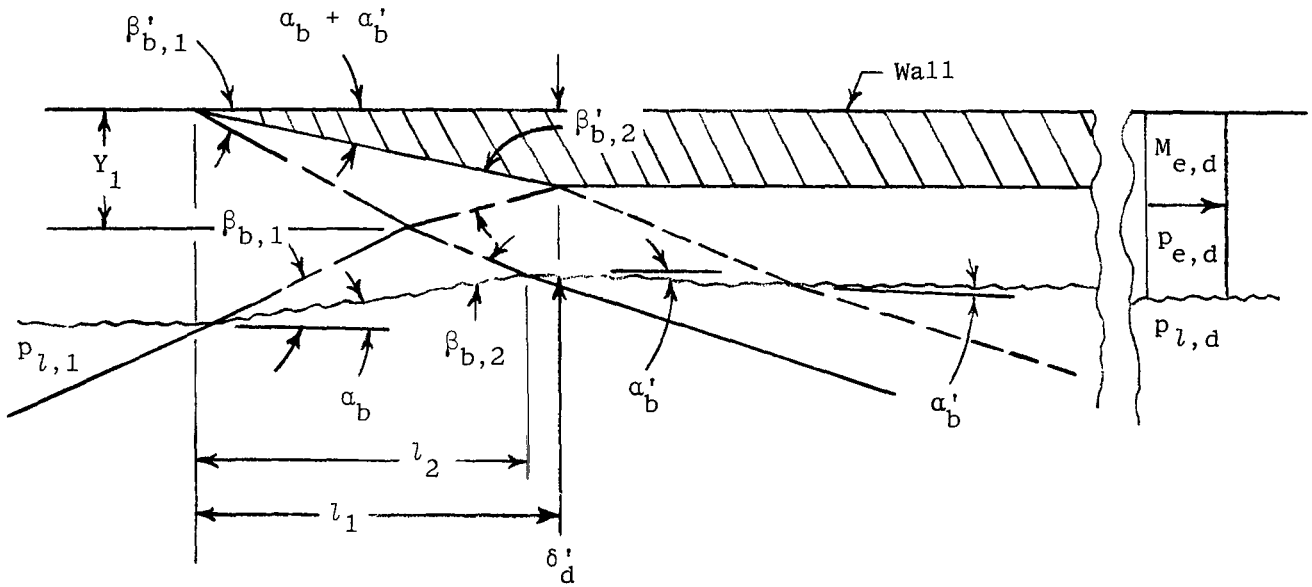

(b) Shock angles.

Figure 8.- Concluded.

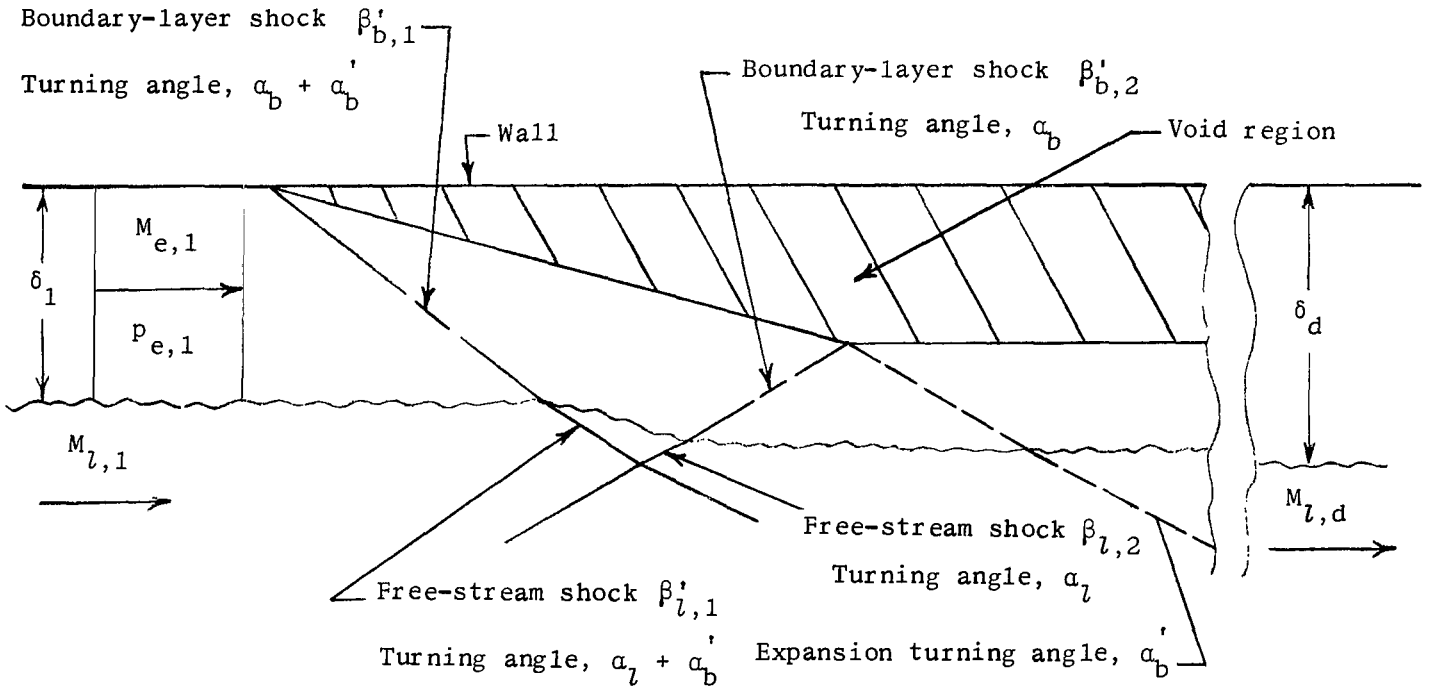

(a) Shock waves.

Figure 9.- Boundary-layer shock model for $Y_1 > \delta_1$.

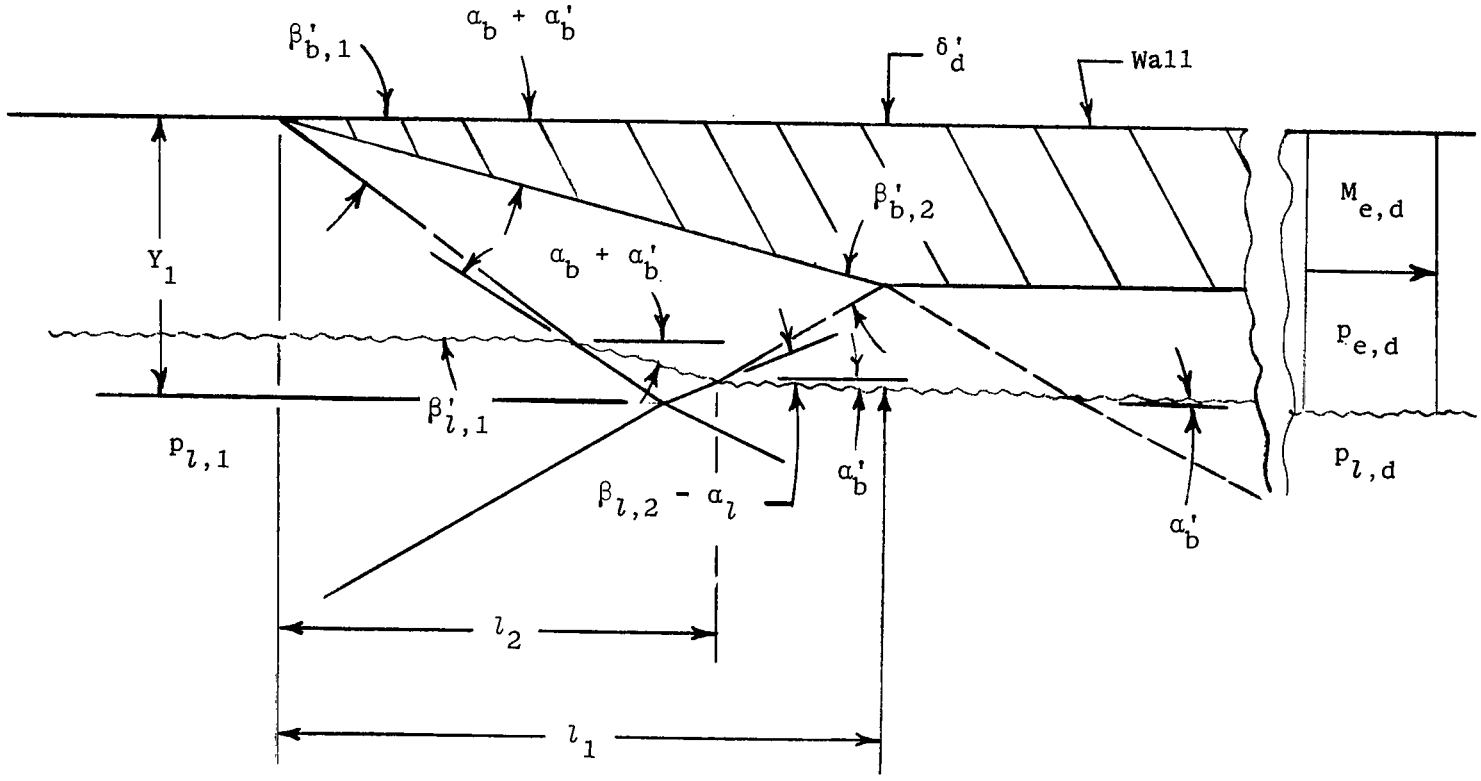

(b) Shock angles.

Figure 9.- Concluded.

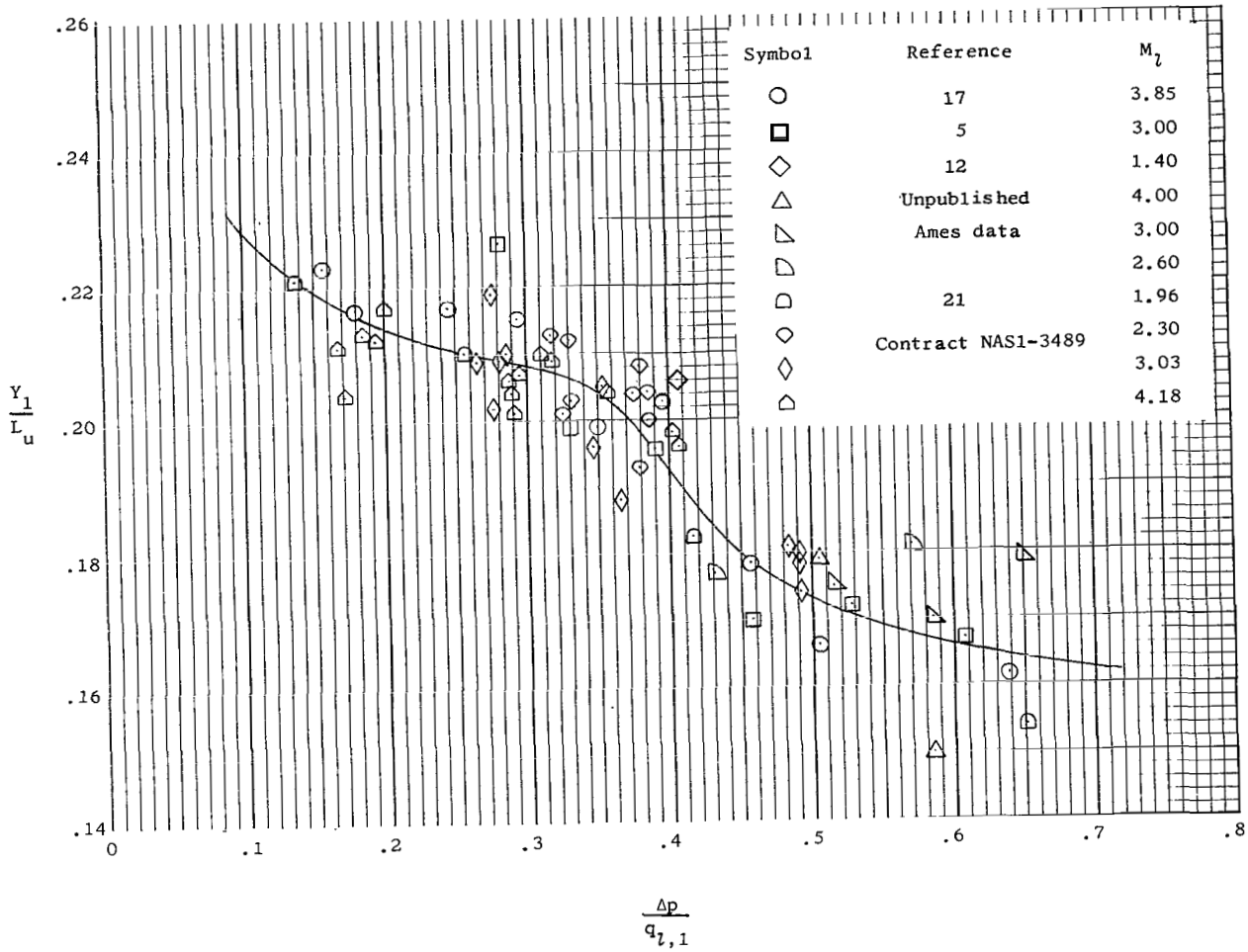

Figure 10.- Variation of $\frac{Y_1}{L_u}$ with free stream $\frac{\Delta p}{q_{l,1}}$ across a shock.

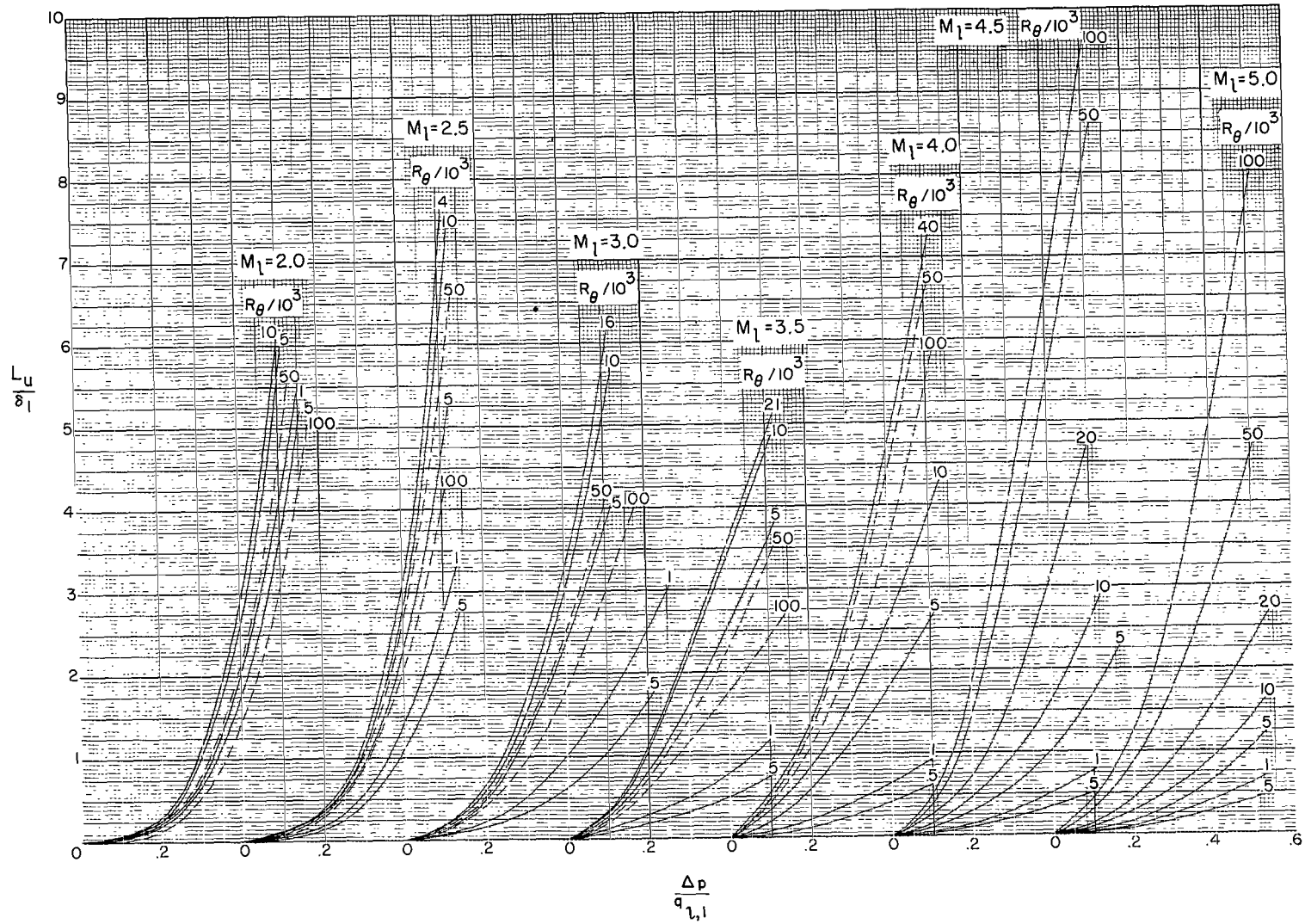

(a) Empirical curves for $\frac{L_u}{\delta_l}$.

Figure 11.- Empirical curves for $\frac{L_u}{\delta_l}$ and the correspondence of experimental data.

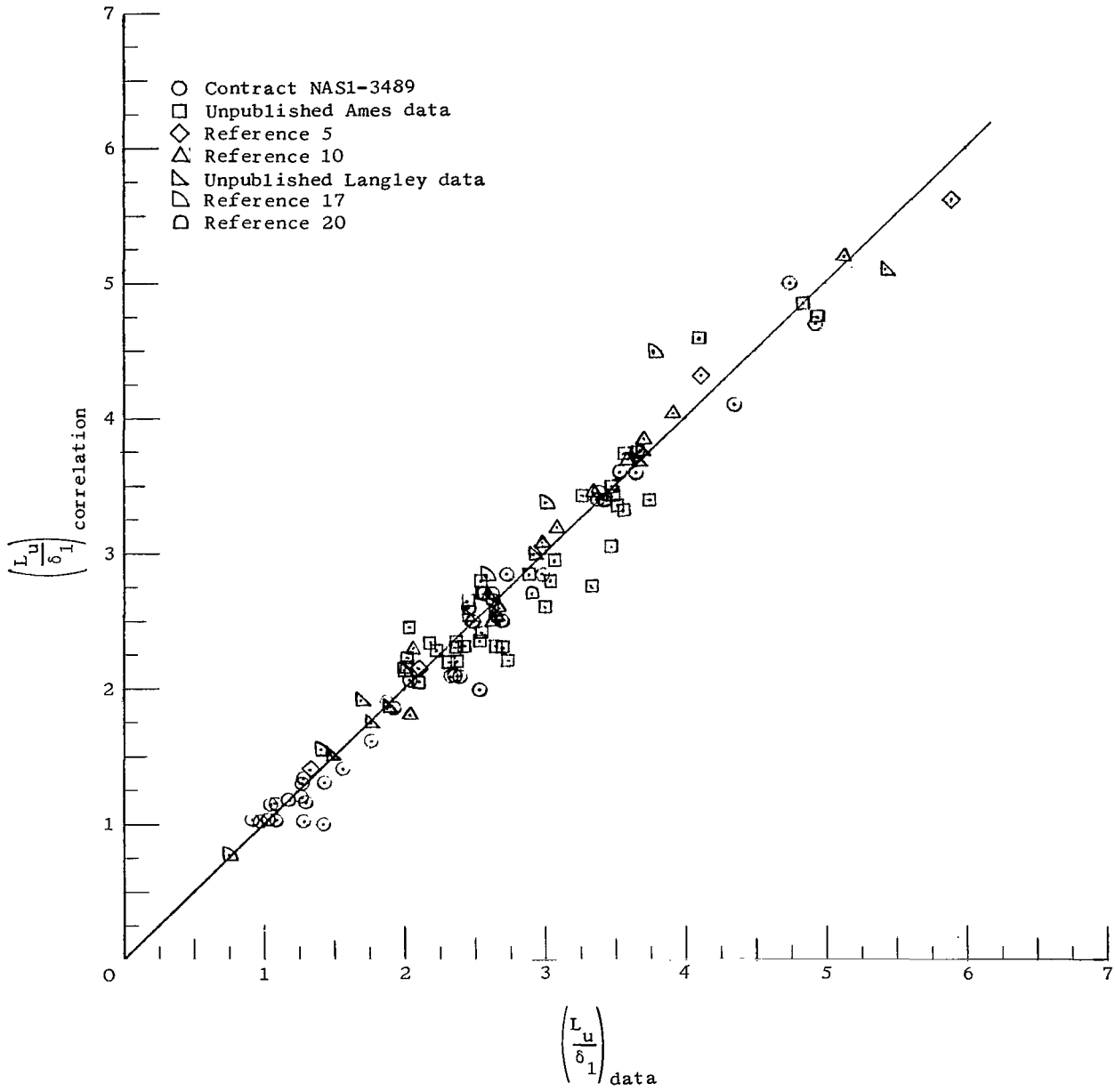

(b) Comparison of existing $\frac{L_u}{\delta_1}$ data and their corresponding empirical values.

Figure 11.- Concluded.

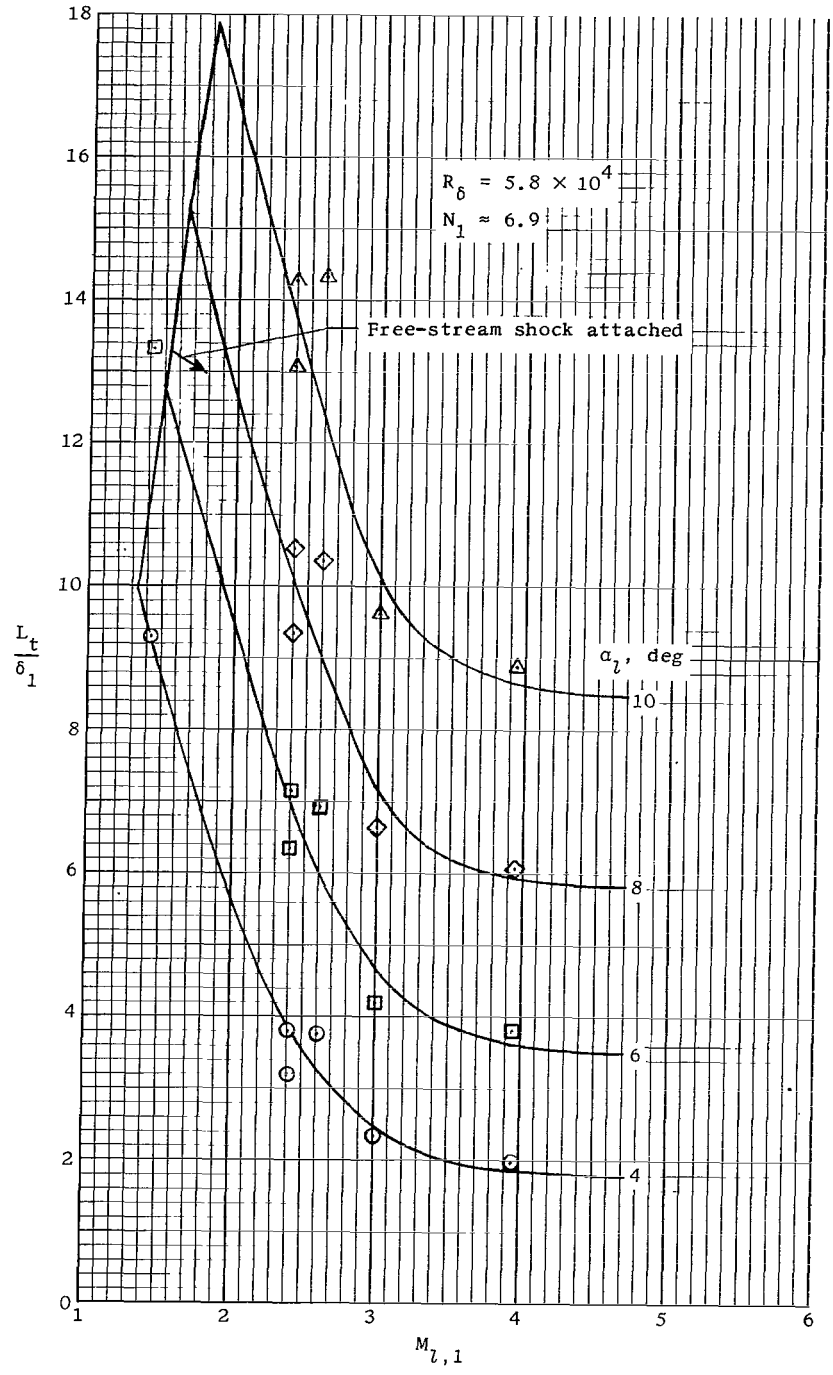

(a) Reynolds number $R_\delta = 5.8 \times 10^4$ and profile index $N_1 \approx 6.9$.

Figure 12.- Plot of nondimensional length parameter $\frac{L_t}{\delta_1}$ where L_t is the total length of the pressure gradient imposed on a plate by an incident-reflecting shock.

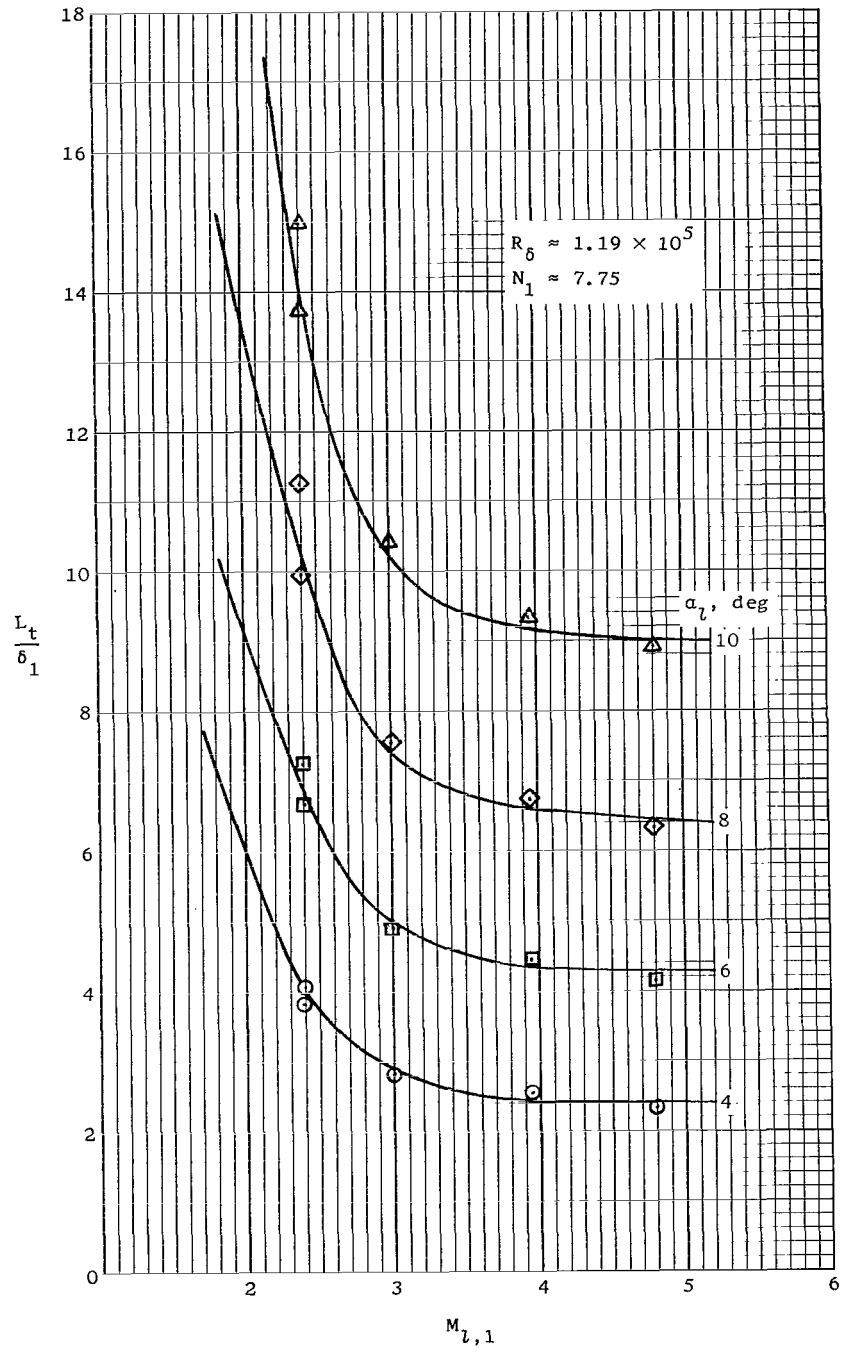

(b) Reynolds number $R_\delta \approx 1.19 \times 10^5$ and profile index $N_1 \approx 7.75$.

Figure 12.- Continued.

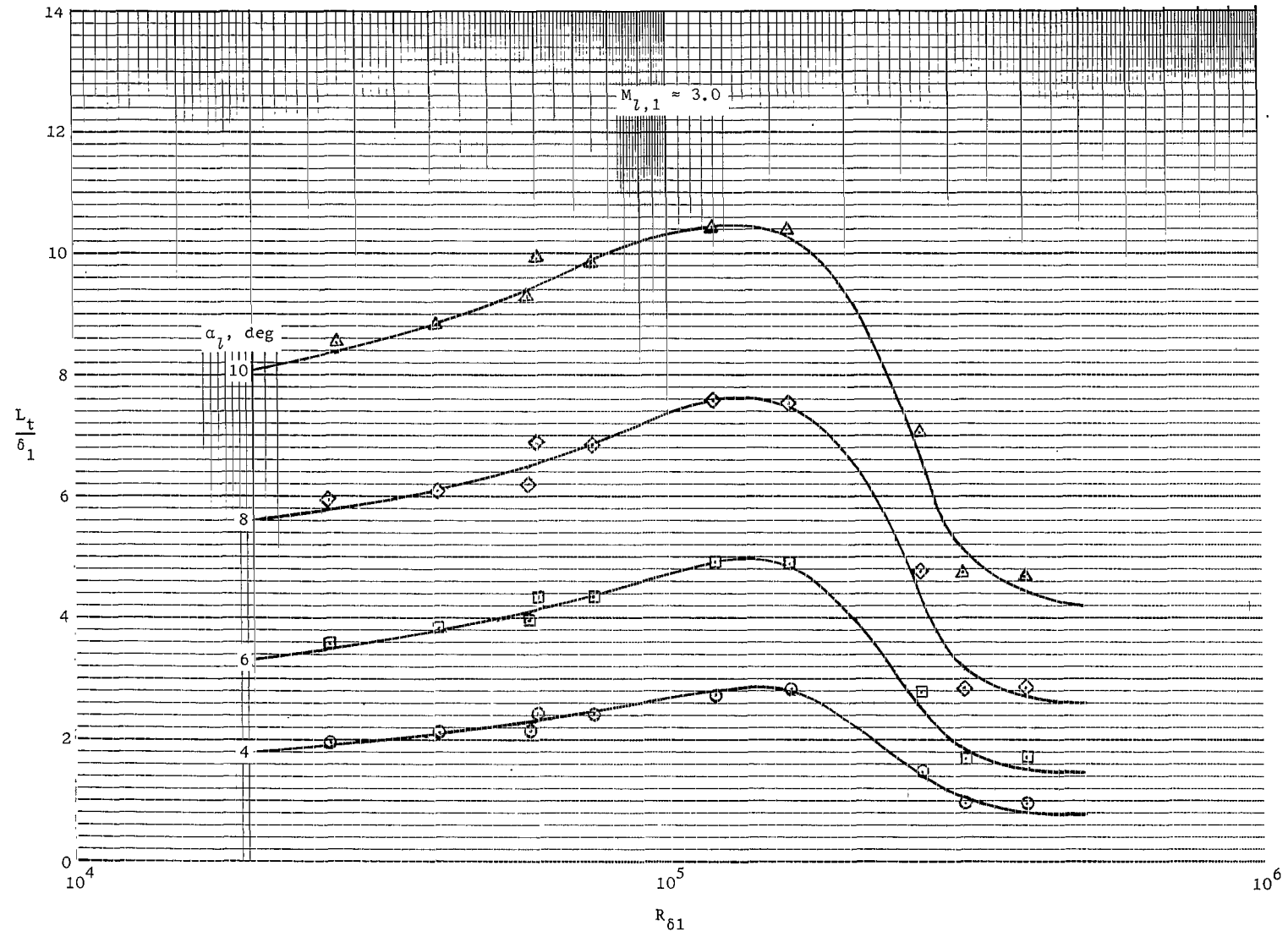

(c) $M_{l,1} \approx 3.0$.

Figure 12.- Concluded.

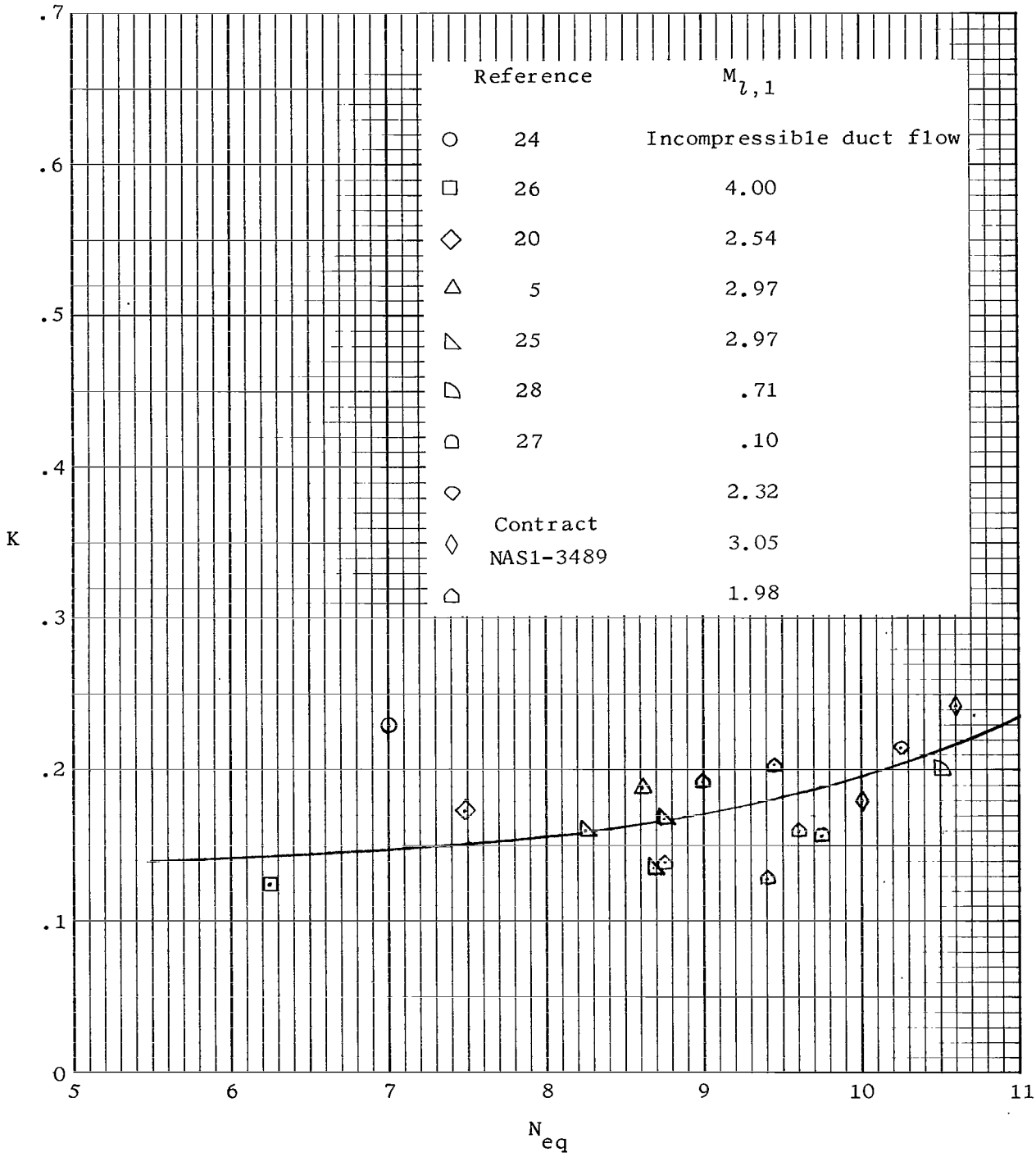

Figure 13.- Mixing constant K as a function of equilibrium profile index N_{eq}.

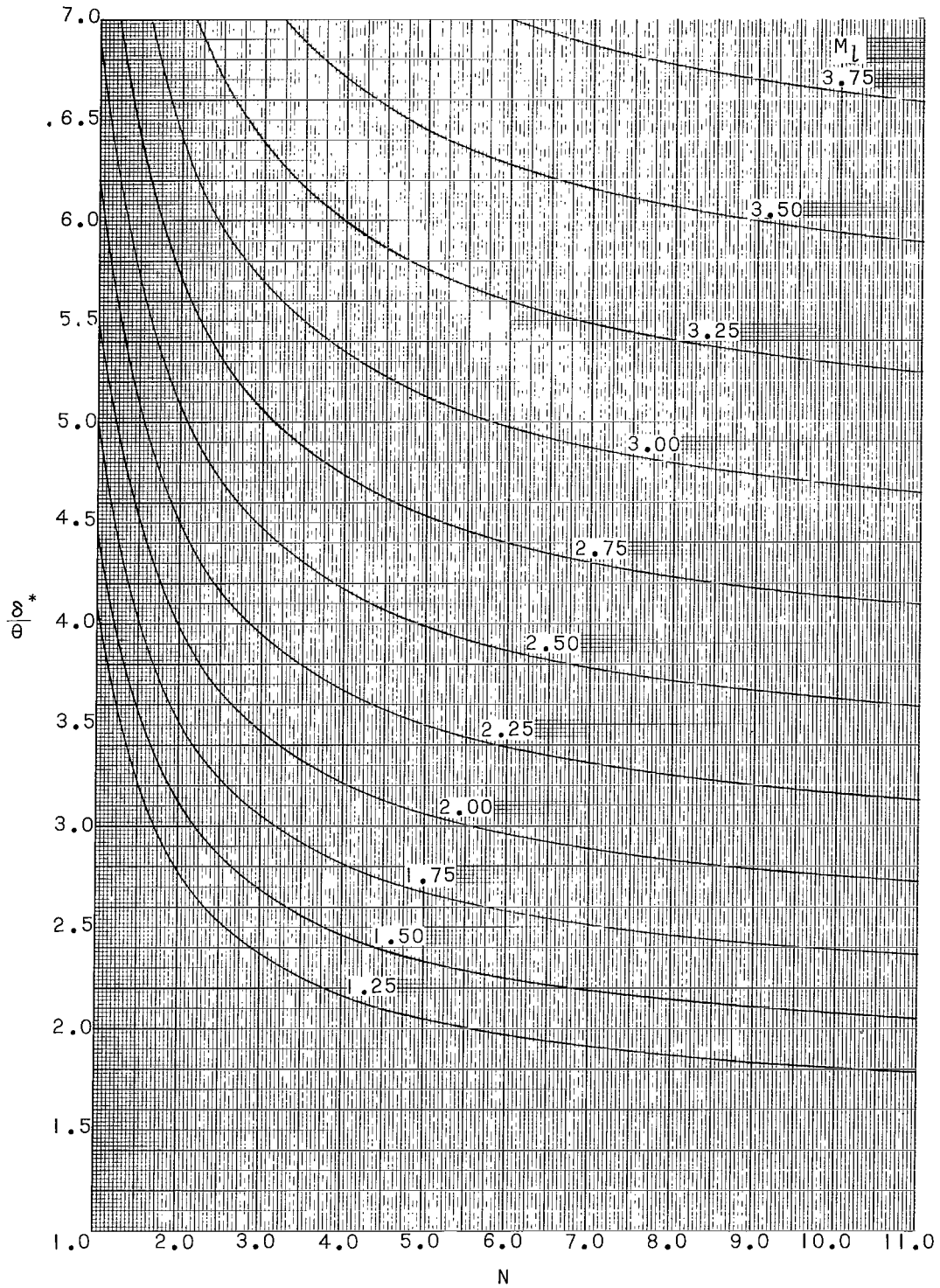

Figure 14.- Compressible flow shape parameter $\frac{\delta^*}{\theta}$ as a function of profile index N and free-stream Mach number M_l.

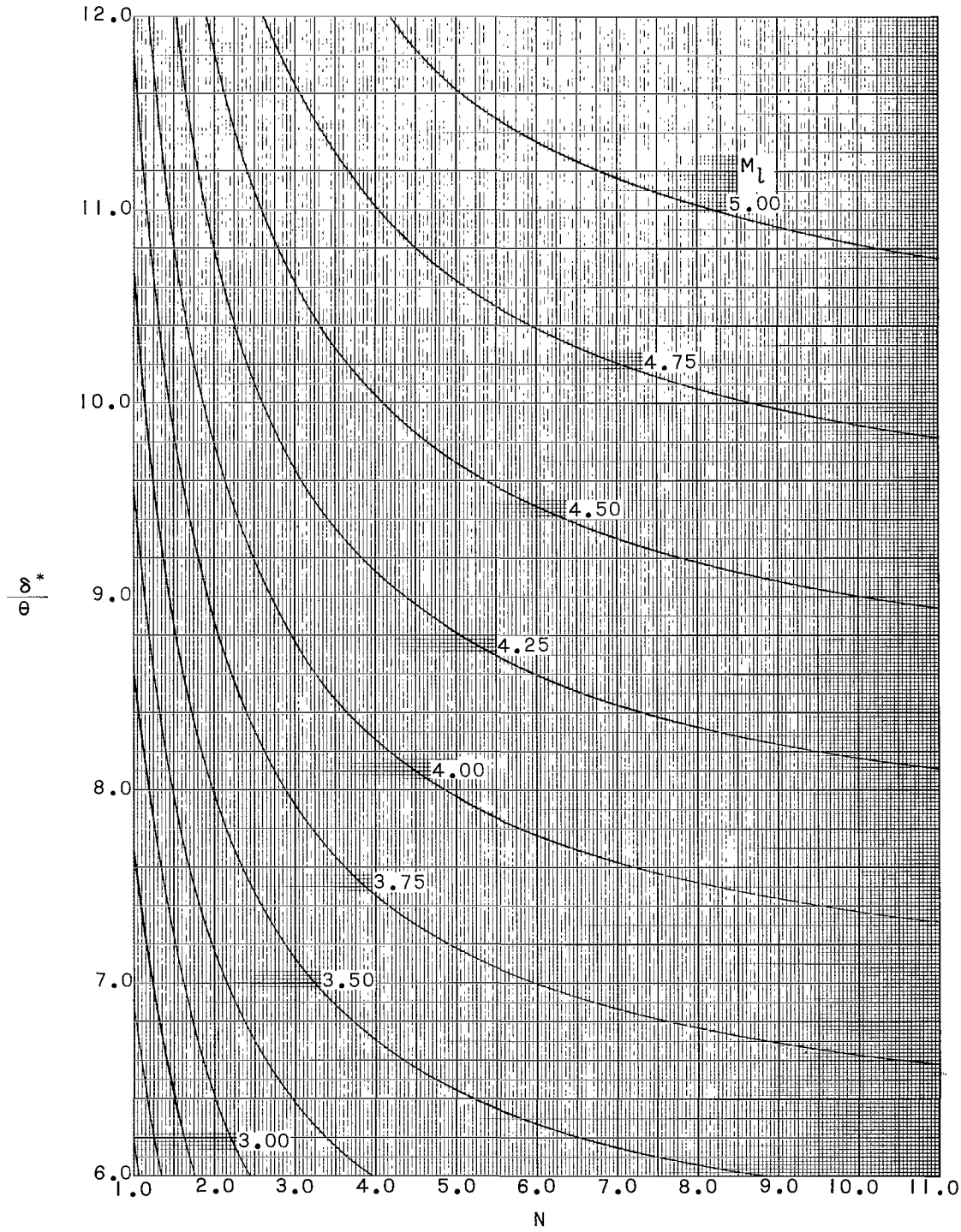

Figure 14.- Concluded.

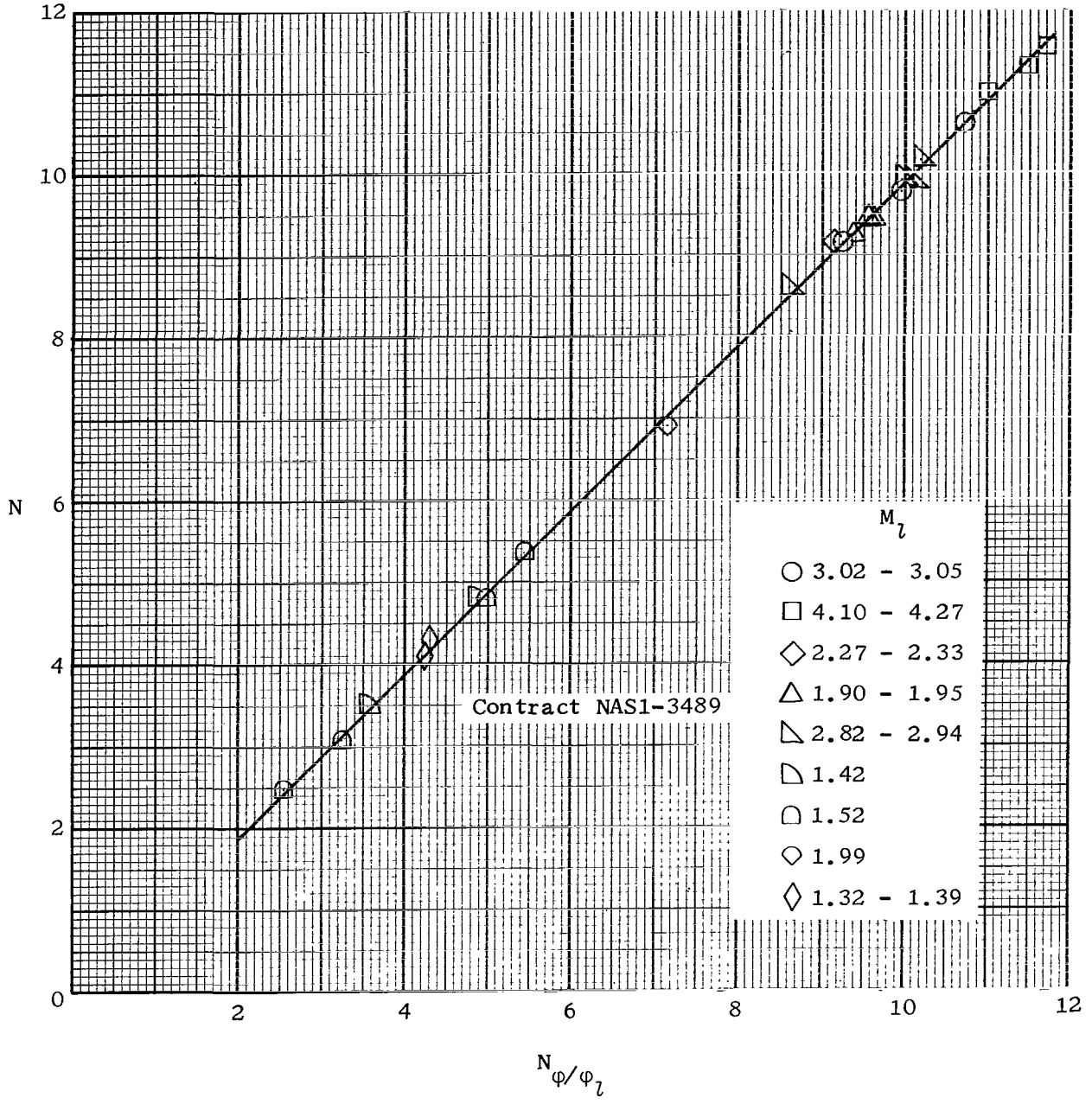

Figure 15.- Variation of profile index N with profile index N_{φ/φ_l}.

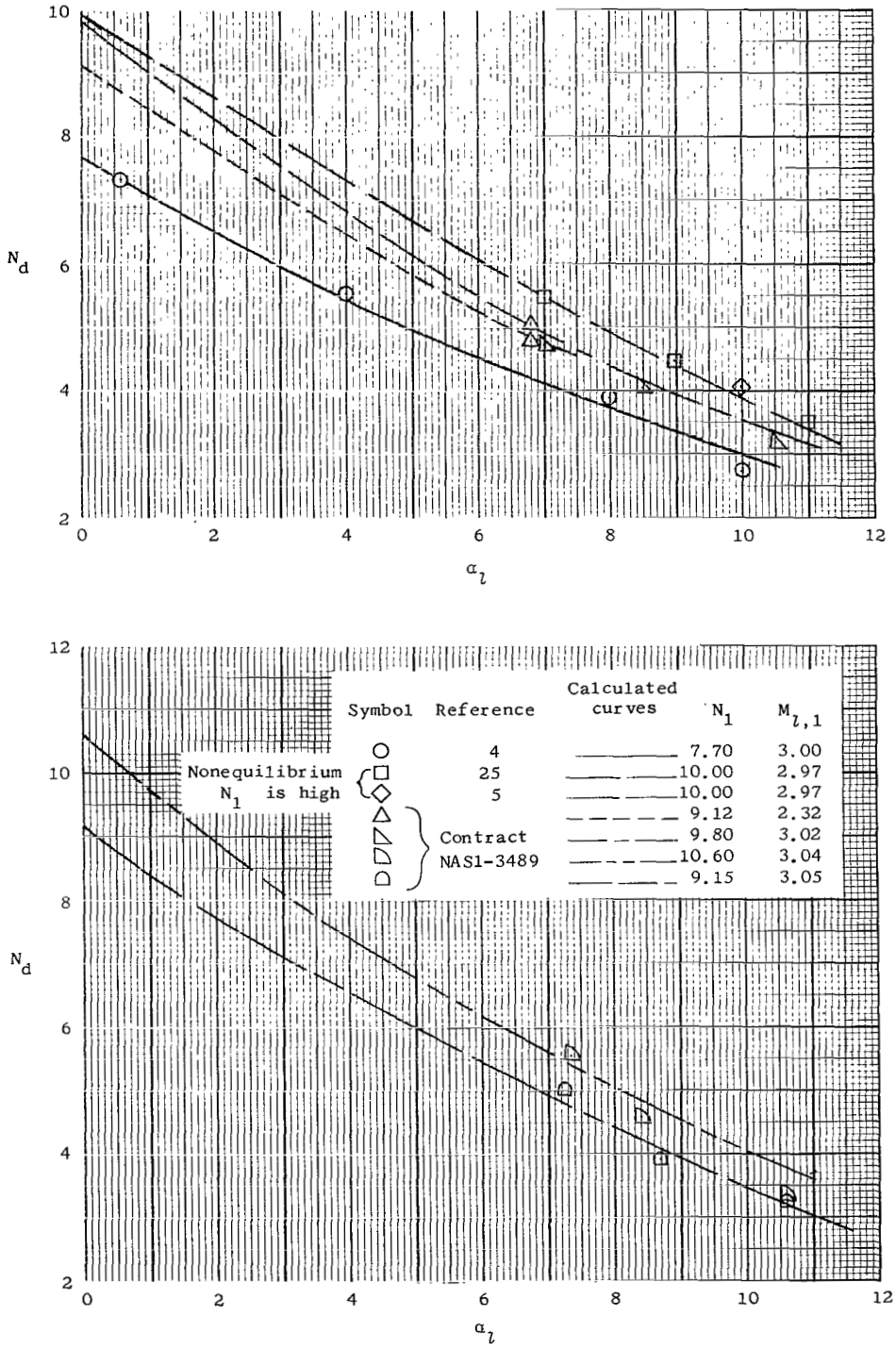

Figure 16.- Calculated profile index parameter changes as compared with data.

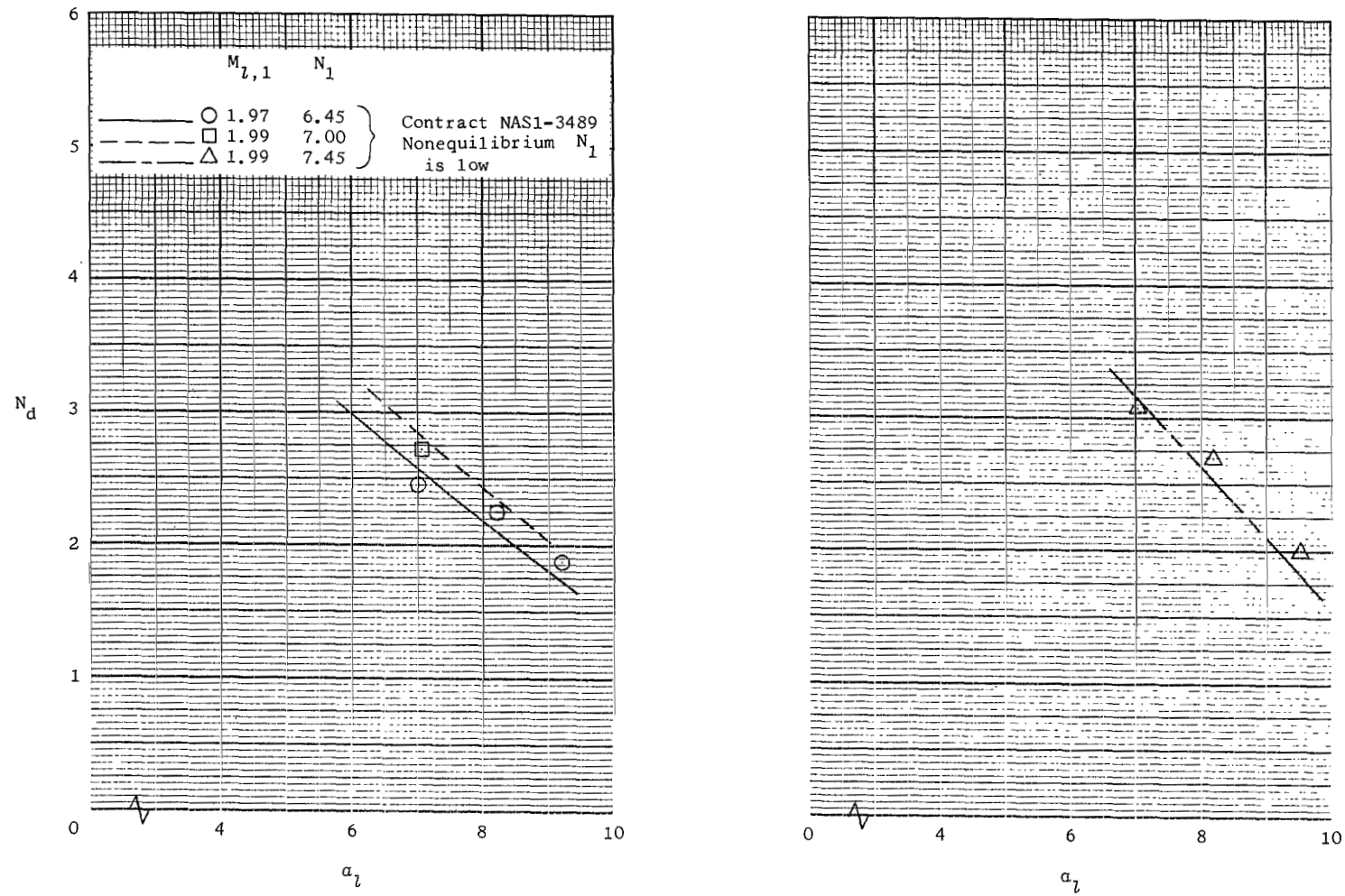

Figure 16.- Concluded.

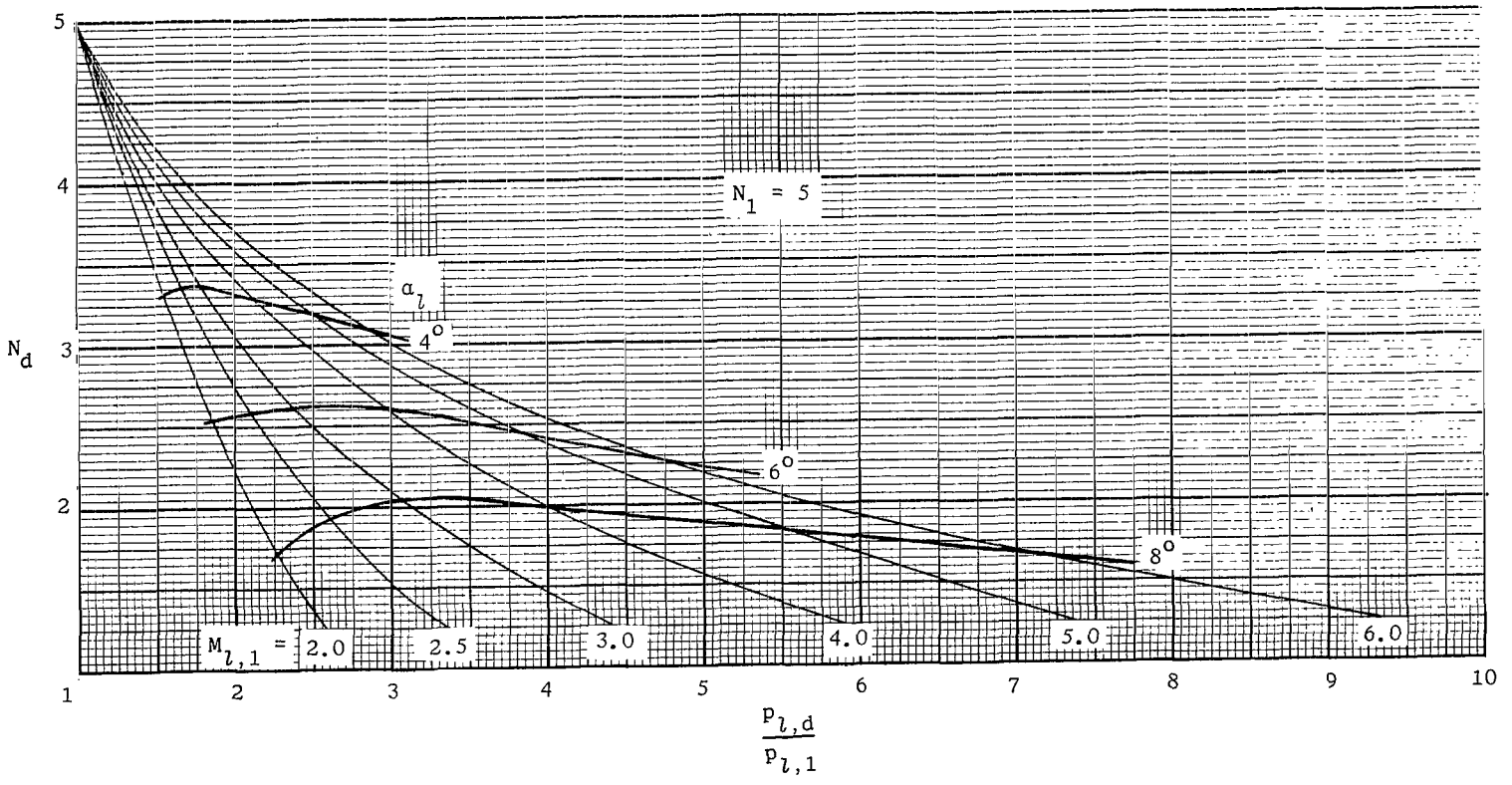

(a) $N_1 = 5$.

Figure 17.- Curves for the profile index change from station 1 to station d.

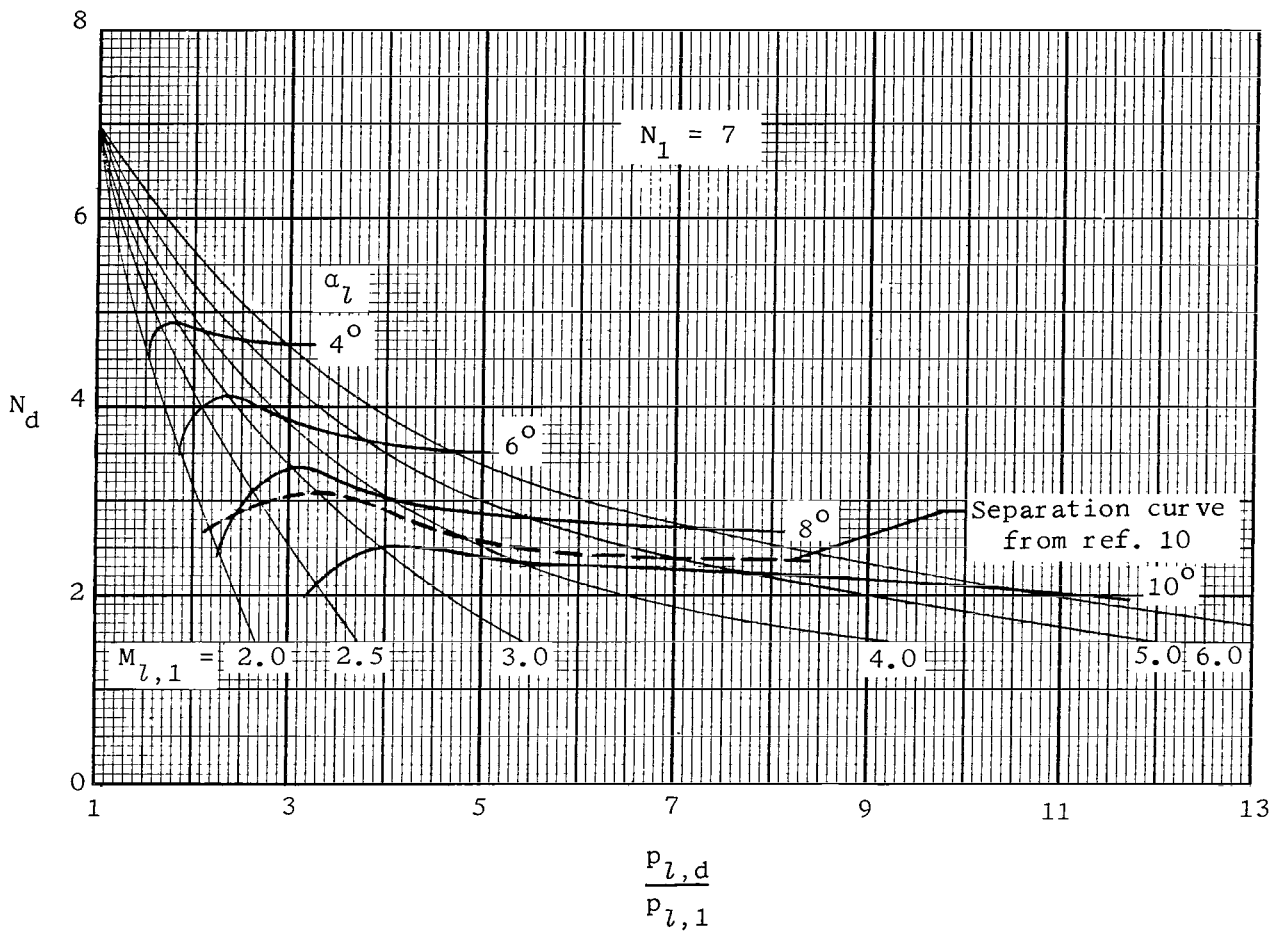

(b) $N_1 = 7$.

Figure 17.- Continued.

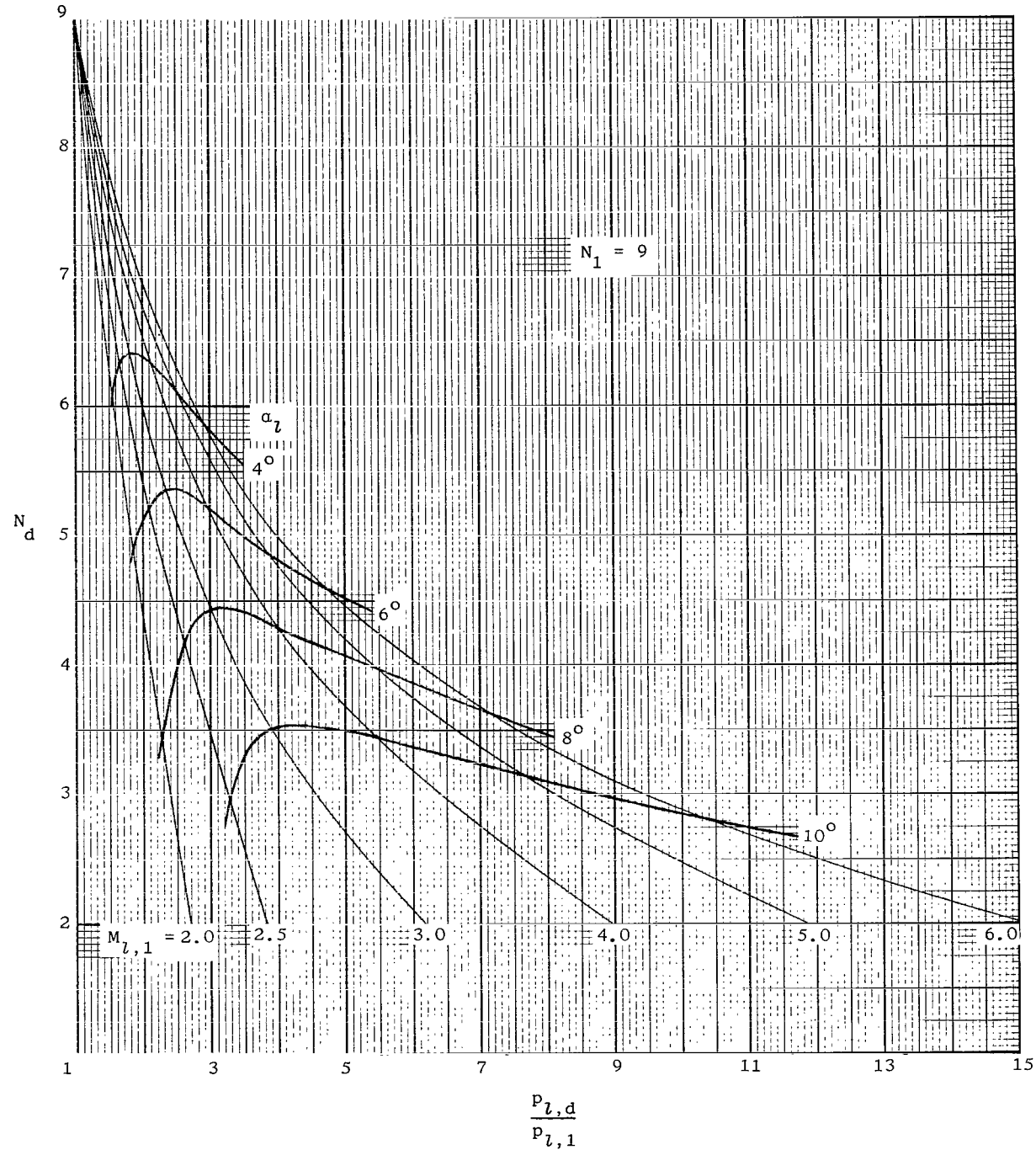

(c) $N_1 = 9$.

Figure 17.- Concluded.

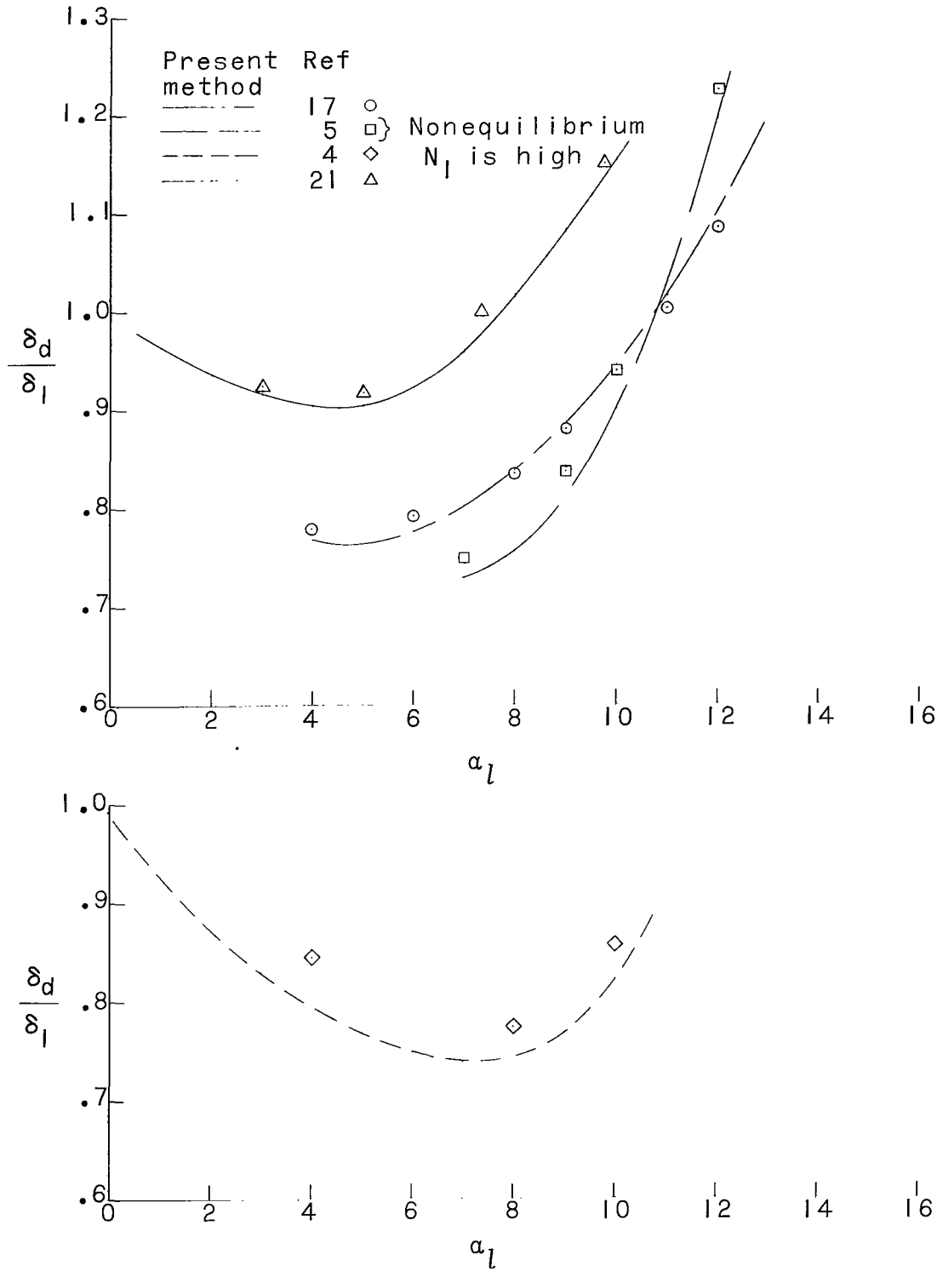

Figure 18.- Calculated boundary-layer thickness changes as compared with experimental data.

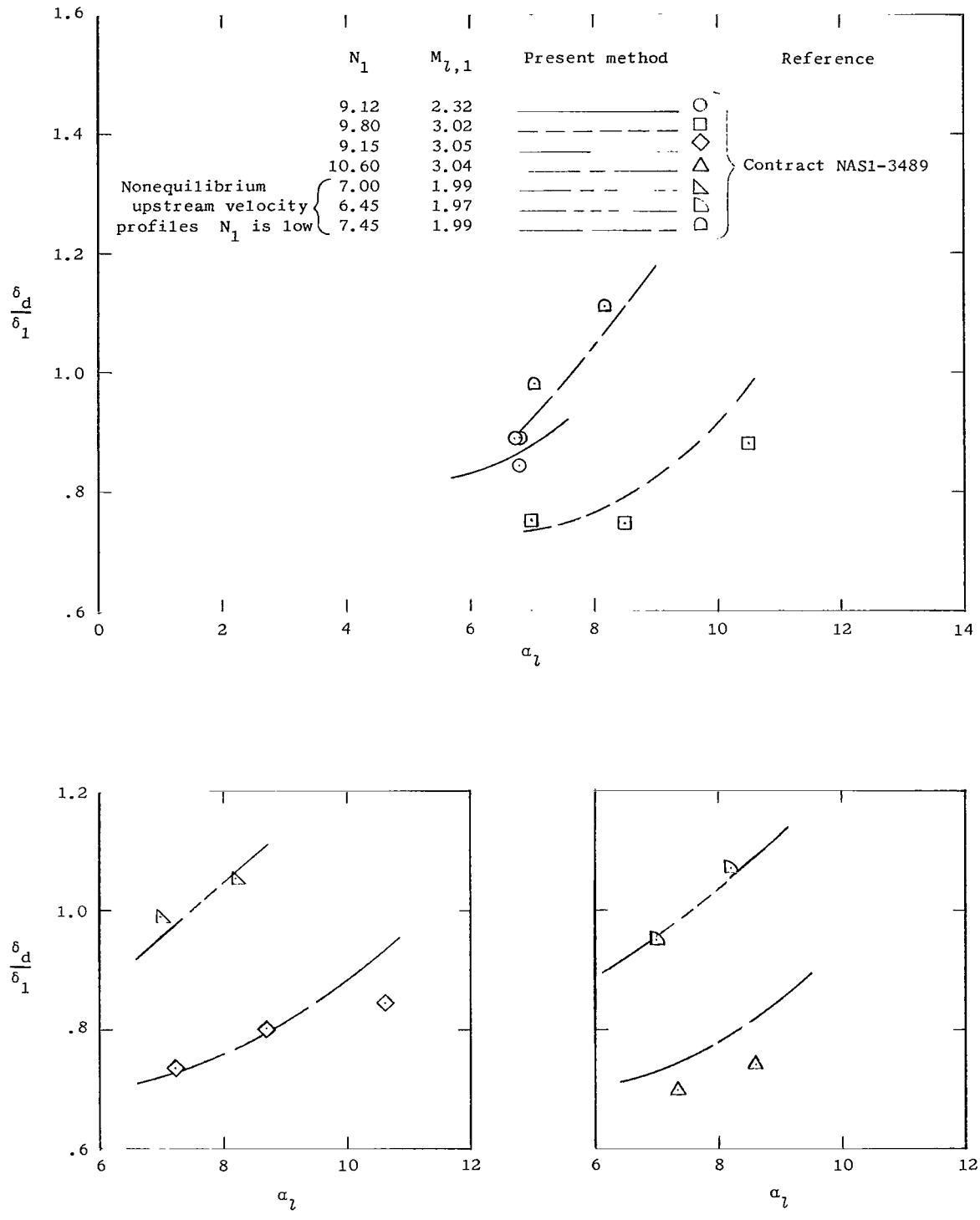

Figure 18.- Concluded.

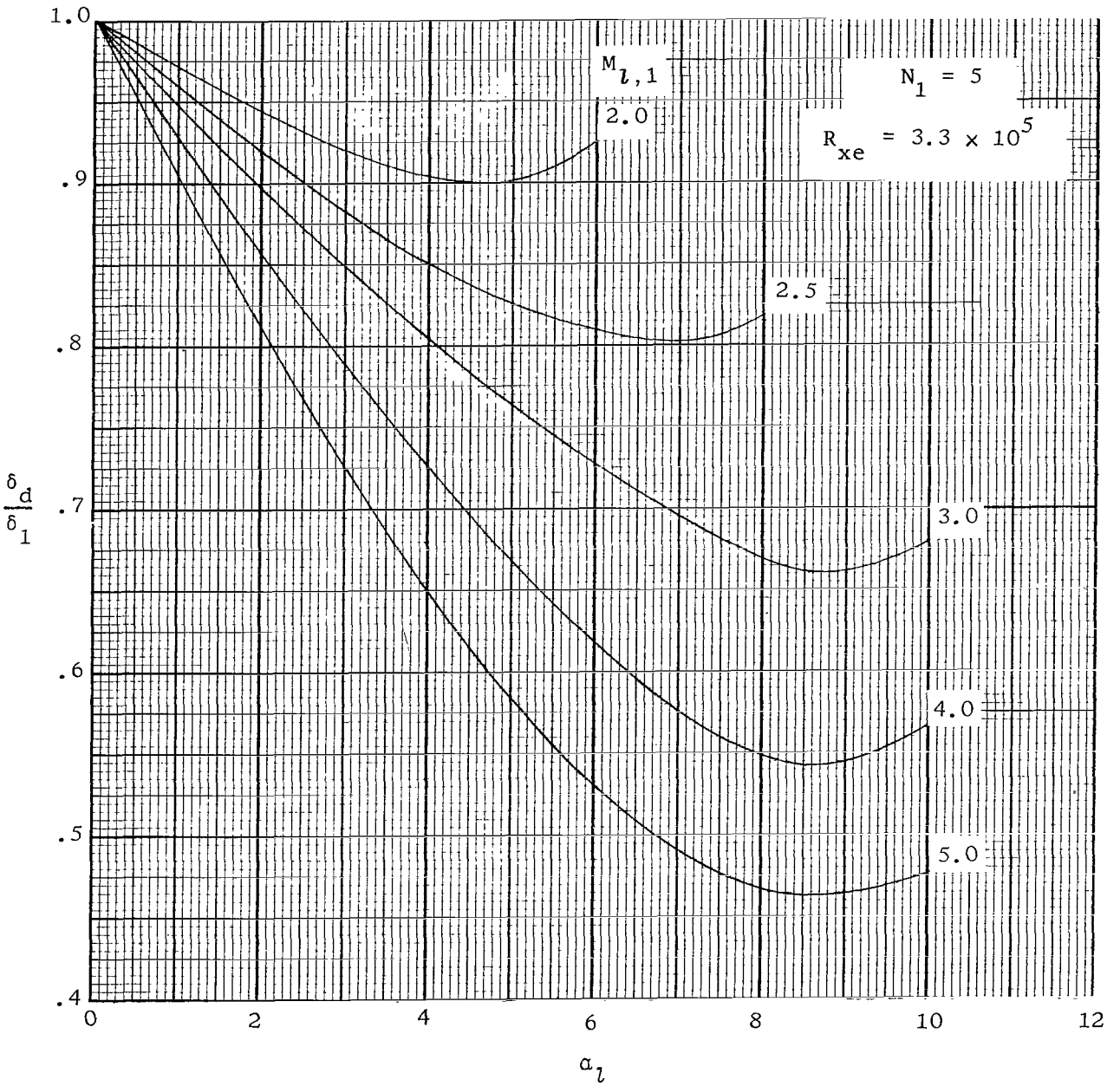

(a) $N_1 = 5$ or $R_{xe} = 3.3 \times 10^5$.

Figure 19.- Curves for the boundary-layer thickness change between stations 1 and d.

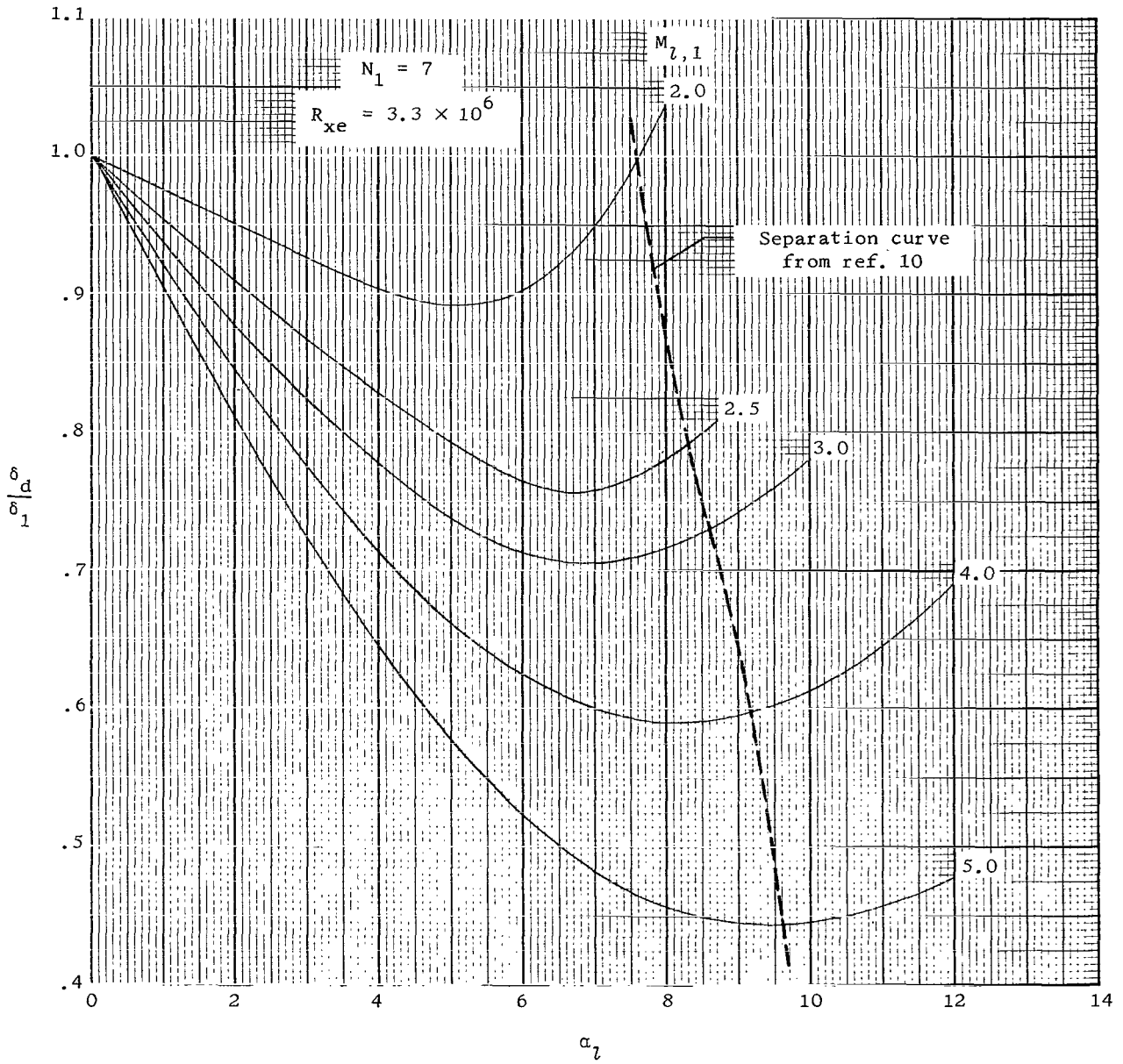

(b) $N_1 = 7$ or $R_{xe} = 3.3 \times 10^6$.

Figure 19.- Continued.

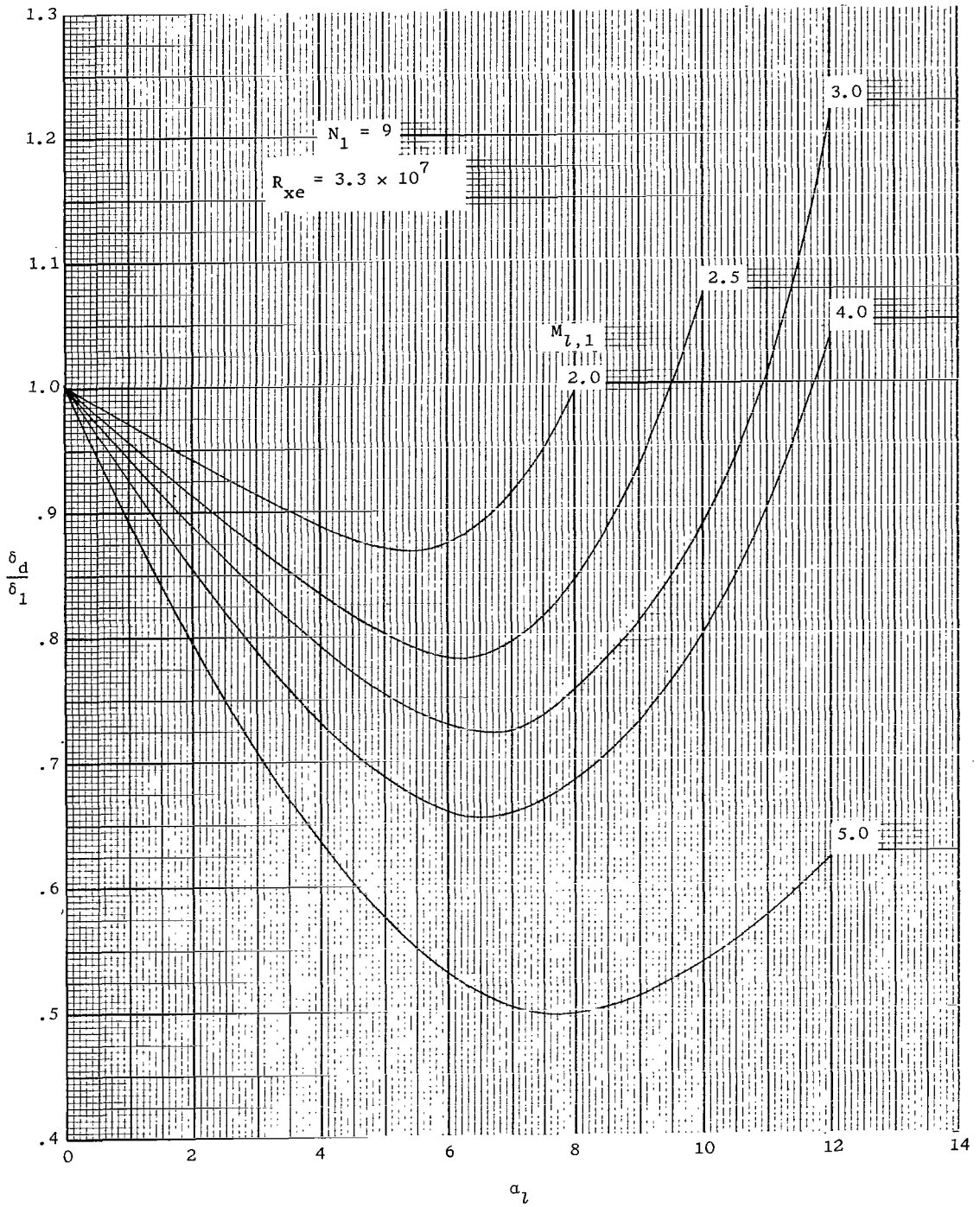

(c) $N_1 = 9$ or $R_{xe} = 3.3 \times 10^7$.

Figure 19.- Concluded.

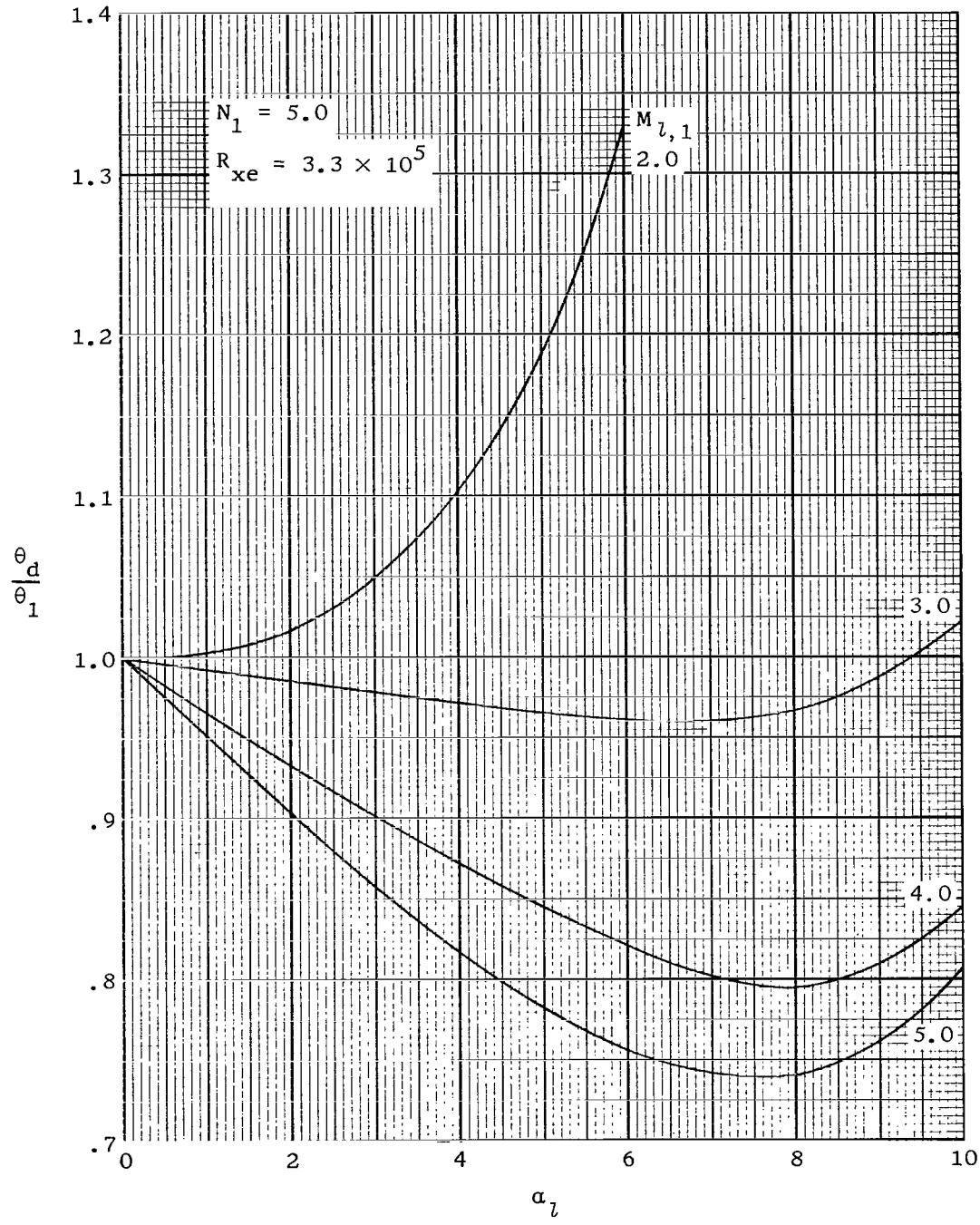

(a) $N_1 = 5$ or $R_{xe} = 3.3 \times 10^5$.

Figure 20.- Calculated momentum thickness-change curves $\frac{\theta_d}{\theta_1}$.

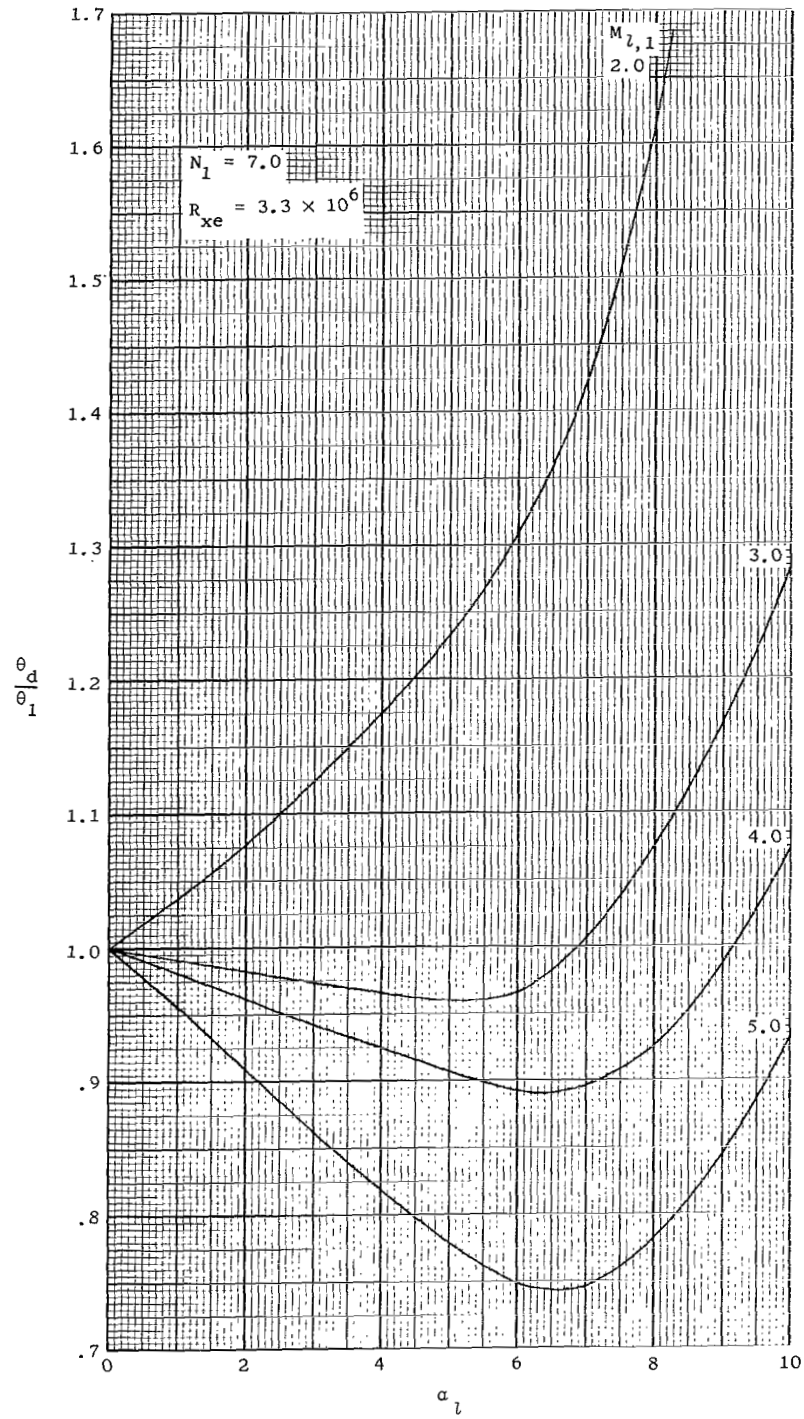

(b) $N_1 = 7$ or $R_{xe} = 3.3 \times 10^6$.

Figure 20.- Continued.

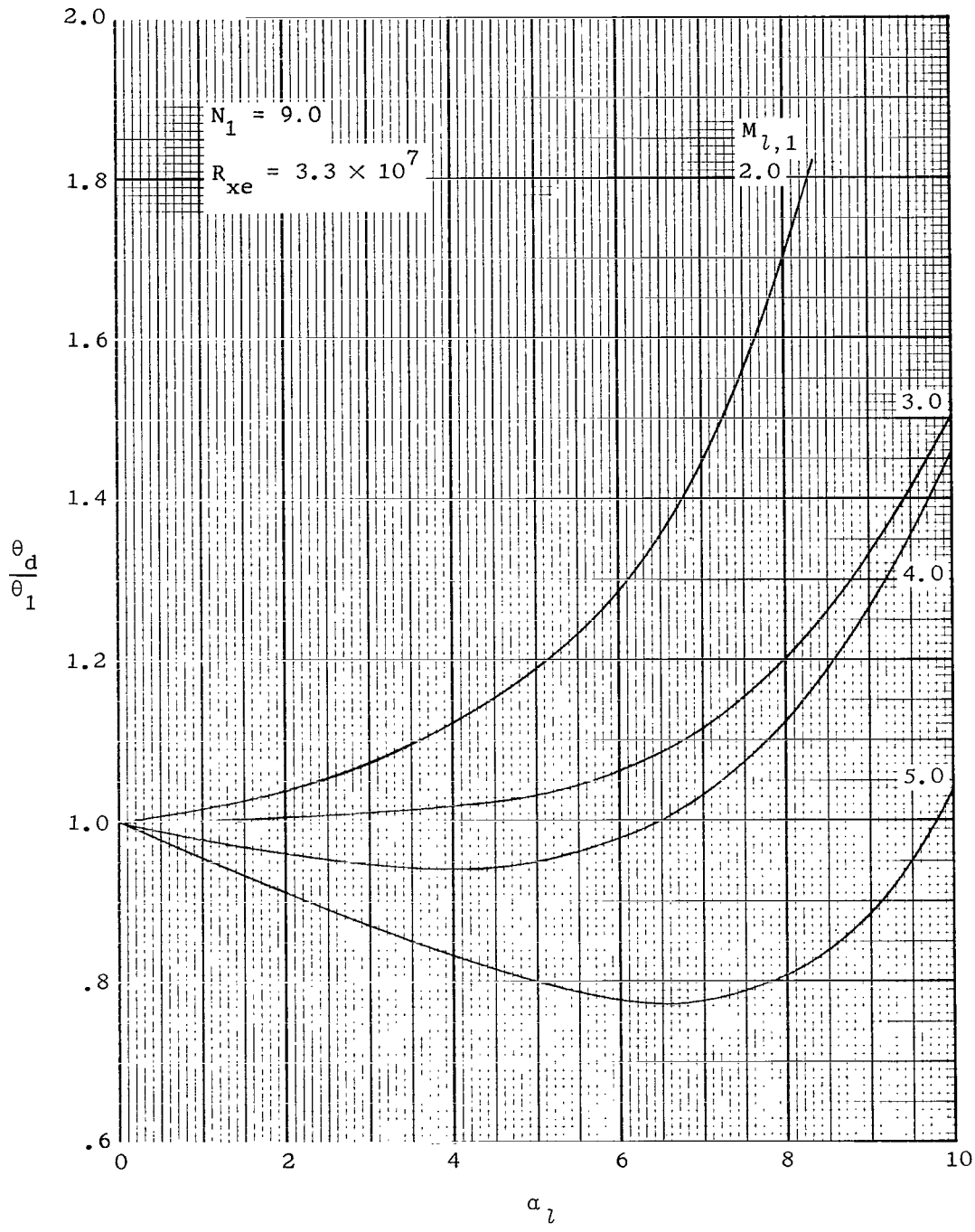

(c) $N_1 = 9$ or $R_{xe} = 3.3 \times 10^7$.

Figure 20.- Concluded.

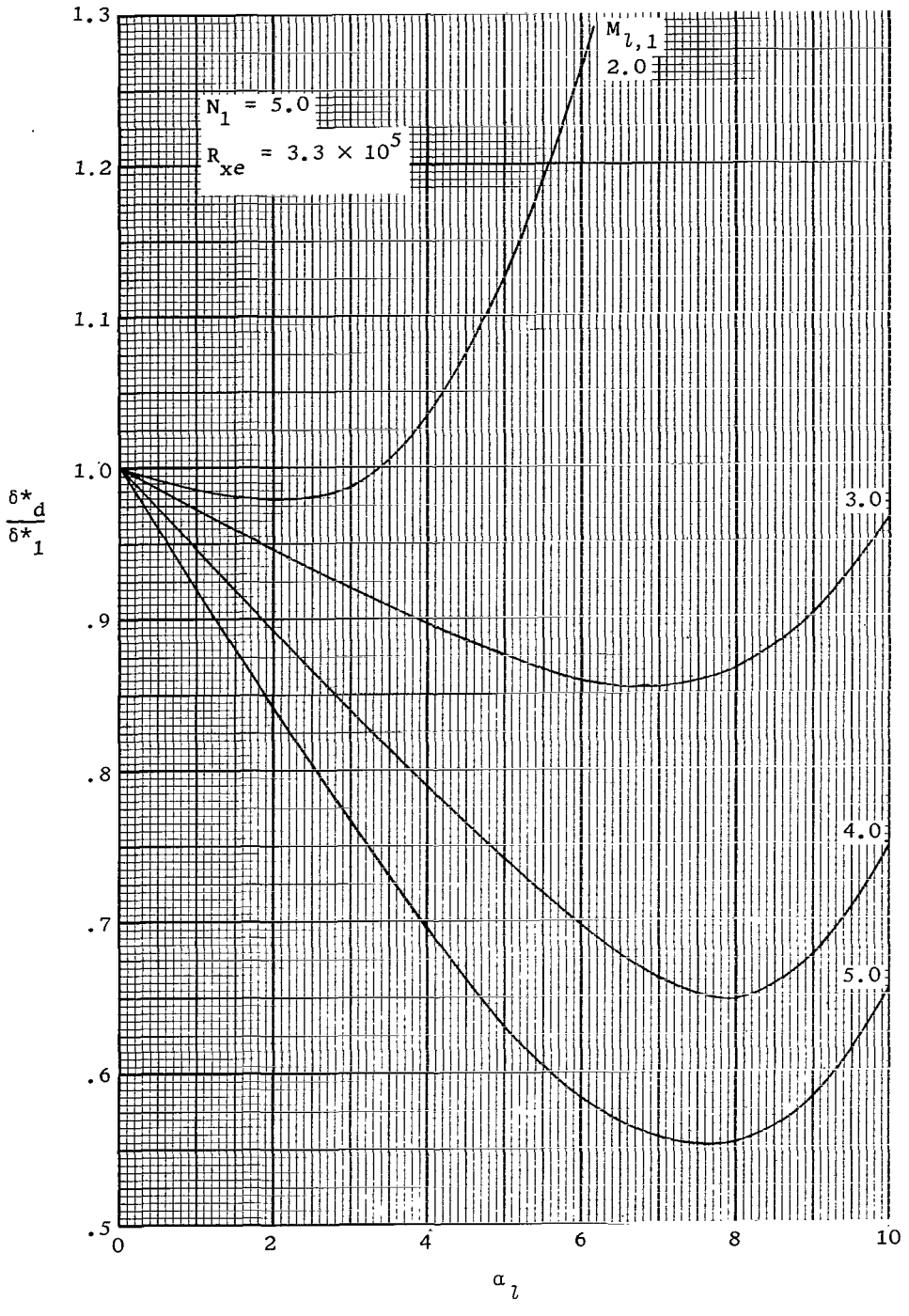

(a) $N_1 = 5$ or $R_{xe} = 3.3 \times 10^5$.

Figure 21.- Calculated displacement thickness-change curves $\frac{\delta^*_d}{\delta^*_1}$.

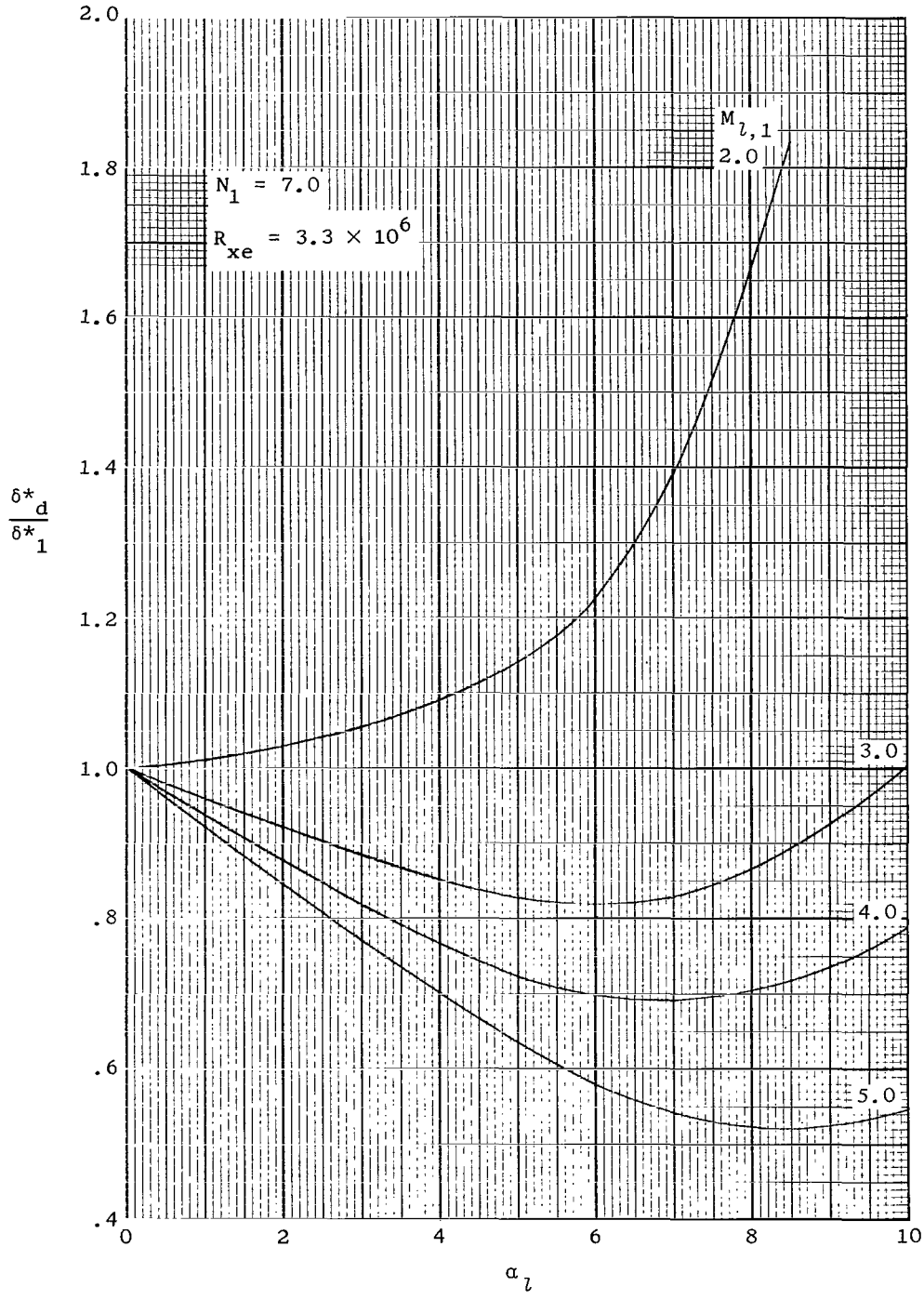

(b) $N_1 = 7$ or $R_{xe} = 3.3 \times 10^6$.

Figure 21.- Continued.

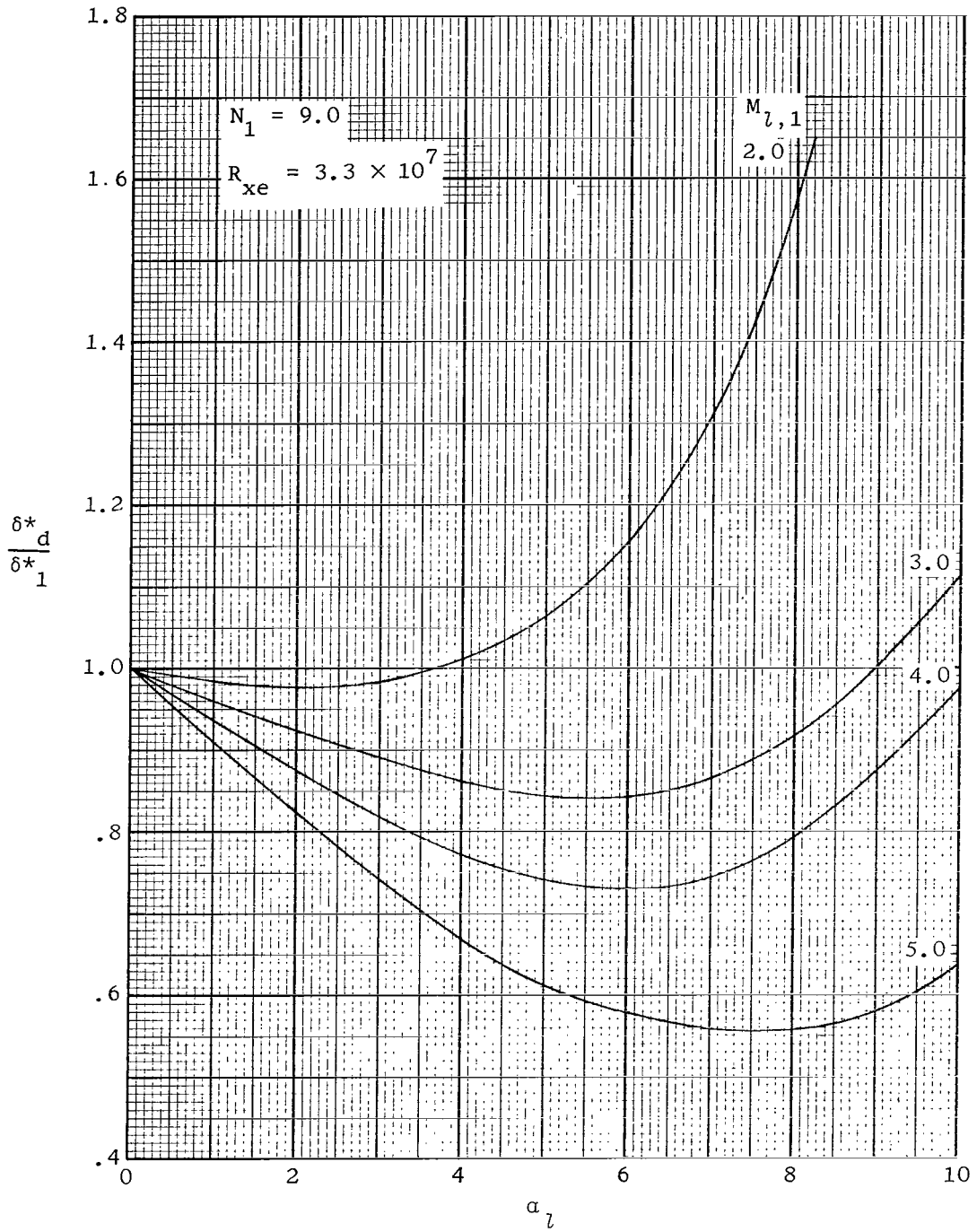

(c) $N_1 = 9$ or $R_{xe} = 3.3 \times 10^7$.

Figure 21.- Concluded.

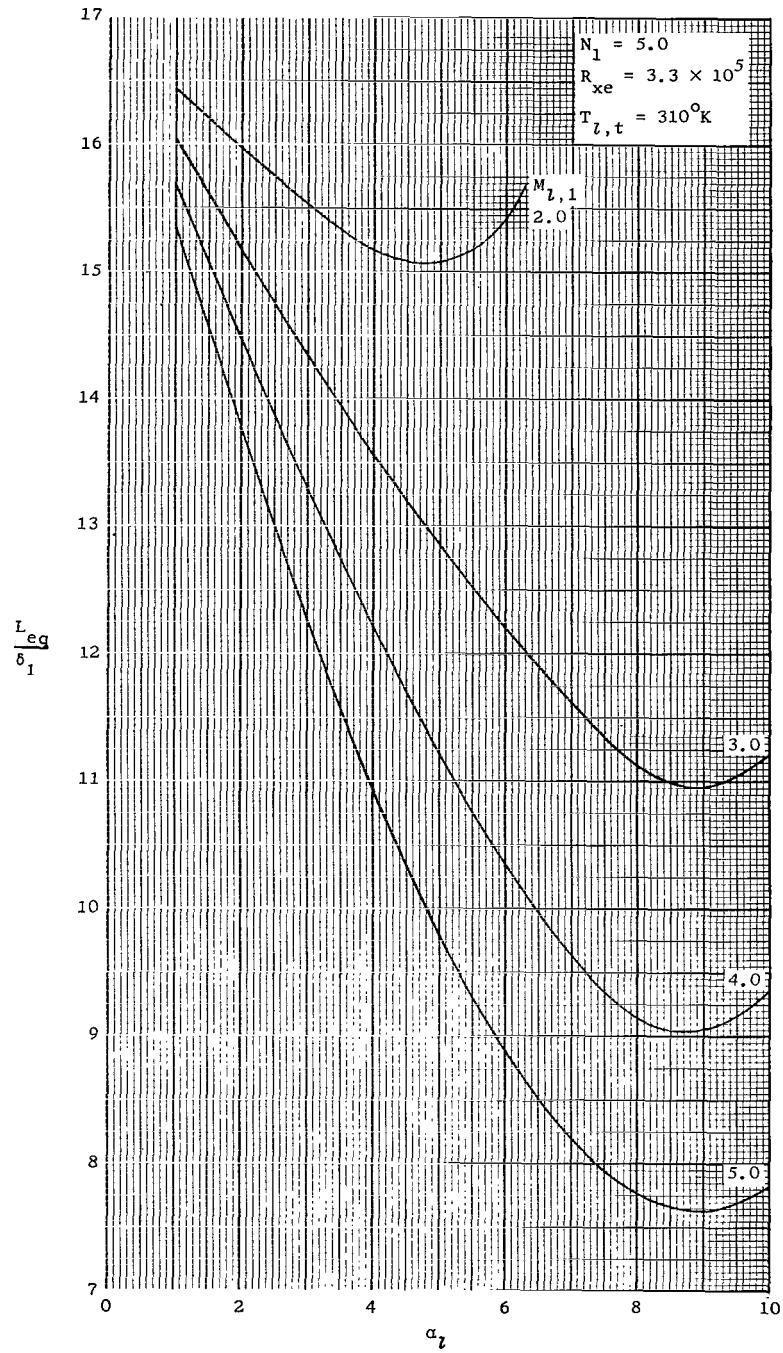

(a) $N_1 = 5$ or $R_{xe} = 3.3 \times 10^5$.

Figure 22.- Calculated values of the nondimensional distance $\frac{L_{eq}}{\delta_1}$ the distance required for a distorted velocity profile at station d to return to an equilibrium profile. $T_{l,t} = 310^\circ$ K.

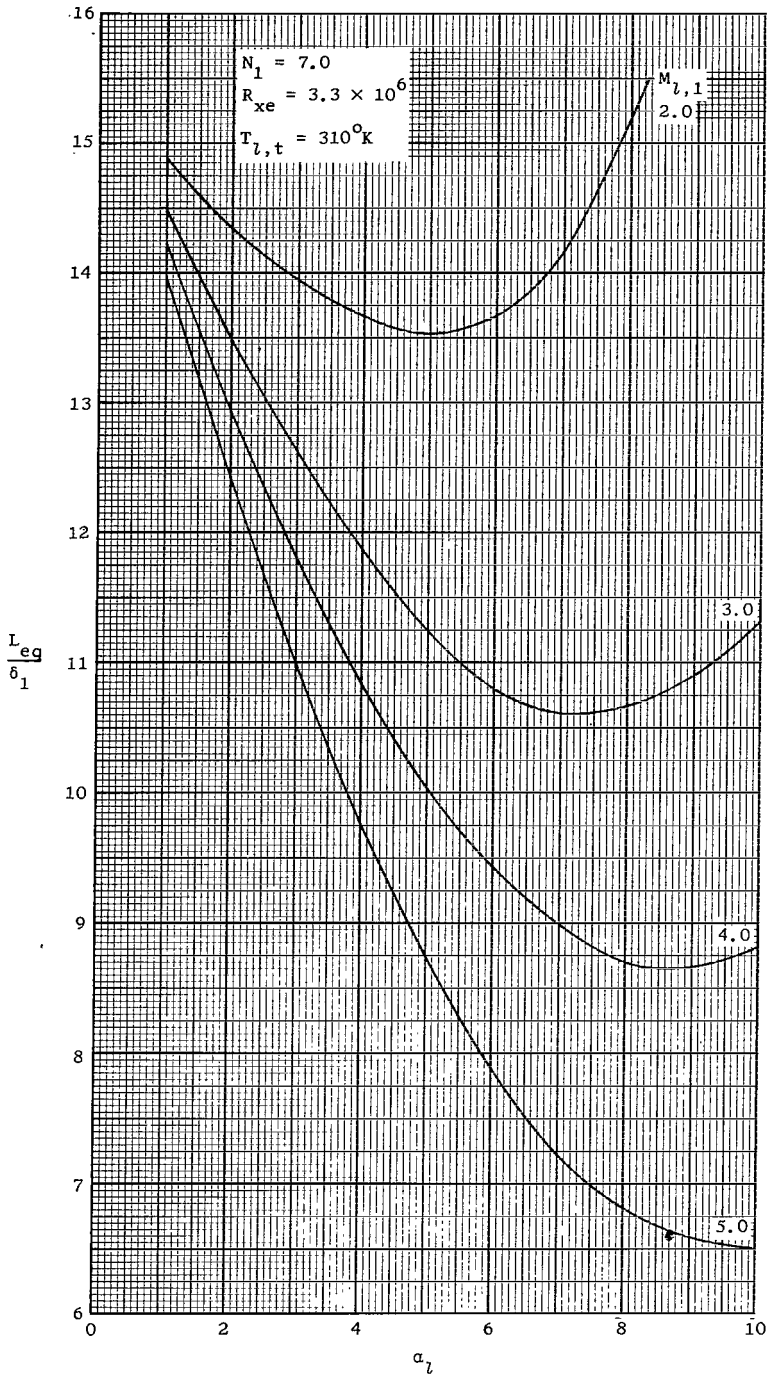

(b) $N_1 = 7$ or $R_{xe} = 3.3 \times 10^6$.

Figure 22.- Continued.

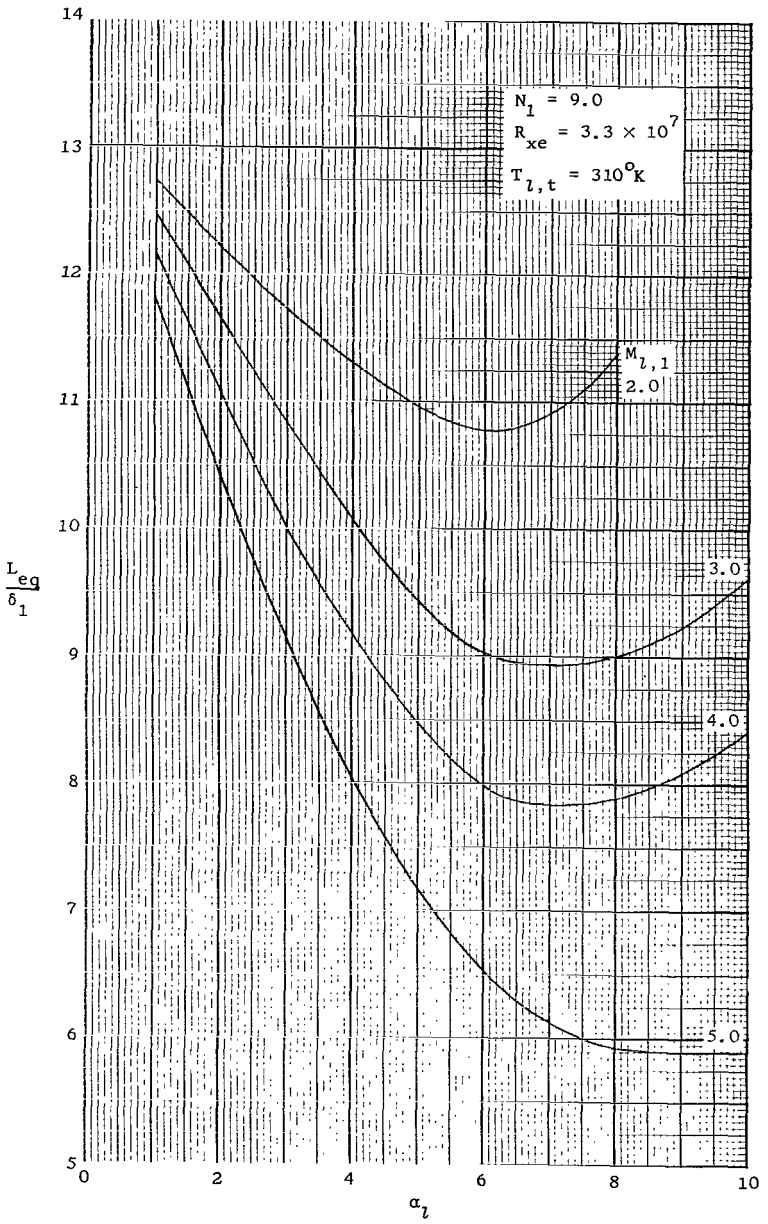

(c) $N_l = 9$ or $R_{xe} = 3.3 \times 10^7$.

Figure 22.- Concluded.

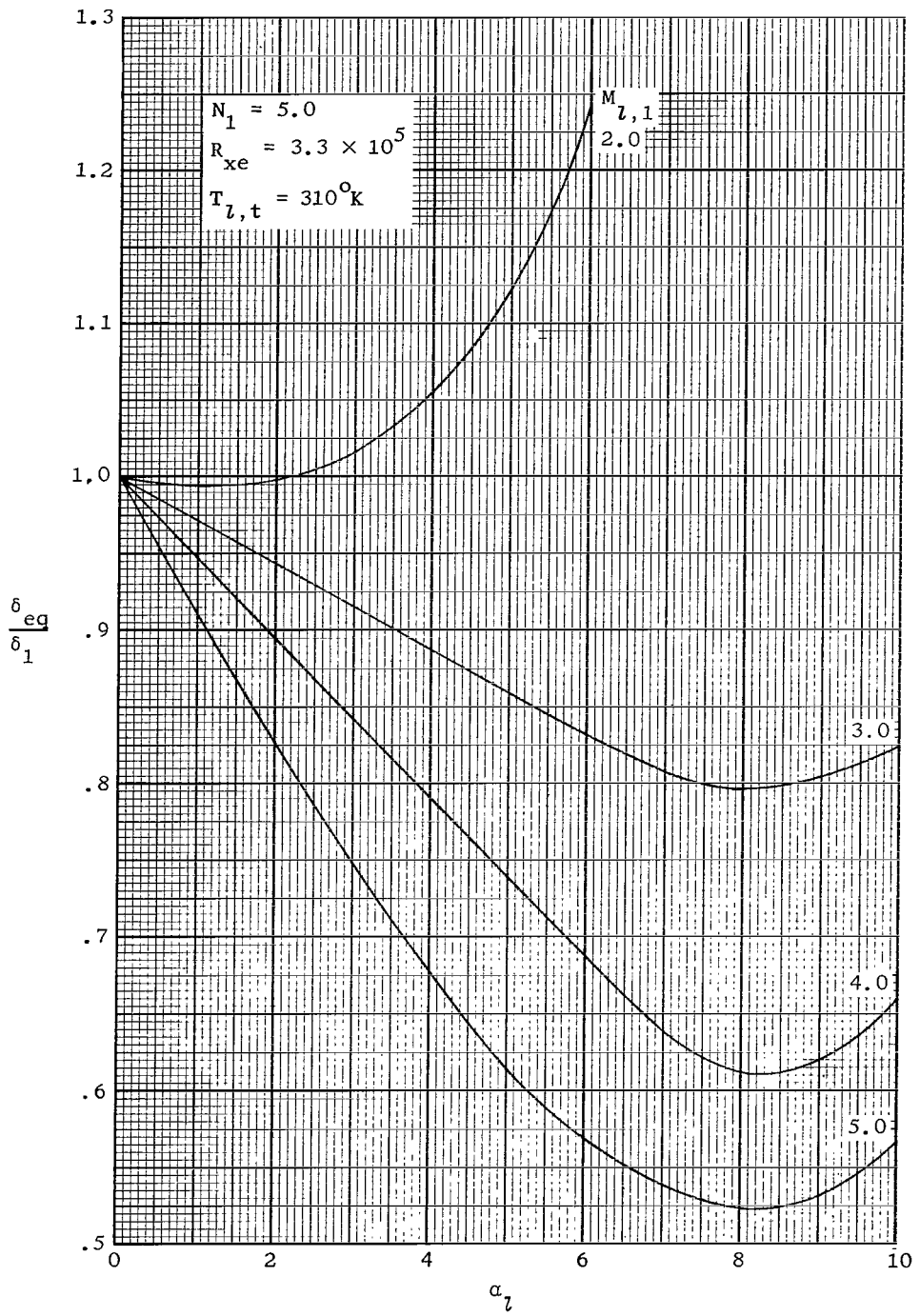

(a) $N_1 = 5$ or $R_{xe} = 3.3 \times 10^5$.

Figure 23.- Computed curves for the boundary-layer thickness change from upstream of the shock, station 1, to the equilibrium velocity profile station, station E, downstream of station d. $T_{l,t} = 310^0$ K.

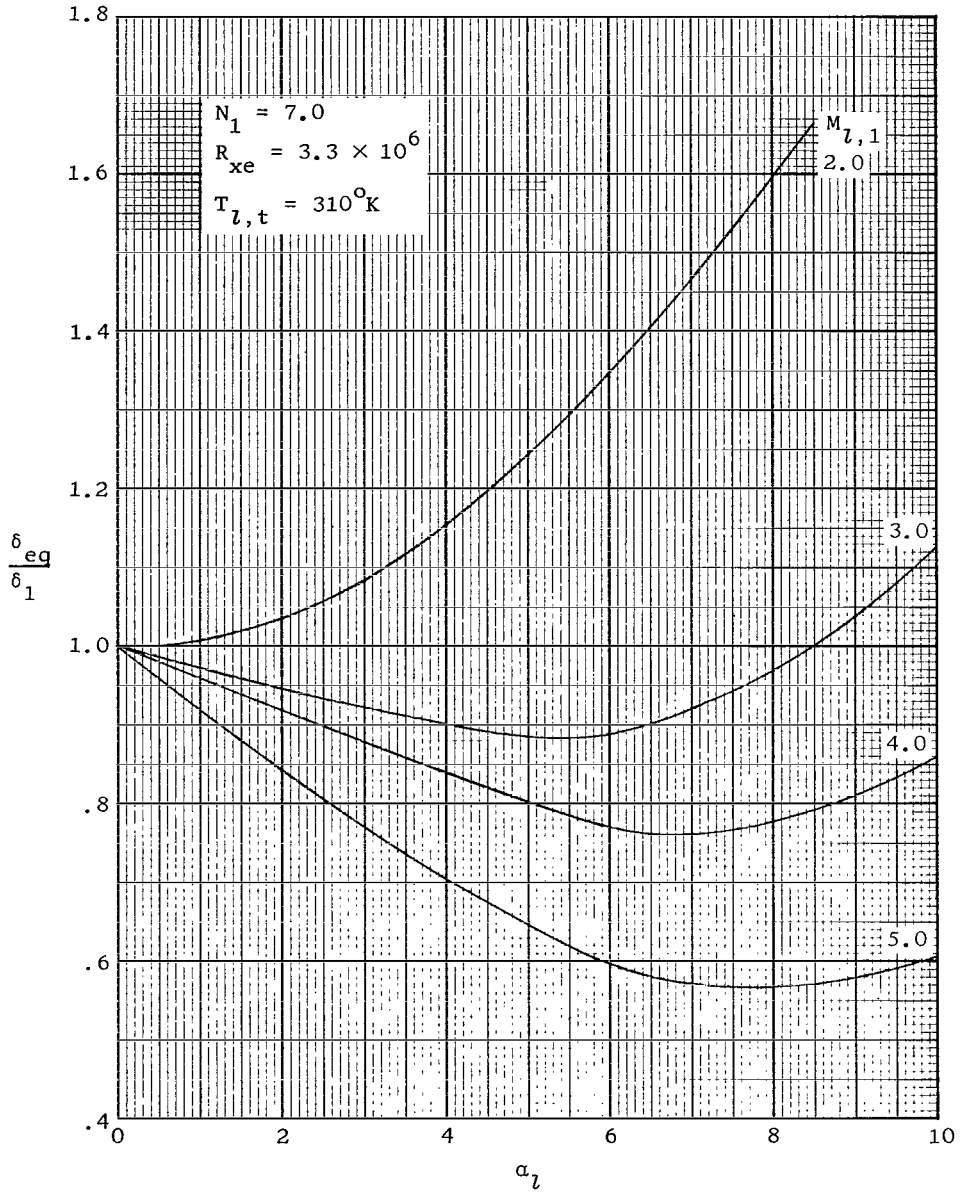

(b) $N_1 = 7$ or $R_{xe} = 3.3 \times 10^6$.

Figure 23.- Continued.

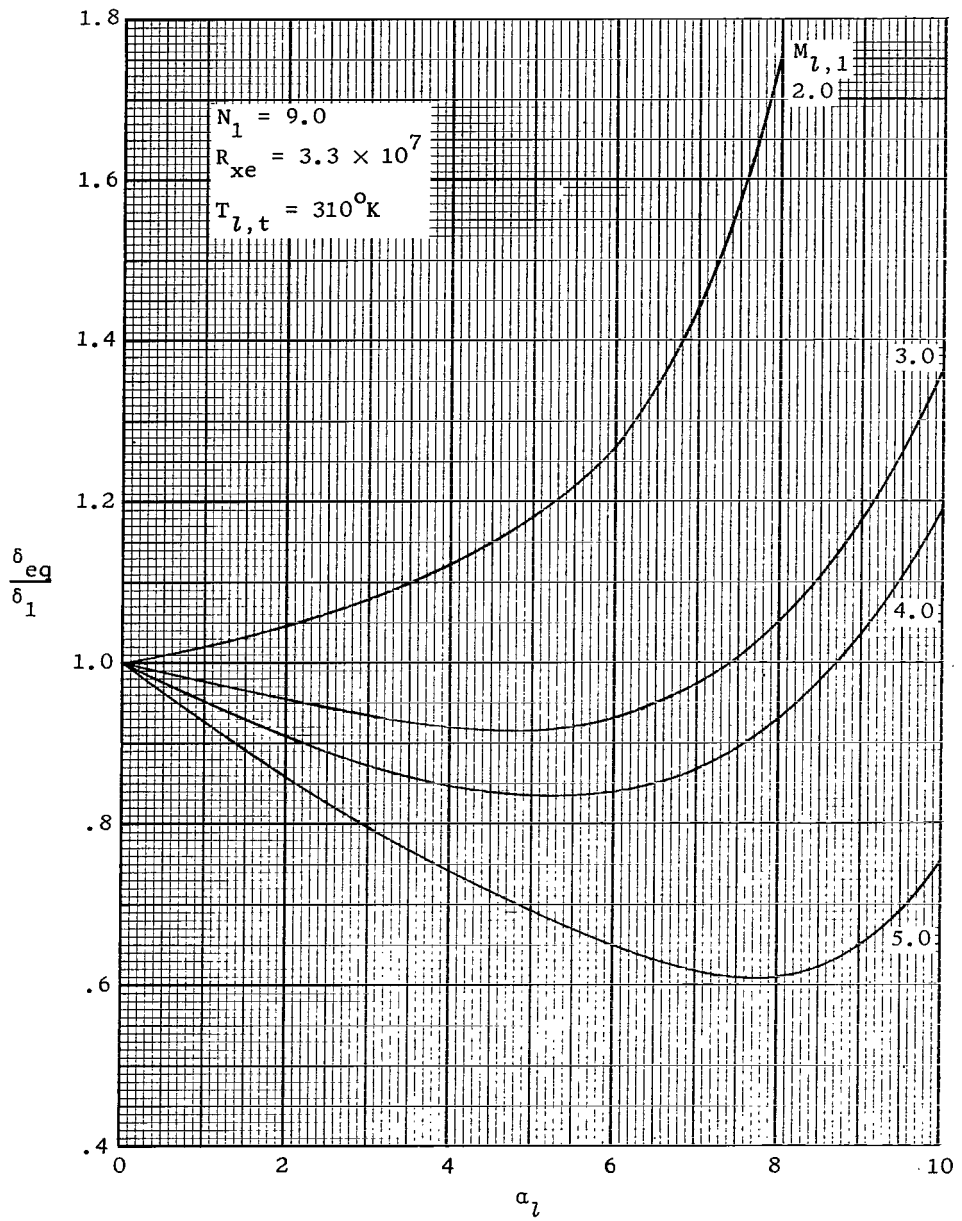

(c) $N_1 = 9$ or $R_{xe} = 3.3 \times 10^7$.

Figure 23.- Concluded.

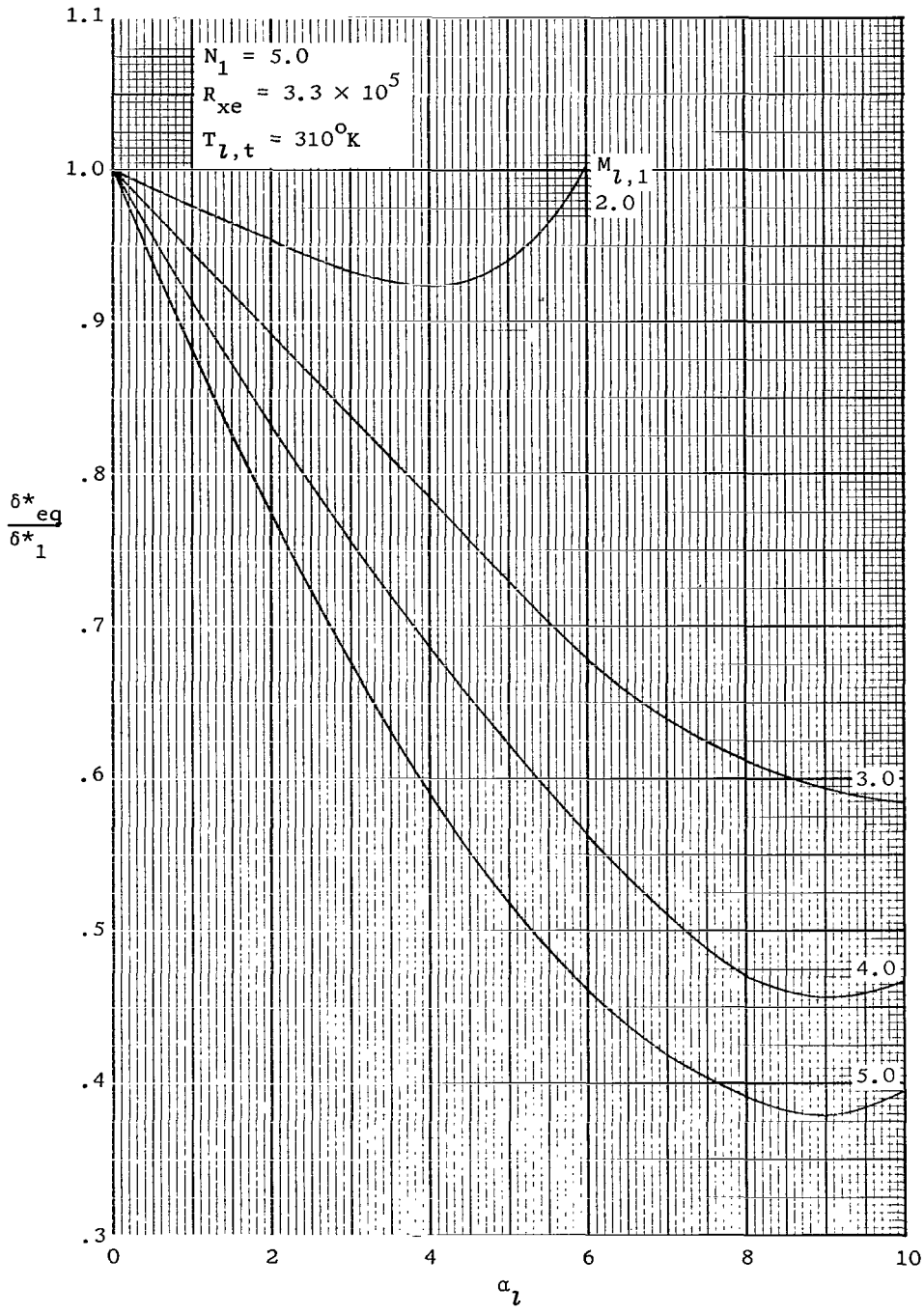

(a) $N_1 = 5$ or $R_{xe} = 3.3 \times 10^5$.

Figure 24.- Computed curves for the displacement thickness change from upstream of the shock, station 1, to the equilibrium velocity profile station, station E, downstream of station d. $T_{l,t} = 310^0$ K.

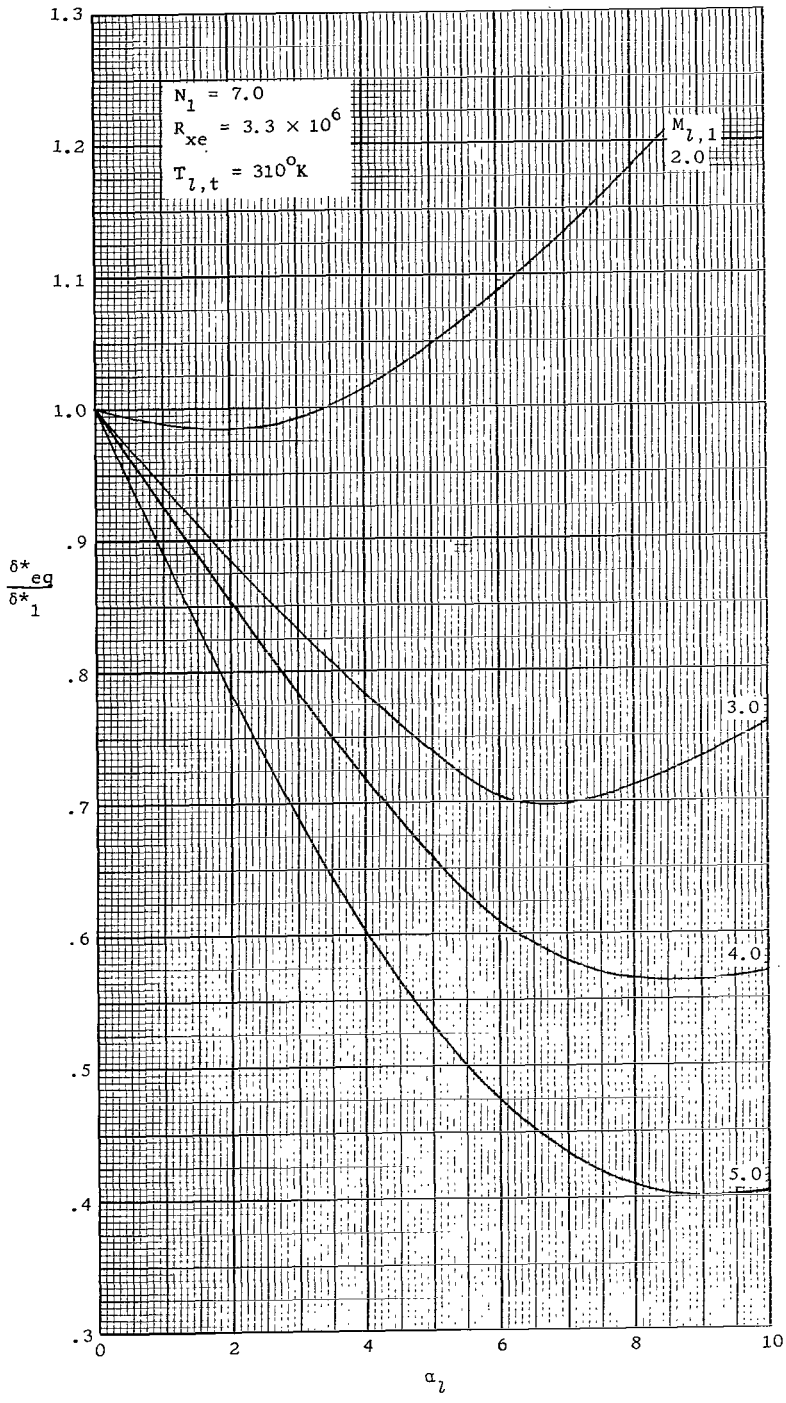

(b) $N_1 = 7$ or $R_{xe} = 3.3 \times 10^6$.

Figure 24.- Continued.

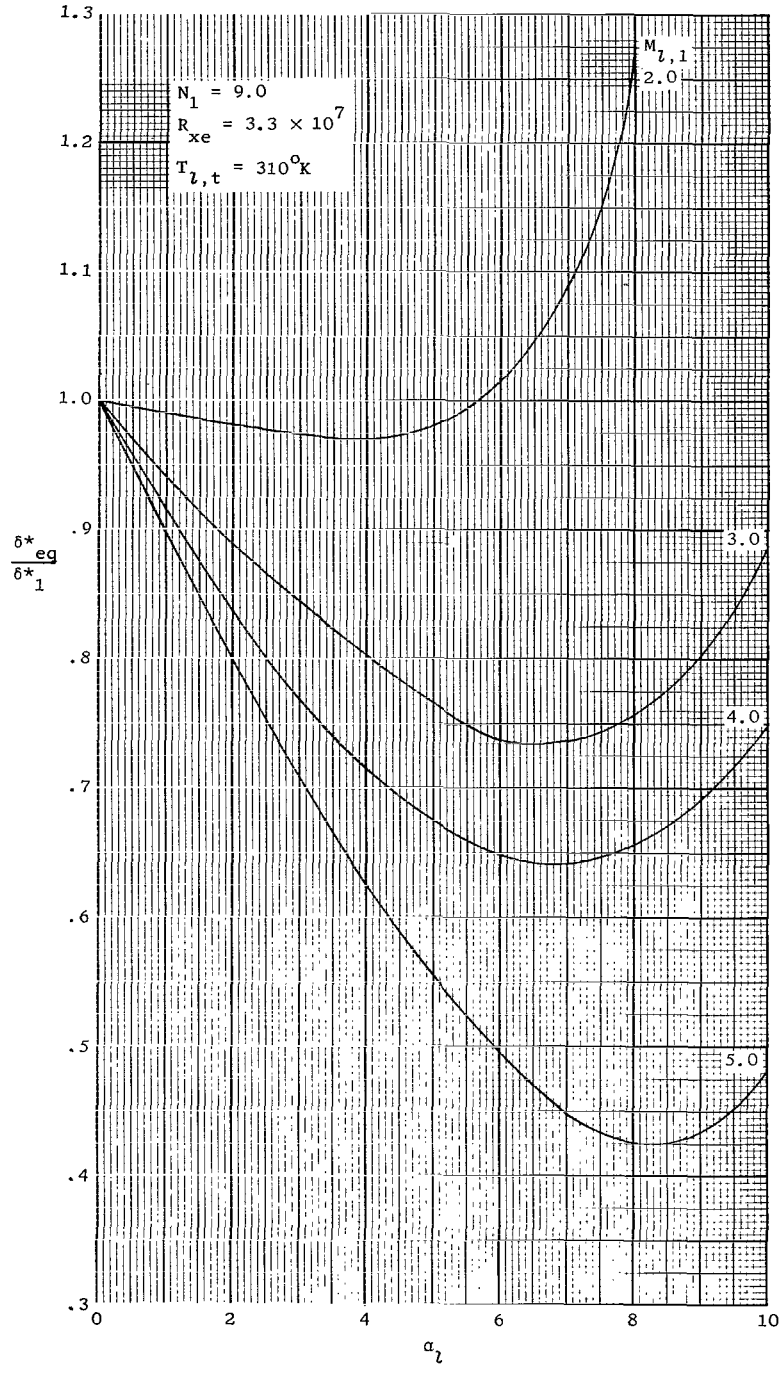

(c) $N_1 = 9$ or $R_{xe} = 3.3 \times 10^7$.

Figure 24.- Concluded.

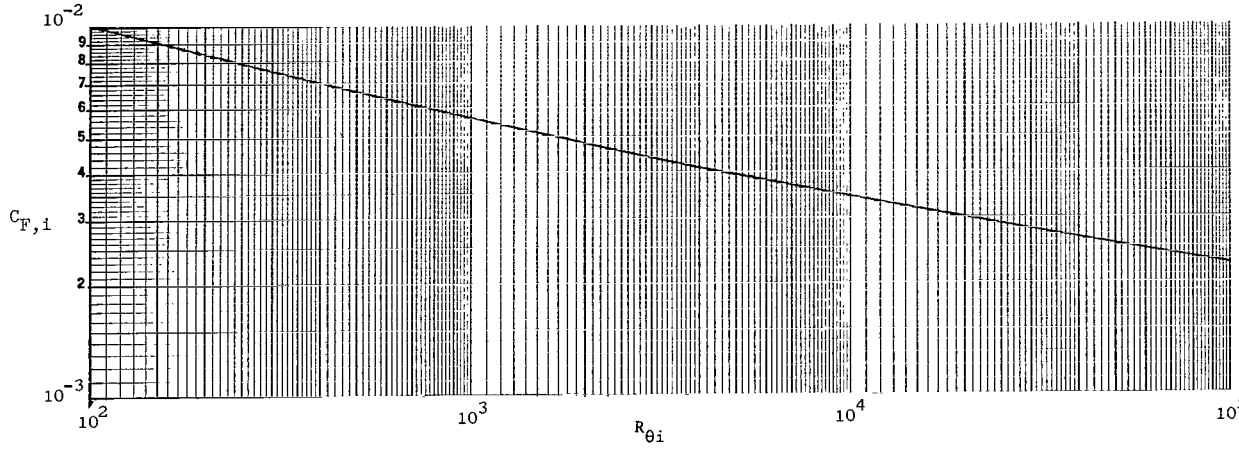

(a) Variation of incompressible average friction coefficient with $R_{\theta i}$.

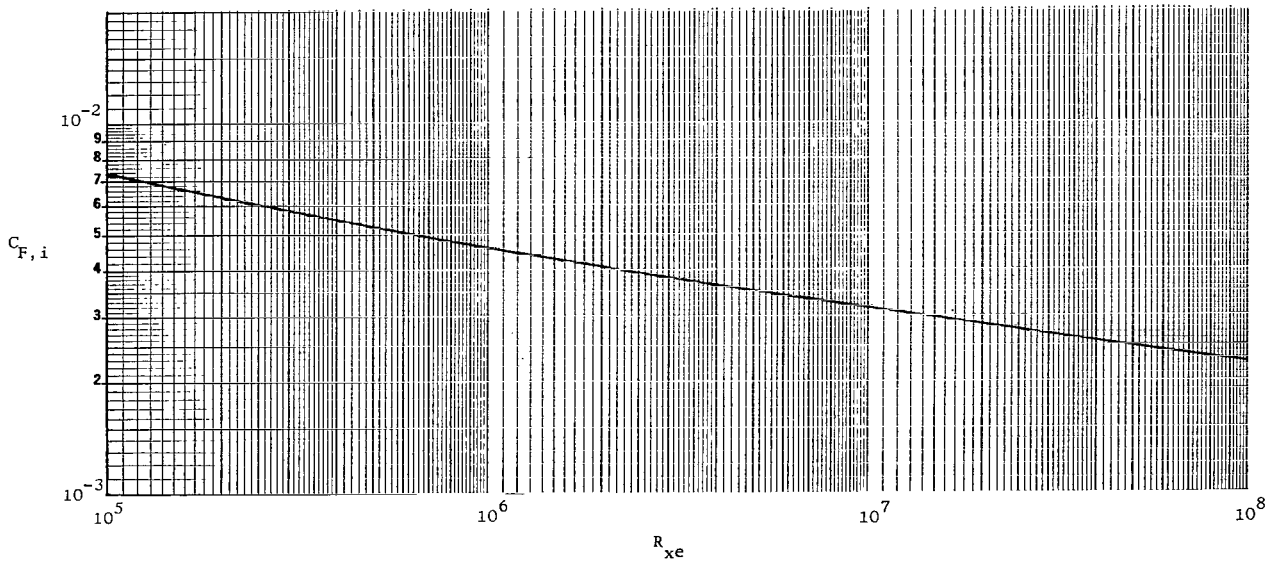

(b) Variation of incompressible average friction coefficient with R_{xe}.

Figure 25.- Incompressible average friction coefficient for turbulent flow.

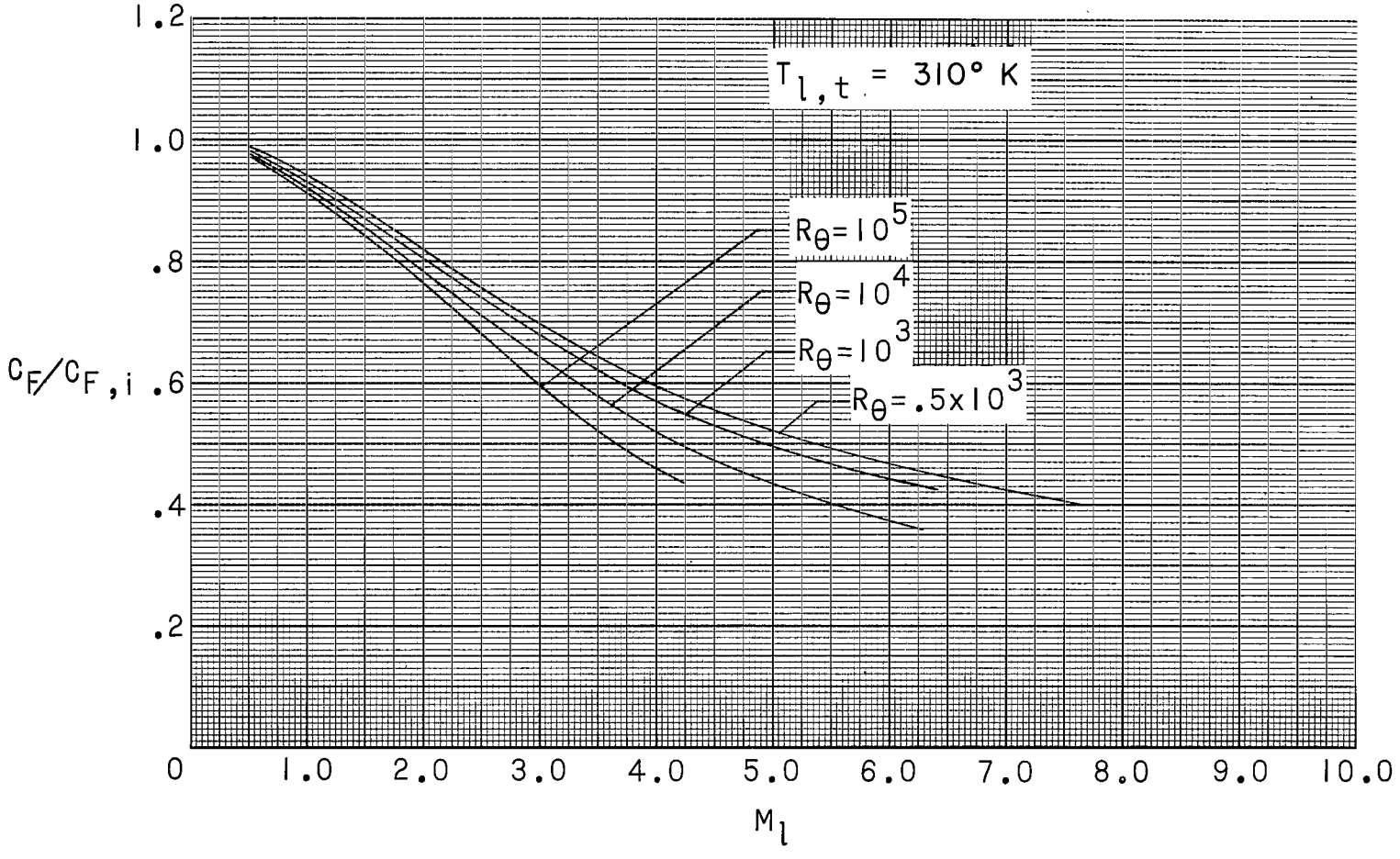

(a) Stagnation temperature $T_{l,t}$ = 310° K.

Figure 26.- Adiabatic-wall values of $\frac{C_F}{C_{F,i}}$ for turbulent flow.

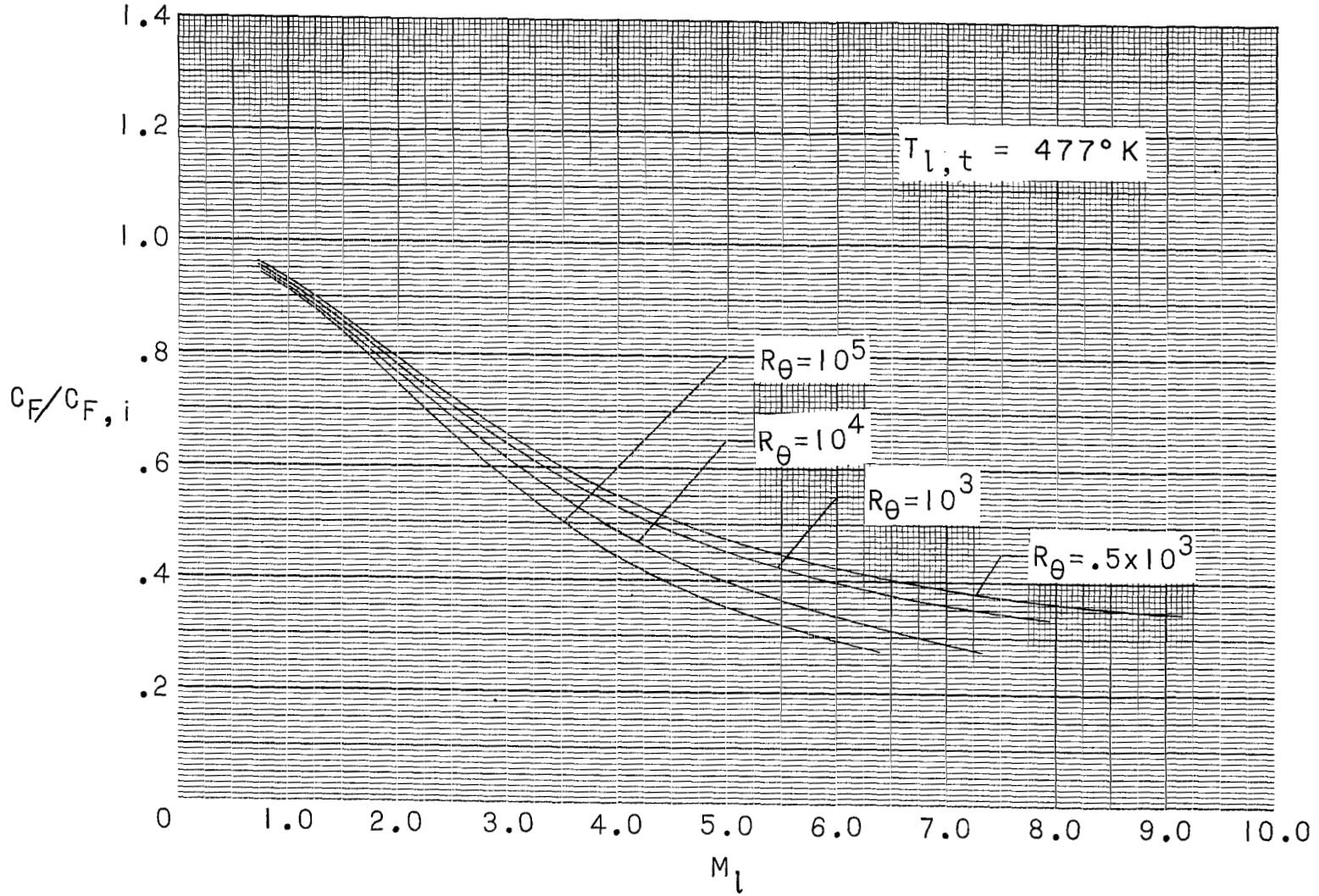

(b) Stagnation temperature $T_{l,t}$ = 477° K.

Figure 26.- Continued.

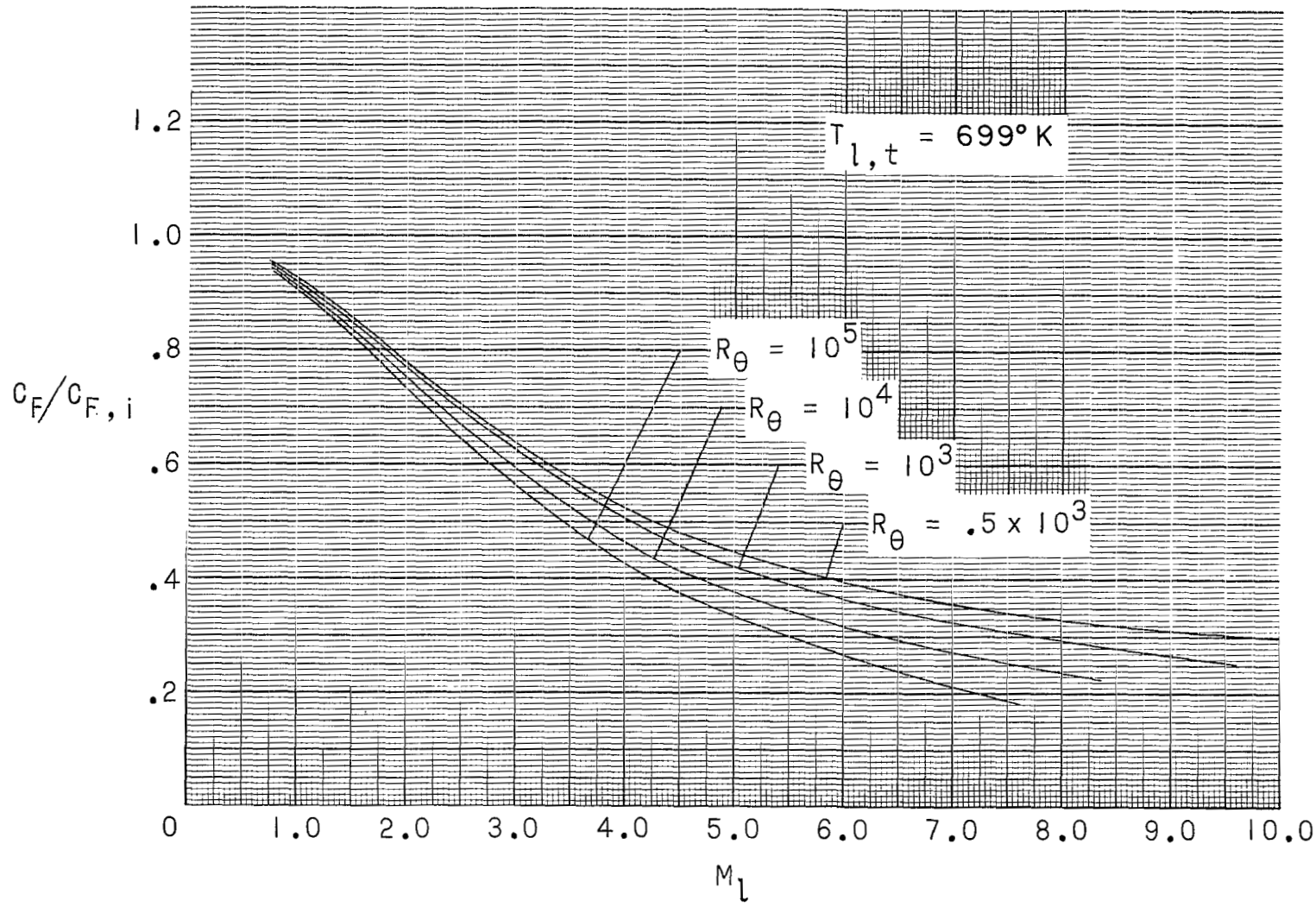

(c) Stagnation temperature $T_{l,t}$ = 699° K.

Figure 26.- Concluded.

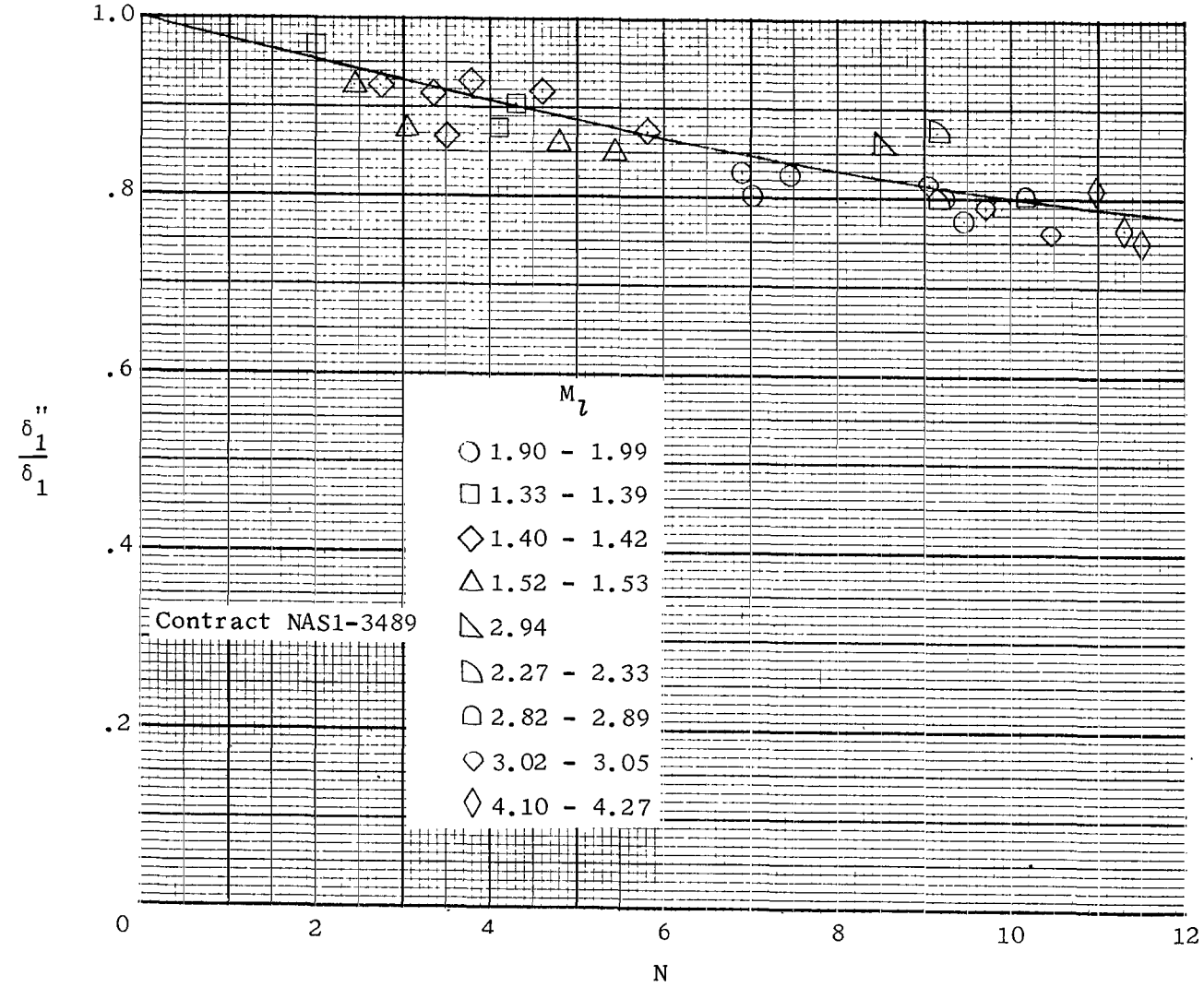

Figure 27.- Plot of $\frac{\delta_1''}{\delta_1}$ as a function of profile index N.

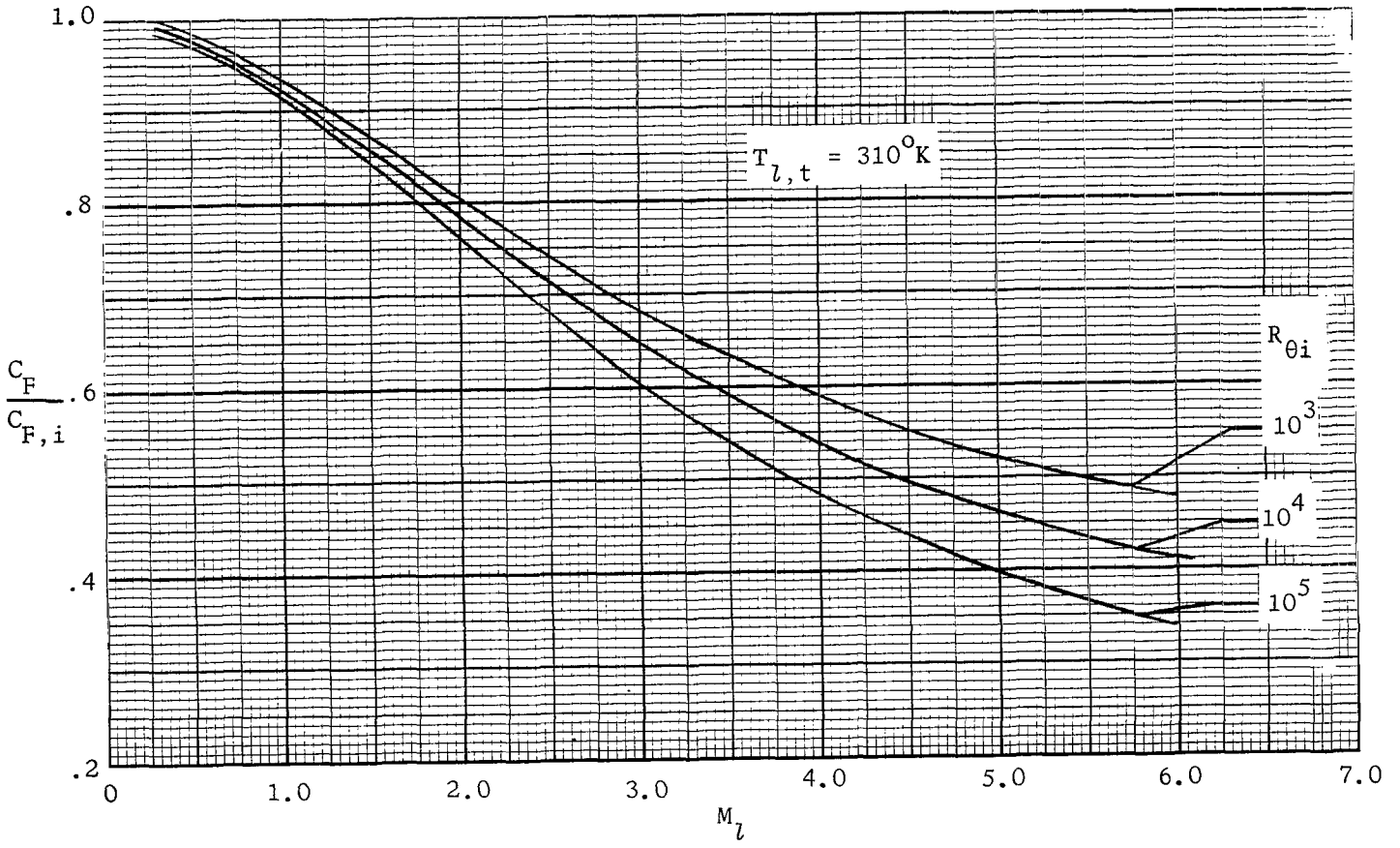

(a) $T_{l,t}$ = 310° K.

Figure 28.- Adiabatic-wall values of $\frac{C_F}{C_{F,i}}$ as a function of free-stream Mach number M_l based on $R_{\theta i}$ for turbulent flow.

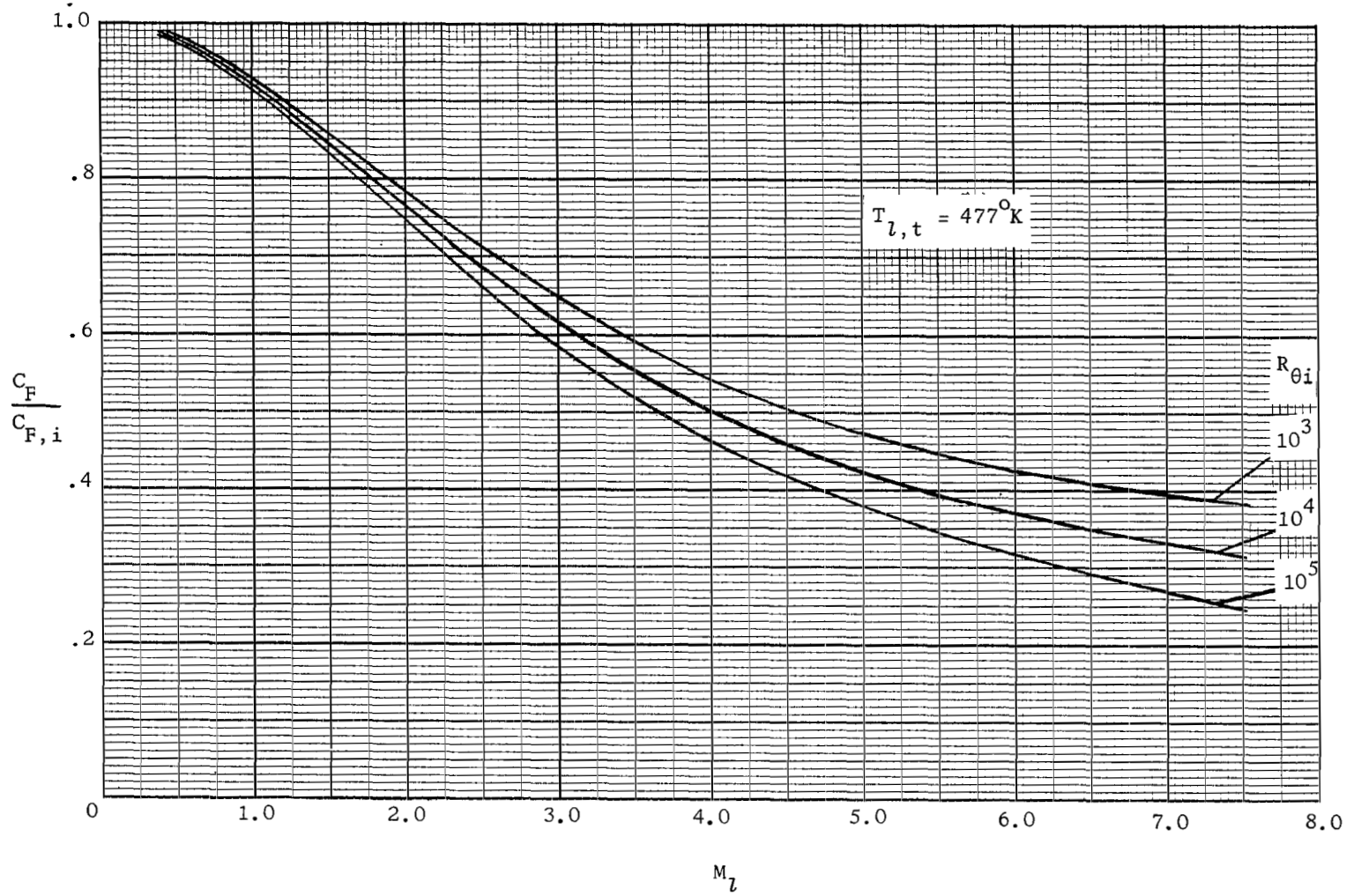

(b) $T_{l,t}$ = 477° K.

Figure 28.- Continued.

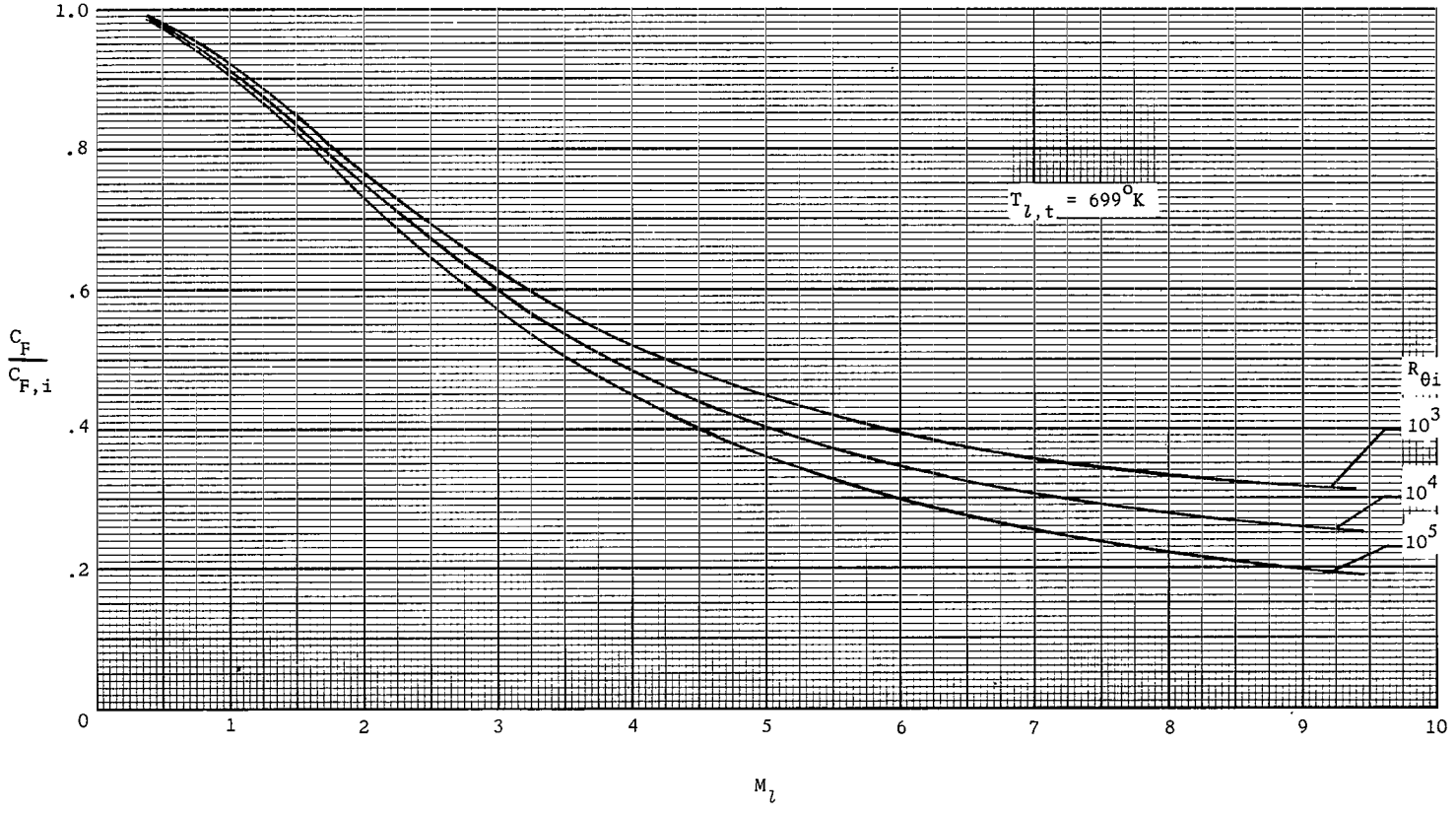

(c) $T_{l,t}$ = 699° K.

Figure 28.- Concluded.

"The aeronautical and space activities of the United States shall be conducted so as to contribute . . . to the expansion of human knowledge of phenomena in the atmosphere and space. The Administration shall provide for the widest practicable and appropriate dissemination of information concerning its activities and the results thereof."

—NATIONAL AERONAUTICS AND SPACE ACT OF 1958

NASA SCIENTIFIC AND TECHNICAL PUBLICATIONS

TECHNICAL REPORTS: Scientific and technical information considered important, complete, and a lasting contribution to existing knowledge.

TECHNICAL NOTES: Information less broad in scope but nevertheless of importance as a contribution to existing knowledge.

TECHNICAL MEMORANDUMS: Information receiving limited distribution because of preliminary data, security classification, or other reasons.

CONTRACTOR REPORTS: Technical information generated in connection with a NASA contract or grant and released under NASA auspices.

TECHNICAL TRANSLATIONS: Information published in a foreign language considered to merit NASA distribution in English.

TECHNICAL REPRINTS: Information derived from NASA activities and initially published in the form of journal articles.

SPECIAL PUBLICATIONS: Information derived from or of value to NASA activities but not necessarily reporting the results of individual NASA-programmed scientific efforts. Publications include conference proceedings, monographs, data compilations, handbooks, sourcebooks, and special bibliographies.

Details on the availability of these publications may be obtained from:

SCIENTIFIC AND TECHNICAL INFORMATION DIVISION

NATIONAL AERONAUTICS AND SPACE ADMINISTRATION

Washington, D.C. 20546